

Surface Plasmon Polaritonic Crystals
for
Applications
in
Optical communications

Maria-Ioanna Benetou

A thesis submitted to the University College London for the degree of
Doctor of Philosophy (Ph.D.)

Department of Electronic and Electrical Engineering

University College London

March 2019

I, Maria-Ioanna Benetou, confirm that the work presented in this thesis is my own.
Where information has been derived from other sources, I confirm that this has been
indicated in this thesis.

To Jonathan, Dimitris, Friends and Family

Abstract

The integration and reduction in the photonic device sizes are essential for the development of applications in short-range interconnects and optical signal processing. Surface plasmon polaritonic crystals (SPPCs) can allow the manipulation of optical information in the microscale level, by coupling photons with collective electron oscillations at a metal–dielectric interface.

This thesis investigates, both numerically and experimentally, the excitation and propagation of the surface plasmon polaritonic (SPP) modes on finite-size SPPCs, their dependence on the nanostructured geometry and the potential applications in implementing different device functions including SPP-beam shaping, such as focusing and splitting, and wavelength/polarisation demultiplexing.

By controlling the SPPC geometry and the excitation beam parameters, directional control of propagating plasmonic modes properties, such as the beam direction, focusing power and beam width, can be achieved. The wavelength-dependent SPP signal spatial separation, due to coupling to the several eigenmodes, and the reduction of the cross-talk by combining polarisation and wavelength modulation have also been shown.

In addition, a compact 4-level polarisation discriminator based on a planar, microscale-scale SPPC was developed as part of the research. Its capability to spatially separate linearly polarised signals with azimuth angles 0° , 45° , 90° and 135° , and define the S_1 and S_2 stokes parameters of any elliptical polarisation state was demonstrated and experimentally tested. The concept was extended to propose a fibre-coupled polarimeter,

able to identify the three Stokes vectors parameters, based on the combination of the SPPC with a high -birefringence fibre.

The use of SPPCs for the implementation and miniaturisation of key optical communication functionalities, in-plane plasmonic beam manipulation and polarisation/wavelength dependent SPP beam propagation, demonstrated in this work can be important for the development of novel integrated nanophotonic functionalities for subwavelength management of optical signals and the design of a new family of compact devices for optical communication applications.

Impact Statement

The integration of various photonic functionalities, along with the reduction in size of integrated photonic systems and telecom components, is essential for the future developments of information processing and transmission for applications in short range interconnects. Plasmonic technology offers unprecedented opportunities in the design of sub-wavelength waveguide circuitry and miniaturised photonic devices. Periodically nanostructured metal films, commonly known as surface plasmon polaritonic crystals (SPPCs), allow for the efficient coupling of incoming optical signal into surface plasmon polariton (SPP) waves [1] offering a promising route to interface plasmonic devices with conventional photonic systems. Until recently, the understanding of the optical properties of SPPCs had been achieved largely by considering infinite crystal lattices, with the role of the boundary shape being largely overlooked, despite its importance for applications in finite size plasmonic structures.

During the research work described in this thesis, it has been shown that appropriate design of the boundary shape allows for the shaping of SPP beams coupled to the smooth metal film, by controlling their refraction and their relative phase relations at the crystal boundary, which can be used for key applications such as information demultiplexing or optimisation of device parameters, such as operation bandwidth and crosstalk [2]

A numerical model based on the point-dipole approximation was developed and compared with experimental results, opening the road to explore the vast parameter space for the design of finite SPPCs for microscale applications [2]. The excitation and propagation of multiple eigenmodes on finite size SPPCs, when several spectral areas are

illuminated, have been investigated both numerically and experimentally, showing the effect of the SPPC boundary and the illumination parameters [2, 3]. The splitting of the SPP eigenmodes at the vicinity of the bandgap, and how the angular separation between the two parts of the same eigenmode can be controlled by engineering the SPPC boundary and controlling the illumination parameters and alignment has been investigated, both experimentally and numerically; this effect can be used on the fabrication of micro-beam splitters and microscale alignment detectors [2-4].

The Fabry-Perot cavities existing at the design of the SPPCs were identified and their effect on the wavelength dispersive properties of the crystal was examined. It has been shown that the substrate Fabry-Perot cavity can enhance the wavelength angular beam separation and decrease the cross-talk.

The spatial separation of SPP signals with different wavelengths, polarisation states or a combination of both has also been investigated, opening the road for numerous on-chip applications. One of these was the development and the experimental testing of a compact, planar, microscale 4-level polarisation discriminator able to spatially separate linearly polarised signals with azimuth angles 0° , 45° , 90° and 135° [5]. The device was also used to determine the S_1 and S_2 stokes parameters of elliptical polarised states and was found in good agreement with a benchtop polarimeter. To achieve a full polarimeter functionality-determine the three Stokes parameters S_1 , S_2 and S_3 - the design of a novel fibre-coupled microscale polarimeter, combining two 4-level polarisation discriminators with a high-birefringence fibre, was proposed [6]. These were welcomed from the scientific community which were inspired to realise full polarimetric devices based on the polarisation-dependent SPP excitation on nanometallic nanostructures [7-15].

Acknowledgments

First and foremost, I would like to thank Jonathan Harper who did everything possible to help me through a very dark period of my life. Jonathan Harper never stopped supporting me and encouraging me to write this PhD thesis, and I feel extremely lucky that God allowed our paths to cross. Furthermore, I would like to thank Dimitris Kentrotis who supported me to start the journey of my postgraduate studies and never stopped encouraging to submit my thesis. I would like also to thank Prof. Polina Bayvel and UCL for allowing me to submit this PhD thesis after an extended period (10 and a half years) after commencing my PhD thesis journey and EPSRC for supporting financially the first three years of my PhD journey.

Furthermore, I would also like to thank Dr. Vitaly Mikhailov for helping me with my initial steps of my experimental work. His idea to automate the experimental procedure using Labview was of vital importance and something that I loved learning. Also, I really enjoyed that after he left from UCL he kept contact and we had some great discussions. I would also like to thank Dr. Benn Thomsen for all his help with my project, the helpful discussions he had and Prof. Nicolae Panoiu for his useful feedback during my transfer thesis exam.

In addition, I would like to thank Prof. Anatoly Zayats, Dr. Wayne Dickson, Dr. Jean-Sebastien Bouillard and Dr. Paulina Segovia for transferring their knowledge about plasmonics to me and provided me with samples of plasmonic crystals.

I would like to particularly thank Dr. Chin Pang Liu, Dr. José Manuel Delgado Mendinueta, Dr. Waegemans, Dr. Martyn Fice and Dr. Robert Steed, as well as all the members of Photonics and Optical Network Groups, for all their help and the great times we passed together.

Last but not least, I would like to thank Elena Kavrohorianou, Dimitra Longinou, Markos Sigalas, Thanos Antoniou, and all my friends from Greece and England, as well as my family who supported during the writing up process of the thesis.

Table of Contents

| | |
|--|------------|
| 1. Introduction..... | 12 |
| 1.1 Motivation | 12 |
| 1.2 Original Contributions..... | 19 |
| 1.3 List of Publications..... | 21 |
| 2. Theory of surface plasmon polaritons - polaritonic crystals | 23 |
| 2.1 Definitions of surface plasmons and surface plasmon polaritons | 28 |
| 2.2 Coupling light into surface plasmons | 29 |
| 3. Analytical calculation of the SPP eigenmodes and their experimental verification | 35 |
| 3.1 Analytical Calculation of the SPP eigenmodes | 35 |
| 3.2 Experimental Arrangement/Procedure | 37 |
| 3.3 SPP Eigenmodes- Results and discussion | 39 |
| 3.4 Summary..... | 41 |
| 4. Visualisation of Bloch modes in finite size plasmonic crystals: Numerical Simulation & Experimental Verification | 43 |
| 4.1 Samples and experiment..... | 44 |
| 4.2 Numerical Model..... | 46 |
| 4.3 Results and discussion..... | 52 |
| 4.3.1 Collimated illumination | 52 |
| 4.3.2 Focused illumination..... | 58 |
| 4.4 Summary..... | 67 |
| 5. SPPC Wavelength Dispersion Properties | 68 |
| 5.1 Experimental Arrangement/Procedure | 80 |
| 5.2 Dense Wavelength Demultiplexing and Power Beam Splitting..... | 85 |
| 5.3 Broadband Wavelength Demultiplexing Based on Multiple Interfaces Eigenmode Excitation..... | 98 |
| 5.4 Summary..... | 107 |
| 6. Multiple-Level Polarisation Demultiplexing based on SPPCs | 111 |
| 6.1 Experimental Procedure | 114 |

| | |
|--|------------|
| 6.2 Summary..... | 124 |
| 7. Conclusions and future work | 126 |
| Appendix 1: Derivation of the dispersion relation of surface plasmon polaritons-smooth metal-dielectric interface..... | 133 |
| Appendix 2: The transverse magnetic (TM) nature of surface plasmons (SPs)..... | 138 |
| Appendix 3: Green-tensor numerical model and Matlab code for the simulation of the SPP excitation and propagation on and around SPPCs..... | 140 |
| Appendix 4: Description of the algorithm to automatically set-up the desired polarisation state | 144 |
| App.4.1 Operational principle of the polarisation controller | 144 |
| App.4.2 Polarisation measurement with a polarimeter | 145 |
| App.4.3 Description of the Nelder-Mead algorithm and its application to the automatic set-up of a specific polarisation state of a laser output beam | 147 |
| Appendix 5: Define the SPPC centre using the SPP wave symmetry | 155 |
| Appendix 6: Calculation of the minimum angular resolution using the camera pixel resolution..... | 157 |
| References | 159 |

1. Introduction

1.1 Motivation

In recent years, there has been tremendous progress in the miniaturisation of optical devices. Devices like optical modulators encode electrical signals to the optical domain, constituting a key element in high-capacity communication links [16, 17]. Ideally, they should feature operation at the highest speed, with the least power consumption, at the smallest footprint and at a low cost [18]. Unfortunately, current technologies fall short of these criteria [19]. Over the last two decades, plasmonics has emerged as a solution offering compact and fast devices [20-23]. Plasmonics is a flourishing field of science that exploits the unique optical properties of metallic nanostructures to route and manipulate light at nanometer length scale [24, 25]. Plasmonics research enables new fundamental science and device technologies and a dramatic growth in both the number and scope of plasmonic applications have been witnessed [24, 25]. With plasmonic devices requiring only a few μm^2 of footprint [26, 27], the technology is much closer to bridging the size gap with respect to complementary metal–oxide–semiconductor (CMOS) electronics, and is likely to allow seamless co-integration with electronics [20]. It can offer the opportunity to combine the size of nanoelectronics and the speed of dielectric photonics, enabling devices that might naturally interface with similar-speed photonic devices and with similar-size electronic components, thus enhancing the synergy between these technologies [25]. An increasing toolbox of plasmonic components is constantly being developed, with a variety of plasmonic and hybrid plasmonic/photonic waveguides and

waveguide components. Key devices based on plasmonic technology such as ring- and disk-waveguide resonators, Mach-Zehnder interferometers, Mach-Zehnder modulators, biosensors, photodetectors, light-emitting diodes (LEDs), optical circuits, optical lasers, Bragg-gratings and nonlinear components have been demonstrated [20, 23, 28-35], allowing plasmonics to play a key role in many applications including optical interconnects for on-chip communications [36], optical/quantum computing [37] and ultra-compact, ultra-sensitive sensing.

Modern micro-processors include tens to hundreds of cores on a single die to improve performance. In order to maximise their performance, a very large bandwidth is needed for the cores to access the data stored in local and distant caches as well as in off-chip main memory [38, 39]. An effective solution, to meet such a bandwidth challenge, is through advanced multiplexing technologies, such as wavelength-division-multiplexing (WDM) and polarisation-division multiplexing (PDM) as widely used in optical fibre communications [40]. In these schemes, multiple wavelengths/polarisation levels can be utilised to increase the transmission rate and maximise the use of the available bandwidth. Each of the wavelength/polarisation states carries a different signal, and all of them simultaneously propagate over a fibre/waveguide. In WDM system the available number of wavelengths is inversely proportional to the channel spacing; the smaller the channel spacing the more channels can fit in a given bandwidth. Wavelength/polarisation demultiplexers are needed to separate the different wavelength/polarisation-coded channels.

In the plasmonic circuitry light is coupling into intense, engineered, localised field distributions able to couple to deep-subwavelength guided modes[1, 25, 41], confine

below the diffraction limit of optics [42] and mediate interactions between propagating radiation and nanoscale objects and devices [24, 25]. To couple optical radiation into surface plasmons (SPs)- the collective oscillations of the free electrons on the metal surfaces- special coupling techniques are required, since the dispersion relation of the surface plasmons lie outside the light cone [1, 43]. Compact devices which can combine vertical-incidence coupling and wavelength/polarisation demultiplexing a focus of much research. Periodically perforated metal films, commonly known as surface plasmon polaritonic crystals (SPPCs) or simply plasmonic crystals, allow the efficient coupling of photons and surface plasmons by modifying the dispersion relation of surface plasmons [1, 44]. Furthermore, surface plasmon polaritonic crystals provide an opportunity to excite and manipulate plasmonic beams with wavelength [45-50] and polarisation [50, 51] control. Such applications rely both on the wavelength dispersion of the surface plasmon polaritonic (SPP) Bloch modes, determined by the period, the size and the shape of the holes, as well as on the SPPC ability to couple these modes onto the smooth film. The signals conditioned by the SPPCs can then be coupled back into optical links or integrated photodetectors. A more extensive review of current literature on wavelength demultiplexers and polarisation demultiplexers/ polarimetric devices are included in chapters 5 and 6 respectively.

The spatial separation of SPP signals based on their wavelength or their polarisation using SPPCs has been the focus of work during the work carried out for this thesis. The wavelength dispersion properties within one eigenmode at the vicinity of the SPP bandgap as well as due to coupling to different eigenmodes have been investigated, examining properties like the wavelength angular beam separation, passband and crosstalk. The

Fabry-Perot cavities existing at the design of the SPPC and their effect on the wavelength dispersion properties has also been examined. Furthermore, the link capacity enhancement of a single-wavelength carrier using polarisation-division multiplexing (PDM) has been experimentally demonstrated. A four-level polarisation discriminator based on an SPPC and able to uniquely spatially separate linearly polarised signals with azimuth angles 0° , 45° , 90° and 135° has been experimentally demonstrated [5, 52]. Due to the surface confinement and the transverse magnetic (TM) nature of SPPs, the polarisation in plasmonic interconnects is highly maintained, and the polarisation-division multiplexing can be simplified compared to the long-haul interconnects in which PDM is generally used together with advanced channel coding techniques, due to the random variation of the polarisation state of light in fibers. The four-level polarisation was also used to identify the S_1 and S_2 Stokes parameters of random elliptical polarised signals and found in good agreement with a benchtop polarimeter. The concept was extended and a micro-level polarimeter, able to identify the three Stokes vectors, S_1 , S_2 , S_3 , made from the combination of two SPPCs and a $(n+1/4)L$ length of a high-birefringence fiber, where L is the HiBi beat length, was proposed [6].

In conclusion the main aim of the research conducted for this PhD thesis was to investigate the excitation of SPP eigenmodes in finite size SPPCs of various periods, boundary shapes and under various illumination schemes at the telecommunication wavelengths. The possibility of using the SPPCs as wavelength or polarisation demultiplexers has also been examined by investigating the SPP eigenmode wavelength dispersion at the vicinity of the bandgaps and the excitation of multiple eigenmodes in both metal-dielectric interfaces, air- Au and glass-Au. Phenomena like the SPP

eigenmode splitting and the effect of the SPPC boundary on the angular separation of the two beams, and the effect of the SPPCs Fabry-Perot cavities on the eigenmode wavelength dispersion properties have been examined. The miniaturisation of crucial devices like this of a four-level polarisation discriminator and a polarimeter has also been experimentally demonstrated or proposed.

The rest of this PhD thesis is structured as follows. Chapter 2 provides the essential theory of surface plasmons (SPs), their coupling to photons to form the surface plasmon polaritons (SPPs), the surface plasmon polaritonic crystals (SPPCs) and the SPP eigenmodes and bandgaps formed on their surfaces, essential for the understanding of the work described in this thesis.

Chapter 3 describes the experimental study of the SPP eigenmodes and bandgaps in the SPPC transmission dispersion, by measuring the SPPC transmission spectrum under collimated illumination in a range of incident angles. The flattening of the eigenmodes close to the bandgaps and their dependence on the SPPC period are also observed experimentally. The eigenmodes were also calculated analytically and compared with the experimentally observed ones.

In chapter 4 the excitation and propagation of the SPP eigenmodes on finite size SPPCs is investigated, using a numerical model, based on the point-dipole approximation, developed during the course of this thesis and compared with experimental images, acquired through scanning near-field optical microscopy (SNOM) images. The effect of the SPPC boundary is investigated under collimated and strongly focused illumination. Significant differences are identified in the excitation of broad SPP beams by plasmonic crystals with the same lattice but with different boundary shapes. The origin of these

differences is explained by the relative phase-relations between the individual SPP scatterers at the boundary of the crystal, leading to complex interferences on the smooth metal film. The excitation of multiple narrow SPP beams at the same wavelength using strongly focused illumination is also demonstrated both experimentally and numerically. Furthermore, the wavelength-dependent SPP coupling, which allows for wavelength demultiplexing functionality and flat transmission band is described.

In chapter 5 after a short summary of the state-of-art, miniaturised wavelength demultiplexers, the SPPC wavelength dispersive properties have been experimentally characterised for SPPCs with several lattice periods and SPPC boundaries. The spatial separation of photonic/plasmonic signals with different wavelengths due to the wavelength dispersion within one eigenmode or due to coupling to several eigenmodes has been investigated, examining qualities like wavelength angular beam separation (WABS), passband and crosstalk. Effects such as SPP beam splitting and positive/negative wavelength dispersion at the vicinity of the bandgaps have been experimentally demonstrated. The effects of the SPPC Fabry-Perot cavities on the wavelength dispersion properties have been examined, by mathematically isolate the effect. The reduction of the cross-talk when the wavelength and polarisation modulation are combined is also shown.

In chapter 6 the spatial separation of four photonic/plasmonic signals linearly polarised with azimuth angles 0° , 45° , 90° and 135° using an SPPC is shown. The 4-level polarisation discriminator was also used to identify the S_1 and S_2 stokes parameters of 60 randomly elliptically polarised optical signals and was found in good agreement with a benchtop polarimeter. To achieve a full polarimeter functionality, i.e. identify the 3 Stokes

vector parameters, the concept of a novel fibre-coupled polarimeter, combining two 4-level polarisation discriminators with a high-birefringence fibre has been proposed. In this chapter we also discuss how the research described in this thesis inspired other scientists to develop miniaturised polarimeters based on metal-nanoslits and chiral devices or metasurfaces.

The conclusions and the future work are summarised in chapter 7. Appendices 1-7 contain the details on the derivation of the SPP dispersion relation and the SPP TM nature, the Green-tensor numerical model developed in Matlab to simulate the excitation of SPP waves through finite size SPPCs, the automation of the polarisation setting procedures, as well as essential details for the post-processing of the SPP intensity around the SPPCs far-field images, such as the identification of the SPPC and the angular resolution are presented at the appendices 1-7.

1.2 Original Contributions

The following original contributions to the field of plasmonics have been made in the course of this research work:

- A numerical model for finite size SPPCs based on the point-dipole approximation was developed and compared to experimental results [2] (chapter 4).

- The role of the SPPC boundary on the focusing of the outcoupling SPP beam under collimated illumination has been numerically and experimentally demonstrated (section 4. 3. 1),

- The beam splitting at the vicinity of the SPP bandgaps has been numerically and experimentally investigated [2-4] (sections 4. 3. 2 and 5.2) . It has been shown that depending the SPPC boundary the splitting ratio can be 1:1 and robust to the SPPC-illuminating spot centres misalignment or can be set to any random ratio by controlling the alignment between the SPPC centre and the illuminating spot centre [4]. The SPPC can also serve as a microscale alignment detector, with the intensity difference between the two prongs to indicate the misalignment between the two centres [4] (section 5.2). The angular separation between the two prongs can also be controlled by the SPPC boundary shape (section 5.2) [4].

- The positive/negative wavelength dispersion of the eigenmodes at the vicinity of the bandgap spectral area has been experimentally demonstrated, exploring its potential for dense wavelength demultiplexing applications (section 5.2)

- The effect of the substrate and SPPC boundary Fabry-Perot cavities on the SPPC wavelength dispersion properties have been investigated. It has been shown that the

substrate cavity can enhance the wavelength angular beam separation and decrease the cross-talk (section 5.2).

– A broadband wavelength demultiplexer, based on the simultaneous excitation of SPP eigenmodes at the two different metal dielectric interfaces of the SPPC has been experimentally demonstrated. The wavelength demultiplexer offered a 55 nm channel spacing, and a -1.55 dB-passband at least 20 nm wide. The wavelengths 1509 nm and 1564 nm were able to separate with a -3dB crosstalk (section 5.3)

– A compact, planar 4-level polarisation discriminator, able to uniquely spatially separate photonic/plasmonic linearly polarised signals with azimuth angles 0° , 45° , 90° and 135° , and identify the s_1 and s_2 stokes parameters of elliptical polarised photonic/plasmonic signals has been experimentally demonstrated. [5, 6, 52]. The concept was extended to provide full polarimetric functionality, i.e. to identify all 3 Stokes vector parameters s_1, s_2, s_3 , by proposing a novel microscale, fibre-coupled polarimeter based on the combination of 2 polarisation analysers and a $(n+1/4)L$ length of a high-birefringence fiber, where L is the HiBi beat length [6] (chapter 6).

1.3 List of Publications

1) **Maria-Ioanna Benetou**, “**SPPC Based Beam Splitter and Alignment Sensor: The Passive and Active Control of its Functionality Parameters**”, *Frontiers in Optics + Laser Science APS/DLS Conference Proceedings, Optical Society of America*, Washington, DC, p. JW3A.68, 2019

2) **Maria-Ioanna Benetou**, Jean-Sebastian Bouillard, Paulina Segovia, Wayne Dickson, Benn C Thomsen, Polina Bayvel, Anatoly V Zayats, “**Boundary effects in finite size plasmonic crystals: focusing and routing of plasmonic beams for optical communications**”, *Nanotechnology*, vol. 26, no. 44, p. 444001, 2015

3) **Maria-Ioanna Benetou**, Wayne Dickson, Benn C Thomsen, Polina Bayvel, Anatoly V Zayats, “**Microscale polarimeter based on a plasmonic crystal**”, *The 5th International Conference on Surface Plasmon Photonics Conference Proceedings (SPP5)*, Busan, Korea, p.135, 2011

4) **Maria-Ioanna Benetou**, Jean-Sebastian Bouillard, Wayne Dickson, Benn C Thomsen, Polina Bayvel, Anatoly V Zayats, “**Visualization of high-order plasmonic Bloch modes in square-lattice plasmonic crystal**”, *The 5th International Conference on Surface Plasmon Photonics Conference Proceedings (SPP5)*, Busan, Korea, 2011

5) **Maria-Ioanna Benetou**, Wayne Dickson, Benn C Thomsen, Polina Bayvel, Anatoly V Zayats, “**Four-level polarization discriminator based on a surface plasmon polaritonic crystal**”, *Applied Physics Letters*, vol. 98, no. 11, p. 111109, 2011.

6) **Maria-Ioanna Benetou**, Wayne Dickson, Benn C Thomsen, Polina Bayvel, Anatoly V Zayats, “**Surface plasmon polaritonic crystal polarisation demultiplexer**

for 4 level polarisation-shift-keying”, *Photon10 Conference Proceedings*, Southampton, UK, 2010

7) **Maria-Ioanna Benetou**, Wayne Dickson, Benn C Thomsen, Polina Bayvel, Anatoly V Zayats, “**Investigation of the effect of the boundary shape on the surface plasmon polaritonic crystal wavelength dispersive properties**”, *Institute of Physics, Plasmonics UK Meeting Proceedings*, London, UK, 2010

8) **Maria-Ioanna Benetou**, Wayne Dickson, Benn C Thomsen, Polina Bayvel, Anatoly V Zayats, “**Dispersive properties of surface plasmon polaritonic crystals with different boundary shapes**”, *IEEE Leos Annual Meeting Conference Proceedings*, Belek-Antalya, Turkey, 2009

9) **Maria-Ioanna Benetou**, Wayne Dickson, Polina Bayvel, Anatoly V Zayats, “**Surface plasmon devices for applications in optical communications and signal processing**”, *Institute of Physics, Young Researchers Meeting Proceedings*, London, UK, 2009

2. Theory of surface plasmon polaritons - polaritonic crystals

A hole in a screen is probably the simplest optical element possible, and was an object of curiosity and technological application long before it was scientifically analysed. In 1944 Bethe [53] treated the diffractive properties of an idealised subwavelength¹ hole in a perfectly conducting metal screen of zero thickness. According to his predictions, the optical transmission efficiency, normalised to the aperture area, scaled as $(r/\lambda)^4$, where λ is the wavelength of incoming wavelength and r the radius of the hole. Therefore, the optical transmission through a subwavelength hole would be very weak and drop rapidly as the wavelength λ becomes larger than the hole radius r . In 1998, T.W. Ebbesen et al [54], while exploring the optical properties of submicrometre cylindrical cavities in metallic films, observed extraordinary optical transmission that was challenging Bethe's predictions [53]. The arrays of such holes displayed highly unusual zero-order² transmission spectra, consisted of sharp peaks at wavelengths larger than the array period, beyond which no diffraction occurs³, and as large as ten times the diameter of the cylinder. At these maxima the light transmitted through the holes was more than twice the light impinging directly on the holes and orders of magnitude greater than what Bethe had predicted [53]. Such extraordinary transmission implied that even the light impinging on

¹ The size of the hole is small compared to the wavelength of the illuminating light

² The case where the incident and detected light are colinear

³ The condition for the first minimum in a diffraction pattern is $\sin\theta = \frac{\lambda}{d}$, where θ is the angle of diffraction, d the period of the array and λ the incident wavelength. When $\lambda > d$ diffraction does not occur and the expected pattern consisted of a single central maximum

the metal between the holes could be transmitted and the hole periodic structure was an active element, instead of a passive geometrical object in the path of the incident beam [41, 54]. Two important clues relating this phenomenon to surface plasmon polaritons (SPPs) come from the following observations [54]. First, the existence of the metallic was essential to observe the enhanced transmission. Indeed, the enhanced transmission was absent when the hole array was fabricated in Ge films. Second, when the metal film was present, the transmission spectrum was well defined with a set of enhanced transmission peaks determined by the periodicity. The positions of the maxima scaled exactly with the periodicity independently of the metal (Ag, Cr, Au), hole diameter and film thickness. The transmission spectrum also changed significantly with the type of lattice, for example whether the array was a square or a triangular lattice. In addition, the zero-order transmission spectra changed in a marked way even for small changes, such as 2° , in the angle of incidence. Indeed, the peaks changed in intensity and split into new peaks which moved in opposite directions. By recording the peak energies as a function of k_x they obtained the dispersion relation, which revealed the band structure of surface plasmon polaritons in the two-dimensional array. Such a behaviour had been observed when the light was coupling with surface plasmons in reflection gratings [55-58]. The connection of the extraordinary transmission of light through a periodic array of subwavelength holes and the surface plasmon polaritons excited at each metal-dielectric interface was theoretically established a couple of years later [59-61]. Surface plasmon polaritons are the efficient coupling of surface charges oscillations at the metal-dielectric interface, named surface plasmons, with light, and they are excited when their momentum ($k_{\text{spp-Bragg}}$) matches the component of the incident photon momentum in the plane of the periodic

array $k_x (=k_0 \sin\theta)$ [41, 56, 62]. The periodic hole array acts as antenna that couples light into surface plasmons, for given values of wavelength, by providing the necessary momentum conservation for the coupling process [54, 63, 64]. As a consequence, the electromagnetic fields at the surface become intense resulting in very high transmission efficiencies and a well-defined spectrum with resonant wavelengths determined by the periodicity. Implicit in the resonance conditions are the symmetry relations of the array. Therefore, the SPPs generated in the array will propagate along defined symmetry axes with their own polarization depending on the (i, j) number of the mode. Both surfaces on either side of the holes can sustain SPP modes offset from each other by the difference in ϵ_d of the material in immediate contact with the metal surface (typically glass and air). Since, the dielectric constants of metals are wavelength dependent, the choice of the metal depends on the wavelength to be used. Ideally, the dielectric constant of the metal should have a high absolute value for the real part and a small imaginary part that determines the absorption into the metal. This combination gives rise to high SPP fields at the surface and minimises the losses. The geometrical factors that influence the optical properties of the holes are numerous: symmetry of the structure, the aspect ratios and shape of the holes, aperture area, profile of the corrugations and so forth. These variables determine the electromagnetic field distribution on the surface, the propagation dynamics of the surface waves and their scattering efficiencies, and, the in-plane and out-of-plane coupling to light. The properties of these apertures can be tailored by structuring the metal with modern nanofabrication techniques.

When the transmission efficiency of the periodic subwavelength hole array- commonly referred to as plasmonic crystal- was measured as a function of the illuminating

light angle of incidence the result was band-diagrams. The band-diagrams were comprised by energy/momentum bands separated by gaps in which propagating states were prohibited. When the period of the nanostructure is half that of the effective wavelength of the SPP mode, scattering may lead to the formation of SPP standing waves and the opening of an SPP stop band [65, 66]. At frequencies within a bandgap, the density of SPP mode is zero-no SPP modes can be supported. However, at the band edges, the SPP mode dispersion is flat and the associated density of the SPP modes is high. Further, the nature of this flat band means that such modes can be excited by light that is incident over a wide range of angles, making them good candidates for frequency-selective surfaces [41].

Since the surface plasmon polariton (SPP) is a fundamental electromagnetic excitation mode on a metal-dielectric interface which is free to propagate along the metal surface, but its field decays exponentially in both media in the direction perpendicular to the interface, its field spatial distribution is inaccessible to the far-field optical techniques. Near-field mapping techniques have been essential for the development of SPP devices. The field spatial distribution of a SPPC was firstly measured by I. I Smolyaninov et al [67] in 1999 using near-field scanning optical microscopy.

The high confinement of the electromagnetic fields at the vicinity of the metallic surface through their interaction with the free electrons of the metal is responsible for their high enhancement and their enhanced sensitivity to the surface features and the dielectric medium in contact with the surface. The modern nanofabrication techniques allow us to tailor the dynamics of this combination by structuring the surface at the subwavelength scale. By altering the structure of a metal's surface, the properties of surface plasmons-

in particular their interaction with light, can be tailored; this combined with the simplicity with which the spectral properties of the periodic hole arrays can be tuned and scaled opens up a wealth of possibilities and applications from optical elements and new types of photonic devices to sensors for chemistry and biology.

Plasmonic crystals can act as filters for which the transmitted colour can be selected by merely adjusting the period of the structure [64, 68]. In addition to the numerous applications as part of photonic devices/optical networks, another promising application of plasmonic crystals is the realisation of structured colours. A palette of spectrally pure and bright colours can be obtained by controlling their geometries, dimensions, angle of incidence[68]. Surfaces decorated with structural colours have received tremendous attention because of their strong potential for a simplified mass production and the reduction of the number of materials used in the supply chain [68].

Numerous ways of actively tuning the lattice resonances have been investigated. Some of these involve choosing liquid crystals, such as E7 [69], or phase change materials, such as $\text{Ge}_2\text{Sb}_2\text{Te}_5$ (GST) [70], as the dielectric material to be in contact with the metallic surface and control their refractive index by applying electric field, optical pumping or thermal stimulus [71]. By altering the dielectric environment in contact with the metallic surface, the lattice resonances can be actively tuned.

Due to the combination of the large electromagnetic fields generated by the SPPs on the hole arrays and their sensitivity to the dielectric medium in contact with the metal, plasmonic crystals can also be used to enhance fluorescence and Raman scattering for biosensing [64, 72-77]. Plasmonic devices have been used for label-free, real-time that has greatly impacted medical diagnostics [78, 79], environmental monitoring and food

safety. Plasmonic crystals based sensors[80-82] can easily generate surface plasmon resonances using broadband, free-space illumination and can be made as a few tens of micrometres [83, 84] enabling the production of compact, multiplexed sensing chips.

This chapter provides some essential background knowledge on the surface plasmon polaritons and surface plasmon polaritonic crystals underpinning for the rest on this thesis.

2.1 Definitions of surface plasmons and surface plasmon polaritons

The free electrons of a metal surface can be treated as an electron liquid which oscillates on the metal surface, due to density fluctuations (plasma concept), and produces a TM electric field [56]. The quanta of these free electron oscillations are called surface plasmons [56]. Surface plasmons are always accompanied by an electromagnetic field, which is localised at the surface, i.e. it has a maximum at the surface and decays exponentially away from the surface (Fig. 2. 1. 1) [1, 41].

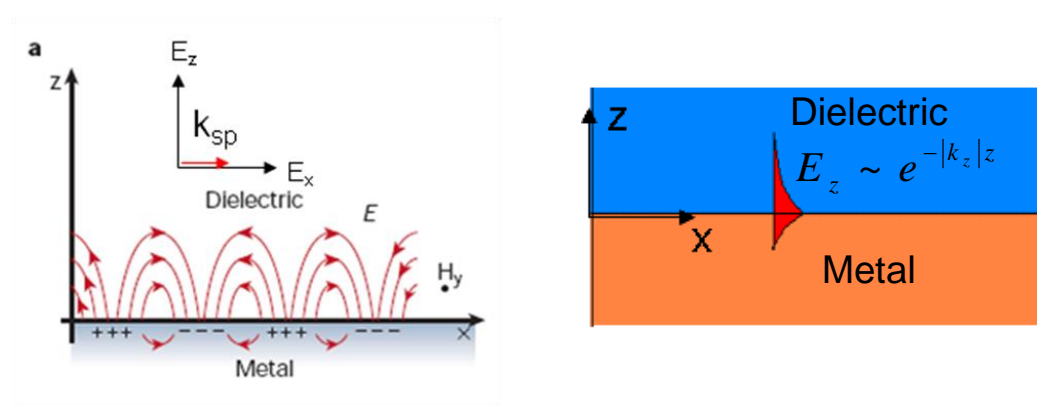


Fig. 2. 1. 1: Surface plasmons have an associated EM field localised at the surface [1, 41].

Starting from Maxwell's equations it can be shown that the surface plasmon (SP) dispersion relation is described by

Eq. 2. 1. 1, where ω is the frequency of the illuminating light and the surface plasmon, c the light velocity in vacuum or air, and ϵ_m and ϵ_d the dielectric constant of the metal and adjacent dielectric [1, 56, 85] (Appendix 1) and that surface plasmons can only be TM polarised [1, 56, 85] (Appendix 2).

$$|\vec{k}_{sp}| = \frac{\omega}{c} \sqrt{\frac{\epsilon_m \epsilon_d}{\epsilon_m + \epsilon_d}} \quad \text{Eq. 2. 1. 1}$$

2.2 Coupling light into surface plasmons

In order to couple two waves, these should have the same frequency (energy matching) and the same wave vector (phase matching). From the surface plasmon dispersion relation

(

Eq. 2. 1. 1) it can be seen that since $\text{Re}[\epsilon_m] < 0$, $\text{Re}[\epsilon_d] > 0$ and $|\text{Re}[\epsilon_m]| > |\text{Re}[\epsilon_d]|$,

$\text{Re}\left(\sqrt{\frac{\epsilon_m \epsilon_d}{\epsilon_m + \epsilon_d}}\right) > 1$ thus the surface plasmon wave vector (k_{sp}) is always greater than the

wavevector of a photon with the same frequency ω propagating in vacuum or air (Eq. 2.

2. 1), as illustrated in Fig. 2. 2. 1.

$$|\vec{k}_{ph}| = \frac{\omega}{c} \quad \text{Eq. 2. 2. 1}$$

Therefore, special coupling techniques, which would either increase the photon wave vector or decrease the surface plasmon wave vector, are required [1, 41, 43, 56].

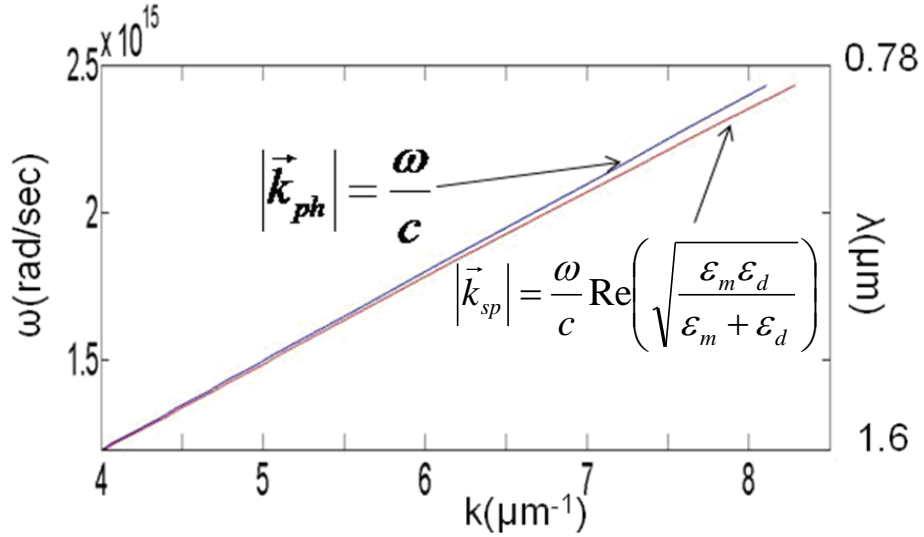


Fig. 2. 2. 1: Dispersion relation of a surface plasmon on a gold-air interface and a free-space propagating photon

One common technique to decrease the effective surface plasmon wave vector is to use Bragg gratings. Surface plasmon polaritonic crystals (SPPCs) are two dimensional Bragg gratings perforated on a metal-dielectric interface and they have been extensively used to couple light into surface plasmons [1, 54, 65, 86, 87].

The surface plasmon dispersion relation on the SPPC surface is modified due to the Bragg grating diffraction and can be analytically approximated, in the spectral areas away from the bandgap areas, by Eq. 2. 2. 2 [1, 69].

$$\overrightarrow{k_{sp_Bragg}} = \overrightarrow{k_{sp}} + p \frac{2\pi}{D_x} \hat{u}_x + q \frac{2\pi}{D_y} \hat{u}_y \quad \text{Eq. 2. 2. 2}$$

where p, q are integers related to the different diffraction modes, D_x, D_y the Bragg grating periods in the x - and y - directions, correspondingly, and \hat{u}_x, \hat{u}_y the unit vectors in the x - and y - directions.

For specific frequencies ω , eigenmodes, there are values of p and q for which

$$\vec{k}_{\text{ph}} = \vec{k}_{\text{sp_Bragg}} \quad \text{Eq. 2. 2. 3}$$

and photons are allowed to couple with surface plasmons producing surface plasmon polaritons (SPPs).

In the course of this work, SPPCs were used to couple light into surface plasmon waves and their potential use in wavelength and polarisation dispersion applications has been investigated. The SPPC samples, fabricated by Anatoly's Zayats research group, Department of Physics, were milled, using focusing ion-beam (FIB), in a 50 nm thick gold film, adhesioned on a 700nm glass substrate, using tantalum pentoxide (Ta₂O₅). The crystals were formed by circular holes of a 300nm diameter periodically perforated in a square lattice of several periods. A scanning electron microscopy (SEM) images of a 1500nm period SPPC is depicted in Fig. 2. 2. 2

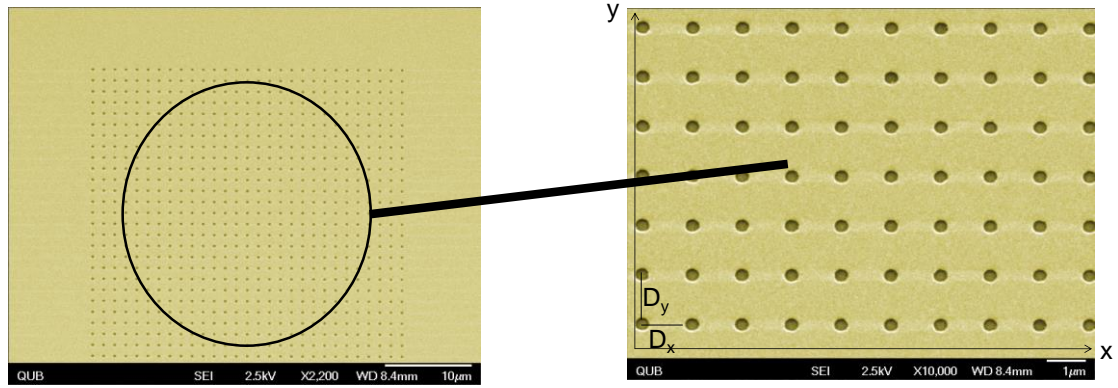


Fig. 2. 2. 2: SEM image of an SPPC sample ,1500nm square lattice, fabricated in the course of this work, by the collaborative research group, Anatoly’s Zayats research group

Fig. 2. 2. 3 (a) shows the surface plasmon dispersion relation on a smooth gold-air interface as calculated, in the course of this work, using Eq. 2. 2. 1, while the dispersion relations of the surface plasmon eigenmodes for $p=-3,-2,\dots,2,3$ and $q=0$ on a 1500nm period, square lattice SPPC , as calculated in the course of this work using Eq. 2. 2, have been plotted in Fig. 2. 2. 3 (b).

It can be observed that when the SP wavevector is equal to half the grating wavevector $\left(2K = \frac{2\pi}{D_x}\right)$ two eigenmodes of different p value cross each other, forming a SP bandgap [65]. Frequencies inside the bandgap cannot excite as the two eigenmodes cancel each other within the crystal. High eigenmode density and eigenmode flattening are experienced at the vicinity of the bandgap regions as it is illustratively represented at Fig. 2. 2. 4 [65]. This surface plasmon eigenmode flattening suggests that the SP eigenmode direction is strongly dependent on small changes of the SP wavelength; over

the last decades this has raised high expectations around the use of SPPCs as high resolution wavelength demultiplexers [48-50, 88].

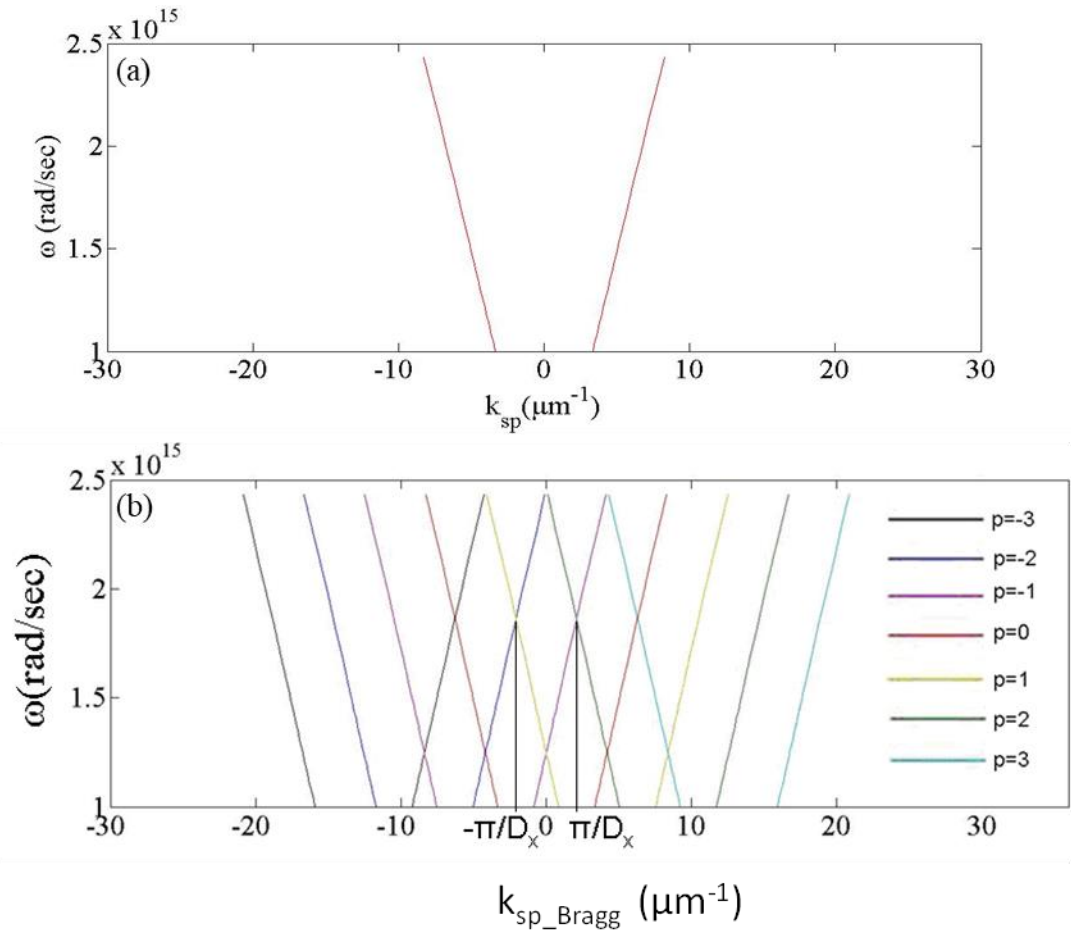


Fig. 2. 2. 3: Surface plasmon dispersion relation on a periodically perforated metal-air interface with a 1500nm period

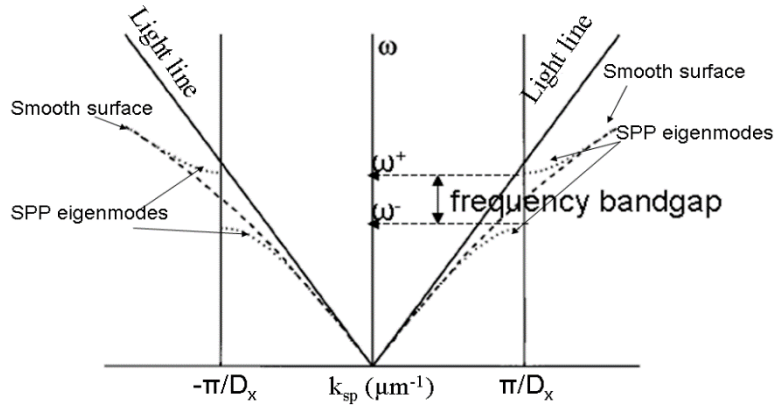


Fig. 2. 2. 4: Illustrative representation of SP bandgap and SP eigenmode flattening; the smooth surface dispersion relation splits into different eigenmodes forming a SP bandgapp. At the bandgap vicinity high eigenmode density and eigenmode flattening are experienced [65]

For specific frequencies ω , there are values of p and q for which

$$\vec{k}_{ph} = \vec{k}_{sp_Bragg} \quad \text{Eq. 2. 2. 4}$$

and photons are allowed to couple with surface plasmons producing surface plasmon polaritons (SPPs).

3. Analytical calculation of the SPP eigenmodes and their experimental verification

In this chapter the SPP eigenmodes and bandgaps at the Γ -X direction of SPPCs, comprised of 300 nm diameter circular holes, perforated in square lattices of various periods in a 50 nm thick gold film and attached on a glass substrate, have been experimentally identified and analytically calculated for horizontally polarised near-infrared illumination. The analytical calculation has been made by combining the approximate surface plasmon dispersion relation on the SPPC surfaces (Eq. 2. 2. 2) and the phase matching relation (Eq. 2. 2. 4). The experimental identification has been made by constructing the transmission dispersion of the samples measuring the SPPC transmission spectra for a range of angles of incidence. As it will be shown the analytical results match well the experimental ones.

3.1 Analytical Calculation of the SPP eigenmodes

In order for two waves to couple efficiently they need to have the same frequency (energy matching) and the same wavevector (phase matching). Thus, the SPP eigenmodes and bandgaps for any direction of an SPPC can be calculated combining the approximate SP dispersion relation on the SPPC surface (Eq. 2. 2. 2) with the phase matching relation (Eq. 2. 2. 4). The SPP eigenmodes for the Γ -X direction of square lattice SPPCs, with a

period D equal to 1400 nm and 1500nm, under horizontally polarised illumination have been calculated in the course of this PhD thesis as follows:

Starting from the phase matching equation (Eq. 2. 2. 4), we have that

$$\vec{k}_{spp_bragg} = \vec{k}_{o||} = k_{spp_bragg} \hat{x}$$

$$(Eq. 2. 2.2) \Rightarrow \vec{k}_{spp} = k_{spp_bragg} \hat{x} - p \frac{2\pi}{D_x} \hat{u}_x - q \frac{2\pi}{D_y} \hat{u}_y \Rightarrow$$

$$\Rightarrow \begin{bmatrix} k_{sppx} \\ k_{sppy} \end{bmatrix} = \begin{bmatrix} k_{spp_bragg} - p \frac{2\pi}{D_x} \\ (-q \frac{2\pi}{D_y}) \end{bmatrix} \Rightarrow$$

$$\Rightarrow (k_{spp})^2 = \left(k_{spp_bragg} - p \frac{2\pi}{D_x} \right)^2 + \left(q \frac{2\pi}{D_y} \right)^2 \Rightarrow$$

$$\xrightarrow{D_x=D_y=D} k_{spp_bragg}^2 - p \frac{4\pi}{D} k_{spp_bragg} + (p^2 + q^2) \left(\frac{2\pi}{D} \right)^2 - k_{spp} = 0$$

k_{spp_Bragg} is real only when $\Delta > 0$,

$$\text{where } \Delta = p^2 \left(\frac{4\pi}{D} \right)^2 - 4 \left[(p^2 + q^2) \left(\frac{2\pi}{D} \right)^2 - k_{spp} \right] \text{ and } k_{spp} = \text{Re} \left(\frac{2\pi}{\lambda} \sqrt{\frac{\epsilon_d \epsilon_m}{\epsilon_d + \epsilon_m}} \right)$$

For $\Delta > 0$ the k_{spp_bragg} was calculated using Eq. 3. 1. 1

$$k_{spp_bragg} = p \frac{2\pi}{D} \pm \frac{\sqrt{\Delta}}{2}$$

Eq. 3. 1. 1

The results of this calculation have been plotted for comparison with the experimental ones in Fig. 3. 3. 1.

3.2 Experimental Arrangement/Procedure

The transmission dispersion for the Γ -X direction of SPPCs comprised of 300 nm diameter circular holes, perforated in 1400 nm and 1500 nm square lattices in a 50 nm thick gold film deposited on a glass substrate was experimentally measured using the experimental arrangement shown in Fig. 3. 2. 1.

The SPPC samples were illuminated with horizontally polarised, collimated light, consisted of a continuous range of wavelengths in the near infrared (NIR) region ($\lambda= 798$ -1652 nm) and the transmitted power at the several wavelengths was measured as the angle of incidence was varied from 0° to 40° to the SPPC normal, in 2° steps. The illuminating beam was emitted from a white light source (tungsten-halogen lamp) and after passing through an aperture to reduce the beam diameter, it was collimated using a lens and horizontally polarised using an NIR polariser. In sequence it passed through an NIR filter (798 -1652 nm) which allowed only near-infrared components to be transmitted. The collimated, horizontally polarised, NIR light passed through another aperture to further reduce the beam diameter, and then through a microscope objective (x2), to refine the beam collimation, before illuminating the sample. The light transmitted through the crystal was collected with a microscope objective (20x, N.A=0.40, F=200mm), coupled to a fibre and then sent to a spectrometer (Triax 322).

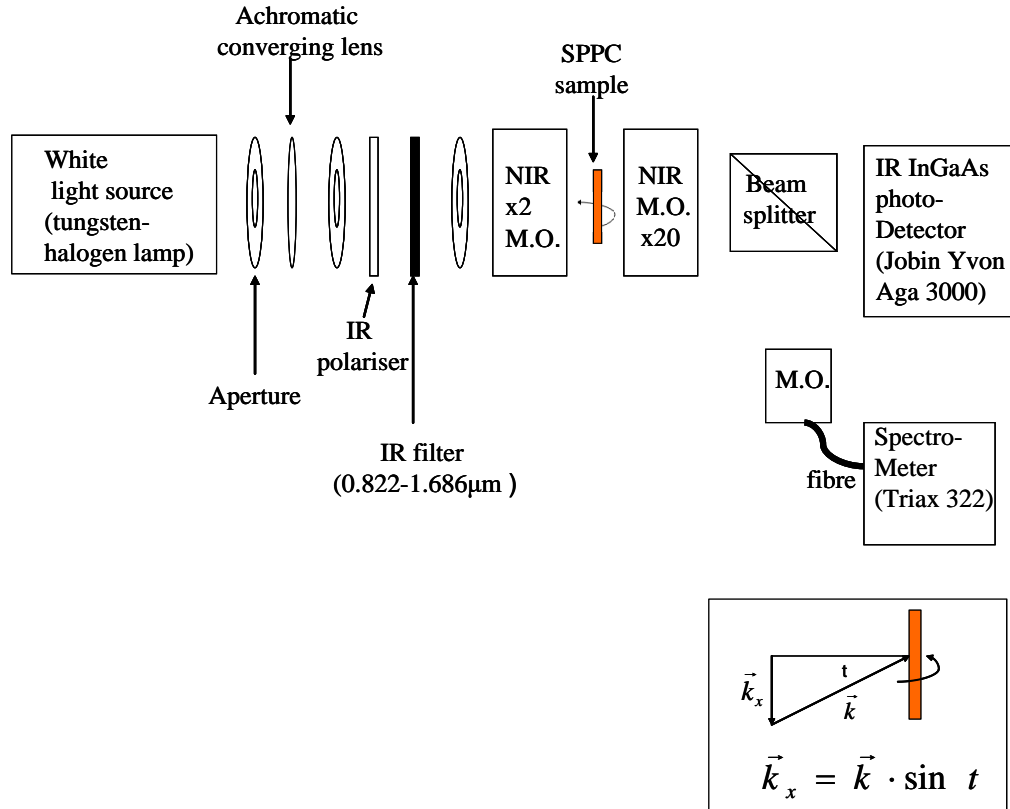


Fig. 3. 2. 1: Experimental arrangement to measure SPPC transmission spectrum. MO: Microscope Objective, (Inset: Geometry of the illuminating beam and the SPPC sample, \vec{k} : illuminating beam wavevector, \vec{k}_x : projection of the illuminating beam on the SPPC surface)

In order to verify that the light received by the spectrometer was actually the light transmitted through the SPPC sample, the light measured by the spectrometer was simultaneously imaged by an NIR camera (Jobin Yvon, AGA 3000), by placing a beamsplitter in front of the spectrometer.

Once the SPPC transmission spectra, $P_{SPPC}(\lambda)$, had been measured for the several angles of incidence, the SPPC was removed and the transmission spectrum without the SPPC, $P_{without_SPPC}(\lambda)$ was measured. The background illumination, $B(\lambda)$, i.e. power measured by the spectrometer when the white light source is off, was measured as well. The transmittance through the SPPC sample, $T(t, \lambda)$. for each illumination angle t and each wavelength component λ , was calculated using Eq. 3.1.1 .

$$T(t, \lambda) = \frac{(P_{SPPC}(t, \lambda) - B(\lambda))}{(P_{without_SPPC}(\lambda) - B(\lambda))} \quad \text{Eq. 3.1.1}$$

3.3 SPP Eigenmodes- Results and discussion

The Γ -X direction transmission dispersion spectra of the 1500 nm and 1400 nm period square lattice SPPCs, when these illuminated with horizontally polarised illumination are depicted in Fig. 3. 3. 1.

The SPP bandgaps can be observed as the dark areas where the eigenmodes cross and thus the SPP waves cannot excite. The eigenmodes can be seen as bright areas, at the vicinity of the bandgap, where the excitation of SPP waves is favored. The flattening of the eigenmodes at the vicinity of the bandgap can also be observed.

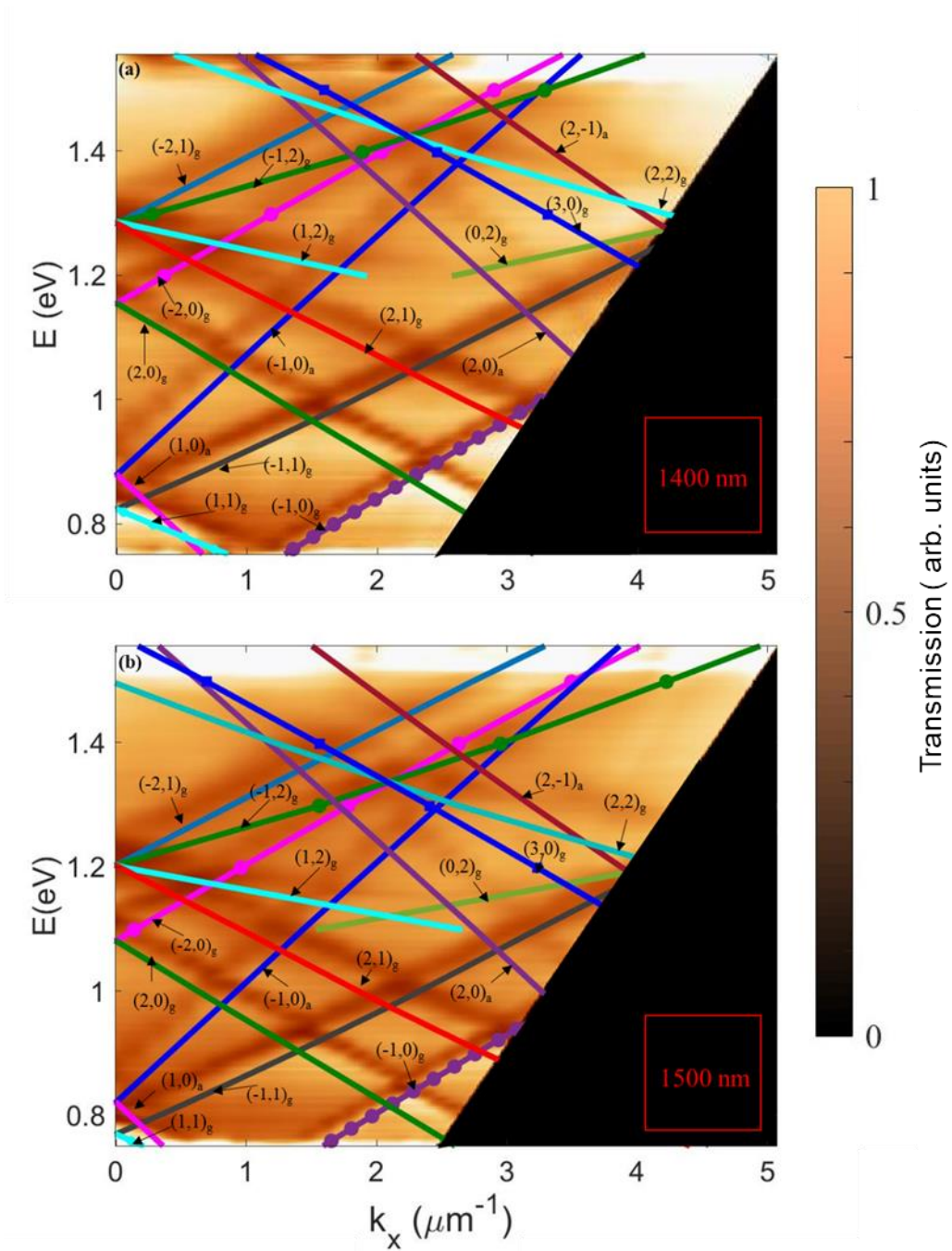


Fig. 3.3.1: Transmission dispersion of (a) a 1400nm and (b) a 1500nm period square lattice SPPCs when illuminated with horizontally polarised light. The eigenmode positions estimated from Eq. 3.1.1 are also shown (solid lines); notations “a” and “g” correspond to the modes of air-Au and glass-Au interfaces, respectively.

Since the illuminating light has to go through the SPPC holes before coupling to the eigenmodes at the glass-Au interface and experience the inevitable losses, the eigenmodes excited at the glass-Au interface appear darker than the ones excited at the air-Au interface. Due to the thickness of the gold film, 50 nm, there is no coupling between the eigenmodes at the glass-Au interface and at the air-Au interface.

The analytically approximated eigenmode positions, as calculated using Eq. 3.1.1 are also shown in Fig. 3.3.1 as solid lines and marked with the mode parameters p , q and the notations “a” and “g” which correspond to the modes of air-Au and glass-Au interfaces, respectively. It can be observed that the analytically calculated SPP eigenmodes are in good agreement with the experimentally measured ones.

Comparing the transmission dispersion for the 1400 nm period (Fig. 3.3.1 (a)) and the 1500 nm period (Fig. 3.3.1 (b)) it can be observed that the set of the eigenmodes excited for the two lattice periods, are the same, but wavelength shifted; the eigenmode set for the 1500nm period is shifted towards longer wavelengths compared to the ones excited for the 1400nm period. This agrees with the theoretical analysis presented in Ref. [65] and shows that by changing the SPPC period, the SPPC can be tuned to excite selected eigenmodes at preferable wavelengths.

3.4 Summary

The SPP eigenmodes and bandgaps at the Γ -X direction of SPPCs, comprised of 300 nm diameter circular holes, perforated in square lattices of various periods in a 50 nm thick gold film and attached on a glass substrate, have been experimentally identified

through the measurement of the transmission dispersion of the SPPCs at the Γ -X direction. The wavelengths at which the various eigenmodes are excited can be tuned by controlling the SPPC period. The eigenmodes and the bandgaps can be analytically estimated by combining the approximate surface plasmon dispersion on the SPPC surfaces and the phase matching relation; the analytical calculation is in good agreement with the experiment.

4. Visualisation of Bloch modes in finite size plasmonic crystals: Numerical Simulation & Experimental Verification

To date, the understanding of the optical properties of SPPCs has been achieved largely by considering infinite crystal lattices, with the role of the boundary shape being largely overlooked, despite its importance for applications in finite size plasmonic structures. Appropriate design of the boundary shape allows for the shaping of SPP beams coupled to the smooth metal film by controlling their refraction and their relative phase relations at the crystal boundary, which can be used for key telecommunication applications such as information demultiplexing or optimisation of device parameters, such as operation bandwidth and crosstalk.

In this chapter, the effects of the finite size SPPC boundary shape and the illumination parameters on the excitation of plasmonic beams under collimated and focussed illumination are described at the telecom wavelengths around 1550 nm. In this spectral range, the boundary effects and their applications can be investigated which is difficult to realise in the visible spectral range due to a shorter SPP propagation distance [89] .

Scanning near-field optical microscopy (SNOM) was used to experimentally visualise the near-field intensity distributions of plasmonic modes on and around the nanostructured metal films, and a numerical model based on the point-dipole approximation was developed to compare with the experimental results and explore the vast parameter space. By engineering the SPPC boundary shape and varying the

illumination parameters, control over the properties of the SPP beams excited by the structure can be achieved. Manipulation of the SPP beams lateral extension and propagation direction, in-plane focusing, SPP beam-splitting and refraction have also been demonstrated, opening the way for numerous on-chip applications.

4.1 Samples and experiment

The SPPCs under investigation were fabricated using focussed ion beam (FIB) milling in a 50 nm thick gold film deposited onto a glass substrate using magnetron sputtering⁴. The plasmonic crystals consisted of circular holes of 300 nm diameter periodically arranged in a square lattice with a 1530 nm period, optimised to excite SPPs at the telecom wavelength of 1550 nm. In order to investigate the effects of the SPPC boundary shape, both square and circular boundaries were considered, with 40 μm width and 40 μm diameter, respectively (Fig. 4. 1. 1 (c) and (d)).

The SPP band diagram of the plasmonic crystals (Fig. 4. 1. 1 (b)) representing the SPP Bloch modes supported by the lattice, was reconstructed from the measured zeroth-order far-field transmission spectra of the nanostructures under p-polarised collimated illumination and simulated using the empty lattice model [1, 69] . For the crystal size used in this work, the far-field transmission dispersion is independent of the crystal boundary shape and is essentially governed by the lattice parameters.

⁴ The SPPCs were fabricated by Wayne Dickson, member of Anatoly's Zayats research group

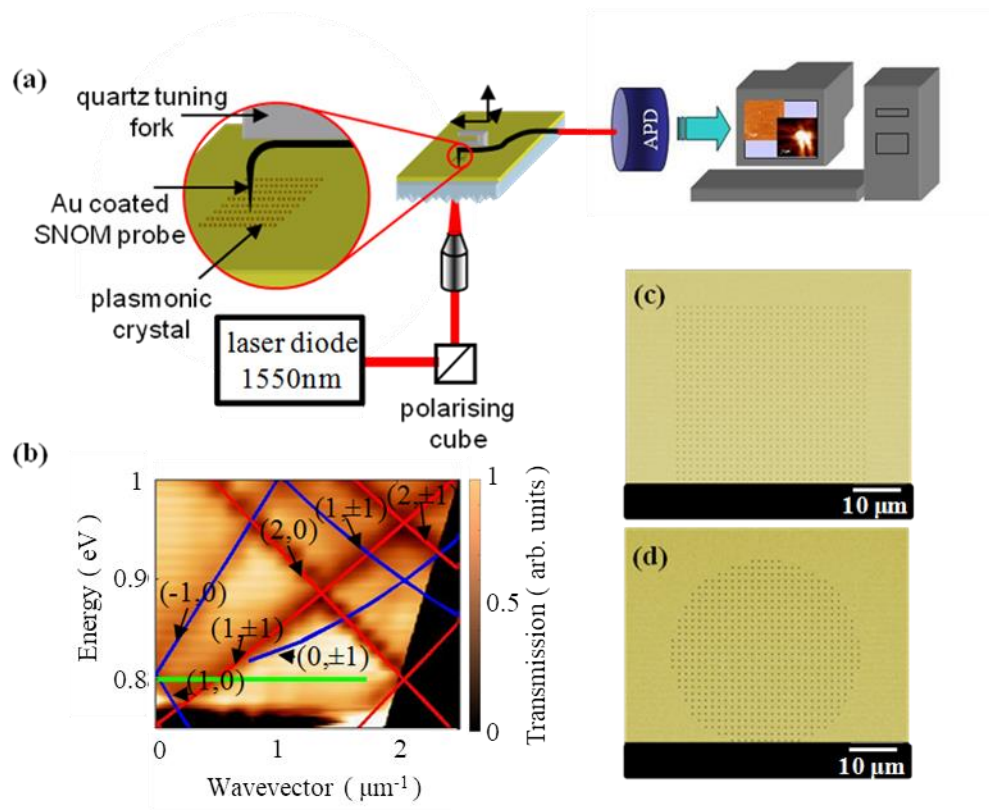


Fig. 4. 1. 1: (a) SNOM experimental arrangement⁵. APD: Avalanche Photodiode (b) Dispersion of the SPP modes on the crystal. The green line indicates the spectral range of wavevectors excited under the illumination with a 1550 nm focussed laser beam (NA=0.43). Blue and red lines represent the SPP Bloch mode positions calculated in the empty lattice model for Au–air and Au–glass interfaces, respectively. (c) and (d) Scanning electron microscope⁶ (SEM) images of the square and circular SPPCs, respectively.

⁵ Courtesy of Jean-Sebastian Bouillard, member of the Anatoly Zayats research group

The propagation of the SPP Bloch modes within the crystal, and their refraction at the boundary with the smooth metal film, were investigated by directly imaging them with SNOM⁶ [90] using the experimental arrangement shown at Fig. 4. 1. 1 (a). A laser diode, emitting at a wavelength of 1550 nm, was used to illuminate the SPPCs in transmission. The beam was expanded, collimated and polarised in the case of a collimated illumination, and a microscope objective with a numerical aperture (N.A.) of 0.43 was used in the case of a focussed illumination. The SNOM probe was a pulled and subsequently gold-coated 9.3 μm core standard single-mode optical fibre at the end of which a nano-aperture was created using FIB. The tapered end of the fibre was bent at 90° and mounted on a quartz tuning fork [90, 91] operating in a tapping mode. The light collected locally by the interaction of the SNOM probe with the near-field at the surface of the sample was then detected by an avalanche photodiode.

4.2 Numerical Model

The optical properties of SPPCs were simulated using the vectorial model for multiple SPP scattering in which surface scatterers are considered small spherical particles emitting as point-like dipoles [92-96]. The point-dipole approximation is based on the assumption of constant field inside a scatterer (spherical particle), which requires the radius R_p of the scatterer to be significantly smaller compared to the wavelength, and the inter-particle distances to be sufficiently larger ($>\lambda/2$), so that the excitation of higher-

⁶ The SNOM measurements were done by Jean-Sebastien Bouillard, member of Anatoly's Zayats research group

order multipolar components in the scattering field can be neglected [92-95]. The scatterers were simulated as small spherical particles with radius R_p ($=150\text{nm}$) and dielectric constant ϵ_m located in a reference system which consists of a dielectric with dielectric constant ϵ_d and a metal with dielectric constant ϵ_m and positioned in the dielectric half space at a distance $z_p=R_p$ from the metal-dielectric interface, the distance between the centre of the sphere at the metal-dielectric interface is equal to the radius of the sphere (Fig. 4. 2. 1).

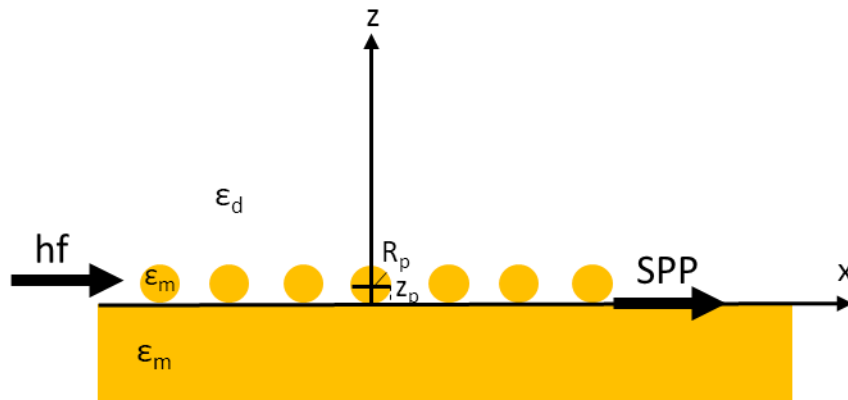


Fig. 4. 2. 1: Schematic representation of physical system: SPP wave is scattered by small metal spheres with radius R_p , and dielectric constant ϵ_m

In the electric point-dipole approximation, each of the scatterers is treated as a dipolar scatterer located at \vec{r}_p , the electric field at each of these scatterers was calculated by solving the $N \times N$ linear equations system represented by Eq. 4. 2. 1.

$$\vec{E}_{sc_i}(\vec{r}) = \vec{E}_{sc_i}^0(\vec{r}) + \frac{k_0^2}{\epsilon_0} \sum_{j=1, j \neq i}^N \underline{G}_{SPP}(\vec{r}, \vec{r}_p) \vec{p}_j \quad \text{Eq. 4. 2. 1}$$

where $\vec{E}_{sc_i}^0(\vec{r})$ is the incident SPP electric field at the position of the scatterer i , N the number of scatterers, $k_0 = 2\pi/\lambda$ the wavenumber in vacuum, ϵ_0 is the vacuum permittivity and $\underline{G}_{SPP}(\vec{r}, \vec{r}_p)$ is the dyadic Green's function of the reference system and \vec{p}_j the dipole moment of the particle.

The dipole moment of a small particle can be expressed as

$$\vec{p}_j = \underline{a}_d \vec{E}_{sc_j} \quad \text{Eq. 4. 2. 2}$$

where \underline{a}_d is the polarisability tensor accounting for the surface dressing effect, which can be calculated by

$$\underline{a}_d = a_0 \left(\frac{1}{1 + \xi\beta} \hat{x}\hat{x} + \frac{1}{1 + \xi\beta} \hat{y}\hat{y} + \frac{1}{1 + 2\xi\beta} \hat{z}\hat{z} \right) \quad \text{Eq. 4. 2. 3}$$

where

$$a_0 = \epsilon_0 \epsilon_d V_p 3 \frac{\epsilon_m - \epsilon_d}{\epsilon_m + 2\epsilon_d} \quad \text{Eq. 4. 2. 4}$$

V_p the volume of the particle,

$$V_p = \frac{4}{3} \pi R_p^3 \quad \text{Eq. 4. 2. 5}$$

β , the geometrical parameter of the surface dressing

$$\beta = \left[R_p / (2z_p) \right]^3 \quad \text{Eq. 4. 2. 6}$$

and ξ the material parameter of the surface dressing

$$\xi = \left[(\varepsilon_d - \varepsilon_m)(\varepsilon_m - \varepsilon_d) \right] / \left[(\varepsilon_d + \varepsilon_m)(\varepsilon_m + 2\varepsilon_d) \right] \quad \text{Eq. 4. 2. 7}$$

In the case where the distance along the interface between a source and an observation point is large, with both points being close to the surface plane (in comparison with the light wavelength in both cases), an analytical approximation of $\underline{G}_{SPP}(\vec{r}, \vec{r}')$ can be written in the cylindrical coordinates (Eq. 4. 2. 8).

$$\underline{G}_{SPP}(p, \varphi, z) = -\frac{i\alpha k_{SPP} H_0^{(1)}(k_{SPP} p) e^{-\alpha k_{SPP}(z+z')}}{2(1-a^4)(1-a^2)} \cdot \left[\hat{z}\hat{z} + a^2 \hat{p}\hat{p} + (\hat{z}\hat{p} - \hat{p}\hat{z})ia \right] \quad \text{Eq. 4. 2. 8}$$

where $\alpha = \sqrt{\varepsilon_d / (-\varepsilon_m)}$ and $H_0^{(1)}$ the zero-order Hankel function of the first-kind.

Once the electric field at the scatterers positions were calculated the electric field inside and outside the SPPC was calculated using

$$\vec{E}(\vec{r}) = \frac{k_0^2}{\varepsilon_0} \sum_{j=1}^N \underline{G}_{SPP}(\vec{r}, \vec{r}_p) \underline{a}_d \vec{E}_{sc_j} \quad \text{Eq. 4. 2. 9}$$

The SPP intensity was calculated using Eq. 4. 2. 10 .

$$I = |\vec{E}(\vec{r})|^2 \quad \text{Eq. 4. 2. 10}$$

Since the experimental dynamic range of the intensity values were limited, in order to better visualise the calculated SPP intensity maps on and around the SPPCs and qualitatively compare them with the experimentally measured ones, the calculated SPP intensities were mathematically saturated before plotted, such as the dynamic range of the calculated intensity values to be similar to the one provided by the experiment. The SPP excitation was investigated for the case of the x-polarised collimated illumination for which the incident electric field is a plane wave described by Eq. 4. 2. 11,

$$\vec{E}(\vec{r}) = E_0 e^{ikz} \hat{x} \quad \text{Eq. 4. 2. 11}$$

and the x-polarised strongly focused illumination at which the incident electric field is described by Eq. 4. 2. , where $s_x = \sin\theta \cos\varphi$, $s_y = \sin\theta \sin\varphi$, $s_z = \cos\theta$, θ the polar angle from the negative z axis, θ_{\max} the maximum incident angle, calculated from the numerical aperture of the illuminating system ($NA = n \sin\theta_{\max}$), φ the azimuth angle from positive axis x, ω_0 and f the beam waist and focal length of the focusing lens and k_0 the free space propagating wavenumber [97-100].

$$\left. \begin{aligned} E_x^m &= \int_0^{\theta_{\max}} \int_0^{2\pi} \exp[-f \sin \theta / \omega_o]^2 (\cos \theta)^{1/2} [\cos \theta + \sin^2 \phi (1 - \cos \theta)] \exp[ik_o (s_x x + s_y y + s_z z)] \cdot \sin \theta d\phi d\theta \\ E_y^m &= \int_0^{\theta_{\max}} \int_0^{2\pi} \exp[-f \sin \theta / \omega_o]^2 (\cos \theta)^{1/2} (\cos \theta - 1) \sin \phi \cos \phi \exp[ik_o (s_x x + s_y y + s_z z)] \cdot \sin \theta d\phi d\theta \\ E_z^m &= \int_0^{\theta_{\max}} \int_0^{2\pi} \exp[-f \sin \theta / \omega_o]^2 (\cos \theta)^{1/2} \sin \theta \cos \phi \exp[ik_o (s_x x + s_y y + s_z z)] \cdot \sin \theta d\phi d\theta \end{aligned} \right\} \text{Eq. 4. 2. 12}$$

The model was used to calculate the SPP distribution on the air-gold interface ($\epsilon_d=1$), while the dielectric constant of the gold was calculated from Eq. 4. 2. 13 where the $(n+ik)$ is the wavelength/frequency dependent refractive index of the metal [101]. The model was used to calculate the SPP distribution on the air-gold interface ($\epsilon_d=1$), while the dielectric constant of the gold was calculated from Eq. 4. 2. 13 where the $(n+ik)$ is the wavelength/frequency dependent refractive index of the metal [101]. The model was used to calculate the SPP distribution on the air-gold interface ($\epsilon_d=1$), while the dielectric constant of the gold was calculated from Eq. 4. 2. 13 where the $(n+ik)$ is the wavelength/frequency dependent refractive index of the metal [101].

$$\epsilon_m = (n + ik)^2 \quad \text{Eq. 4. 2. 13}$$

The model was developed in Matlab in the course of this thesis; the detailed calculations used in solving the NxN linear equations system are described in Appendix 3. In section 4.3, the low-order (collimated illumination) and multiple (strongly focused illumination) Bloch mode excitation is described, superimposing numerical simulations and experimental results, and focusing on the effect of the finite size and the boundary shape of the structure.

4.3 Results and discussion

4.3.1 Collimated illumination

The effects of the SPPC boundary shape on the coupling to SPPs on the smooth metal film were firstly investigated under linear-polarised plane wave illumination at normal incidence. Fig. 4. 3. 1. 1 shows the experimental and calculated near-field intensity distributions on and around the nanostructured area under such illumination conditions. The near-field intensity distributions have been calculated and plotted for both the case that the higher-order of multiple scattering among the holes/point scatterers is considered (Fig. 4. 3. 1. 1 (c) ,(h),(e),(k))) and the case it is ignored (Fig. 4. 3. 1. 1((b),(g) , (d), (i)).

Due to the homogeneous illumination across the whole SPPC, the SPP excitation is dominated by the first-order scattering of the incident field on the holes/point scatterers and the superposition of these scattered fields. The intensity of the scattered field from each individual scatterer is 5 orders of magnitude smaller than this of the incident field, leading the higher-order scattering among the holes/point scatterers to have little to zero effect on the excited SPP waves. At the SPP beam propagation direction, x-direction, the SPP distributions numerically calculated considering the higher-order multiple scattering (Fig. 4. 3. 1. 1 (c), (h), (e), (k))) are almost the same, exhibiting only fine details, with the ones calculated ignoring it (Fig. 4. 3. 1. 1 ((b), (g), (d), (i))). In addition, the parallel beams propagating at the y-direction, seen at (Fig. 4. 3. 1. 1 (c), (h), (e), (k))) due to the SPP higher order multiple scattering are not experimentally observed showing that the actual scattering efficiency of the SPPC holes is smaller than this of the dipole-like small metal spheres with which these are simulated with at the numerical calculations.

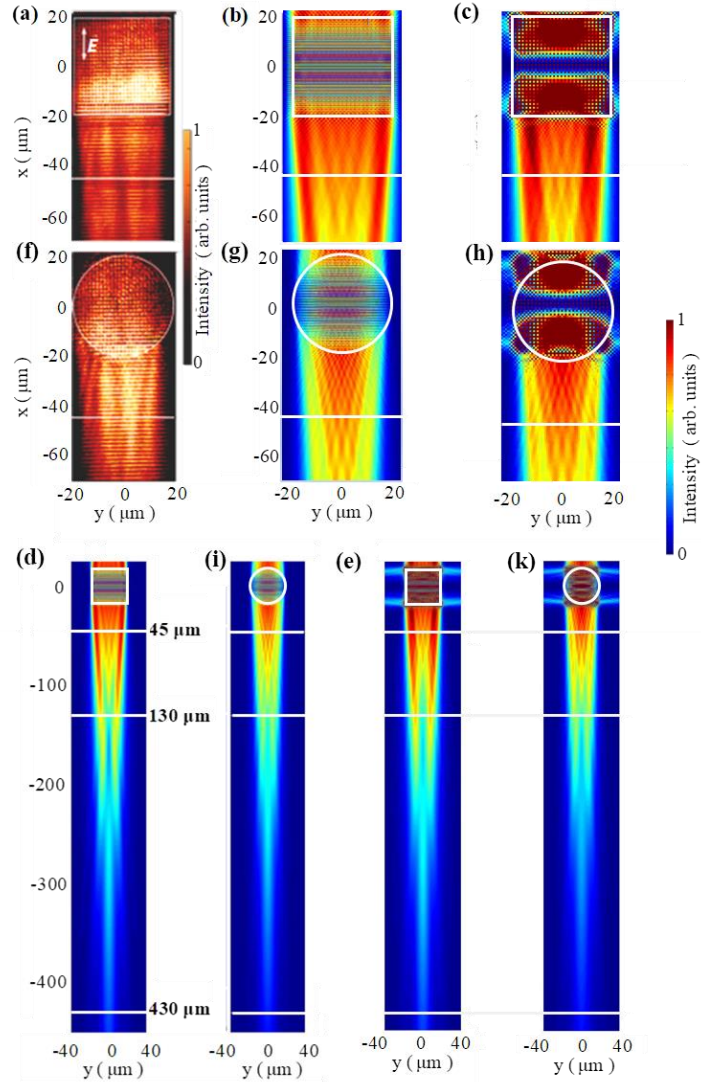


Fig. 4.3.1.1: (a,f) Experimentally measured and (b-e, g-k) numerically simulated SPP intensity distributions, (c, h, e, k)) considering and (b, g, d, i) ignoring the higher order scattering among the holes/scatterers, on and near the square lattice SPPCs with 1530 nm period for (a-e) square (40 μm width) and (f-k) circular (40 μm diameter) boundaries. The Collimated illumination wavelength is 1550 nm; polarisation is indicated in (a). White lines indicate the position of the cross-sections of the intensity distributions plotted in Fig. 4.3.1.2.

In both the experimentally measured (Fig. 4. 3. 1. 1 (a), (f)) and the numerically calculated SPP distributions (Fig. 4. 3. 1. 1 (b)-(e), (g)-(k)), the excitation of the counter-propagating $(\pm 1, 0)$ SPP Bloch modes, leading to the formation of the well-known standing wave pattern on the nanostructured area [93, 102, 103] and the SPP beams on the smooth metal film after refraction at the crystals' boundary can be clearly observed. The higher SPP intensity in the lower half of the structures observed in the experimental images (Fig. 4. 3. 1. 1 (a,f)), is due to a small deviation from the ideal normal incidence illumination conditions (a deviation of 1° is enough to result in preferential coupling to the one of the $(\pm 1, 0)$ modes as seen in Fig. 4. 1. 1 (b)). As a result, SPP modes travelling in the negative x direction were preferentially excited, resulting in an increased near-field intensity at the corresponding boundary. This does not, however, modify the eigenmodes of the crystal and the SPPs propagating on the nanostructured area are the well-defined $(\pm 1, 0)$ SPP Bloch modes. Consequently, their refraction at the boundary of the crystal and their propagation onto the smooth metal film is not affected.

The SPPC boundary acts as an interface where SPPs are either reflected back into the crystal or transmitted onto the smooth metal film after refraction. As a direct consequence of the finite size of the structures, focusing of the SPPs coupled onto the smooth metal film can be observed both experimentally and numerically (Fig. 4. 3. 1. 1). This focusing effect, illustrated by a reduction of the SPP beam waist with increasing distance from the crystal boundary, is the result of the interference between SPPs coupled onto the smooth metal film from different parts of the SPPC boundary, each with a different phase relation in a given propagation direction, defined by the boundary shape. Assuming N scatterers contributing to the field at a point P on a smooth metal film, the effect can approximately

be predicted analytically, describing the resulting electric field [52]: $E_P \sim \sum_{i=1}^N E_i(\vec{r}_i) / r_i^{1/2} e^{-i\vec{k}_{SPP}\vec{r}_i}$, where E_i is the electric field amplitudes at the i^{th} scatterer, \vec{r}_i is the coordinate of the i^{th} scatterer with respect to the observation point P , and \vec{k}_{SPP} is the SPP wavevector. Thus, the phases $\Delta\varphi_{ij} = \vec{k}_{SPP}|\vec{r}_i - \vec{r}_j|$ determine the interference process depending on the position of the scatterers at the boundary of one or another shape. If only several neighbouring scatterers at the boundary are involved, the phase changes are not significant enough to modify strongly the field distribution for different boundary shapes.

The numerically calculated beam profiles for the square and circular structures at several distances from the SPPC centre, along with the experimental SPP profile, measured at a distance of 45 μm from the crystal centre, are plotted in Fig. 4. 3. 1. 2. Whilst there are small differences between the experiment and model, the profile shape and its dependence on the boundary geometry is clearly close to the modelling results for either the cases that multiple scattering is considered or ignored; finer details of the experimental SPP profile can be recovered with higher accuracy when multiple scattering is taken into account. The focusing effect is highlighted further in Fig. 4. 3. 1. 2 (c) which depicts the experimentally measured and numerically calculated full-width half maximum (FWHM) of the SPP beam as defined in Fig. 4. 3. 1. 2 (a) for both the square and the circular SPPCs as a function of distance from the crystal centre. The width of the outcoupled SPP beam is smaller in the case of the circular boundary compared to the square boundary, but for both structures, the SPP beam width decreases as it propagates away from the structure. For smaller distances away from the SPPC centre, ($< 45 \mu\text{m}$ for square structure and $< 30 \mu\text{m}$ for circular structure), the experimental FWHM values are recovered better from the model that considers multiple scattering, while for bigger

distances the experimental values are recovered more accurately with the model that ignores the multiple scattering.

In order to compare the focusing properties of the two different boundary shapes in the context of on-chip signal processing, Fig. 4. 3. 1. 2 (d) shows the aperture size needed to collect 50% of the total SPP power as a function of the distance from the SPPC centre. It can be seen that a circular boundary exhibits a stronger effective in-plane focusing power, with a focal length of 346 μm and a 'depth of focus' (DOF) of 72 μm , compared to 450 μm and 82 μm , respectively, for a square boundary; the values have been extracted from the curves calculated ignoring the multiple scattering, as for long distances are the ones that fit better the experimental results. Here, the DOF is defined as the area over which the size of the detector required to detect 50% of the SPP power varies by less than 1% from its minimum value at the focal point. Interestingly, due to the complex beam profiles, defocusing of the SPP beam in both cases takes place at the same rate. The differences observed in the focussing of SPPs depending on the SPPC shape illustrate the necessity for adequate boundary engineering, such as varying the nanostructure shape and size which offers additional control over the generated plasmonic beams and provides opportunities for generating complex plasmonic beam shapes [89, 104-111]. In addition to the focusing aspect, multiple bottle-type SPP beams can be observed for both boundary shapes considered here, further illustrating the possible control over the phase of individual SPP beams coupled onto the smooth metal films. Such phase-controlled plasmonic beam formation was recently used for the generation of cosine-Gaussian and other non-diffracting SPP beams [108, 110]. However, whilst for the generation of such complex-beam-profiles and non-diffracting SPP beams specially designed geometries are

used to provide the required phase relations, the work presented here illustrates that careful engineering of the plasmonic crystals boundary can also be used for this purpose.

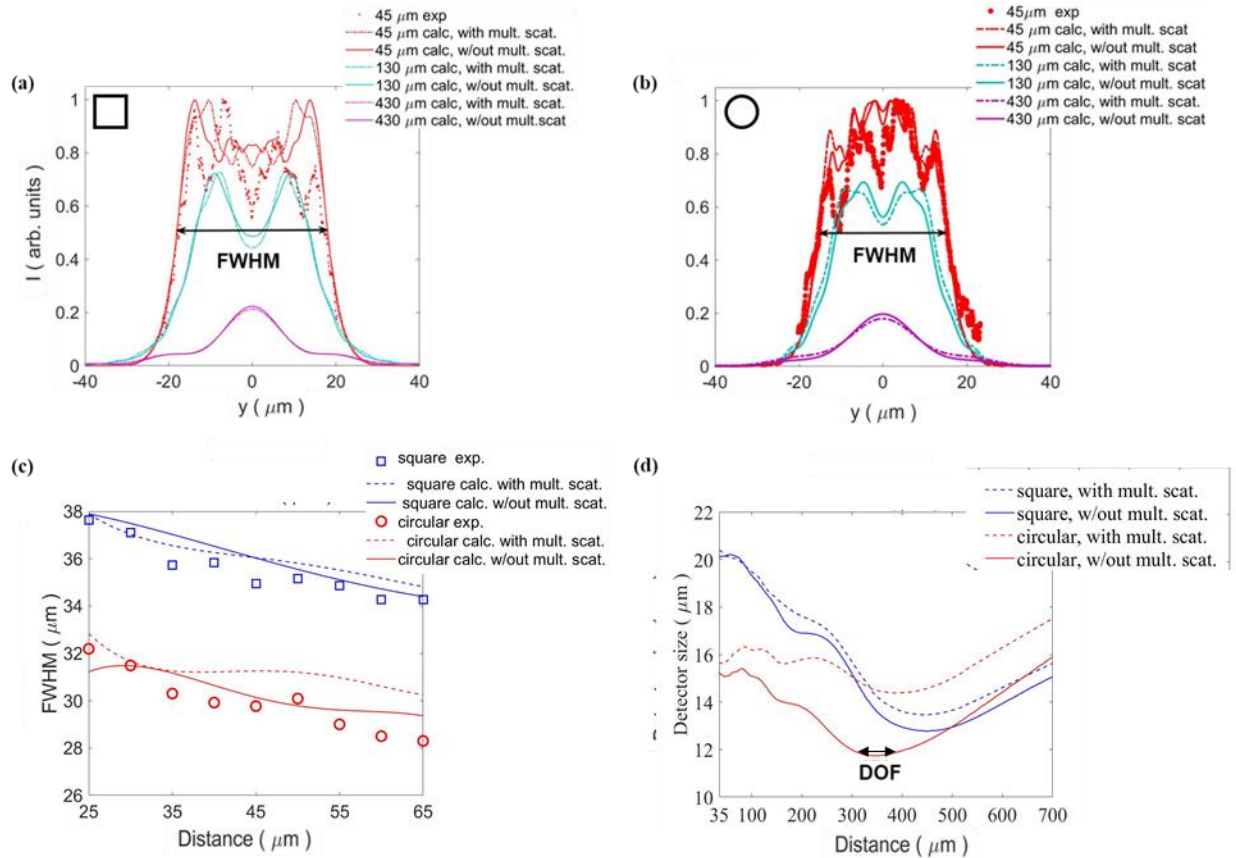


Fig. 4.3.1.2: (a), (b) Cross-sections of the SPP beams radiated by the square (a) and circular (b) SPPCs at several distances from the SPPC centre. Positions of the cross-sections are indicated with white lines in Fig. 4.3.1.1. (c) FWHM of the experimentally measured and numerically calculated SPP profiles as a function of distance from the SPPC centre. (d) The distance dependence of the minimum aperture size needed to detect 50% of the total SPP power (recalculated from the field distributions in Fig. 4.3.1.1).

4.3.2 Focused illumination

To increase control over the generated SPP waves and further explore the effects of the crystal boundary shape, focused illumination of a part of the SPPCs was studied. Such an illumination provides a localised source of SPP waves inside the crystal. SPP beams are excited and subsequently couple to the eigenmodes of the SPPC, dictated by the plasmonic band diagram of the structure [89]. This illumination scheme allows for the direct visualisation of the SPP beams propagating inside the nanostructured area followed by their refraction on the crystal boundary and coupling to smooth film SPP modes; as a result of the local illumination, 10 μm in diameter, and the subsequent filtering by the lattice, only the SPPs coupled to the crystal eigenmodes are incident onto the boundary [89].

To differentiate between the effects resulting from the reduced illumination spot size and from the larger incident wavevector spectrum provided by the focused illumination, one can consider a gedanken experiment with a narrow-beam collimated illumination with the spot size identical to the focused case (10 μm diameter). Despite being Fourier invalid, since the space confinement will inevitably introduce additional wavevector components, this artificial notion allows to probe the effects linked to the reduced illumination spot size independently of the mixing of the incident wavevectors. Using this artificial illumination scheme, the SPP distribution on the surface and in the vicinity of the SPPCs (square and circular), at the Au-air interface, was simulated and plotted in Fig. 4. 3. 2. 1.

The simulations were performed considering multiple scattering among the holes since the incident beam illuminated only a part of the SPPC.

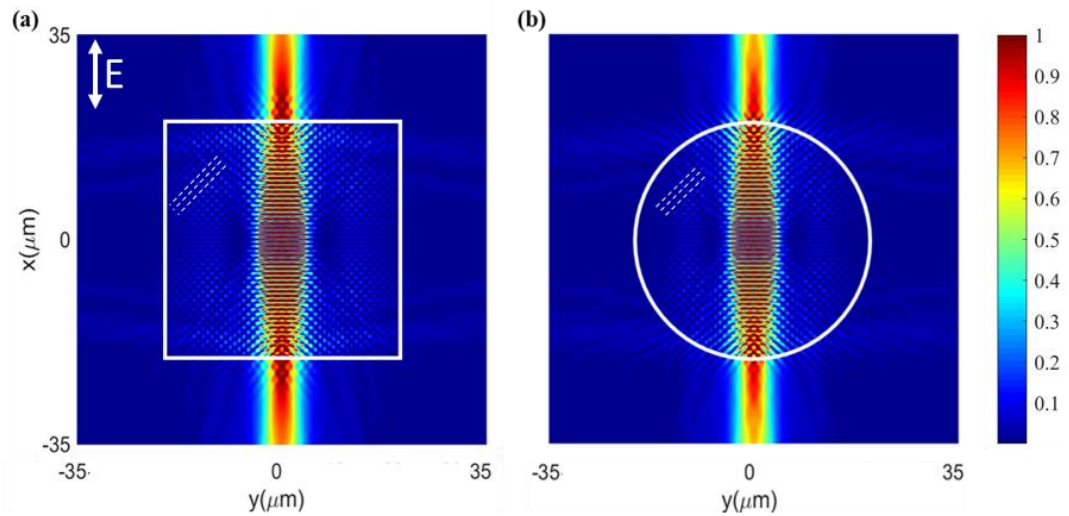


Fig. 4.3.2. 1: Numerically simulated SPP intensity on and near (a) the square (40 μm width) and (b) circular (40 μm diameter) SPPCs at the Au-air interface , when illuminated at the centre, with a collimated beam of a 10 μm diameter and 1550 nm wavelength. The polarisation of the incident light is indicated in (a). The parallel dashed lines mark the electric field intensity fringes (Fizeau fringes) formed by the SPPC boundary Fabry-Perot Cavity

In general, the spectrum of the populated SPP Bloch modes is defined by the overlap, in both the frequency space and the momentum space, of the in-plane scattering diagram of the illuminated scatterers and the SPP Bloch modes sustained by the nanostructured area defined by the plasmonic band-diagram of the crystal [89]. As a result, it can be seen that, independently of the illumination beam size, in the case of a collimated illumination, the same SPP Bloch mode spectrum is observed on the Au-air interface (Fig. 4.3.1.1 (b-

e, g-k) and Fig. 4.3.2.1). The size of the illumination spot, however, determines the number of elements of the crystal contributing to the generation of SPPs, directly influencing the width of the generated SPP beams. For a reduced illumination spot size, the narrow width of the generated SPP beams results in an interaction with a smaller number of scatterers at the crystal boundary, so that the phase-differences from the scatterers contributing to the SPP beam formation on the smooth film are negligible, resulting in near conventional, diffraction governed, SPP beam propagation, different from the complex SPP beams generated with a larger number of scatterers observed in Fig. 4.3.1.1. Furthermore, the reduced illumination spot size makes it possible to visualize the Fizeau fringes due to the Fabry-Perot cavity formed by the SPPC boundary, denoted in Fig. 4.3.2.1 as white dashed lines. The existence of such a Fabry-Perot cavity has been experimentally demonstrated along with its effect on the SPPC wavelength dispersion properties in section 6.2.

In addition to a reduced illumination spot size, the wide range of incident wavevectors present in the focussed illumination (Fig. 4.1.1(b)) results in the simultaneous excitation of a number of SPP Bloch modes propagating in different directions (Fig. 4.3.2.2 and Fig. 4.3.2.3). The complex angular distribution of the SPP beams generated for an off-centre illumination at a wavelength of 1550 nm as experimentally measured and numerically calculated is presented in Fig. 4.3.2.2 (a-d). It can be observed that the calculated near-field distributions reproduce the full range of beams observed experimentally (Fig. 4.3.2.2 (a,b)). The $(\pm 1, 0)$ and the $(0, \pm 1)$ eigenmodes, propagating in the x- and y-directions, respectively, are clearly visible. The relative coupling efficiency to each SPP eigenmode is directly related to the wavevector spectrum

and the polarisation states present in the illumination spot [5, 89], controlled by the illumination conditions. The corresponding SPP intensity distributions in the case of the central illumination are plotted in Fig. 4. 3. 2. 2 (e,f).

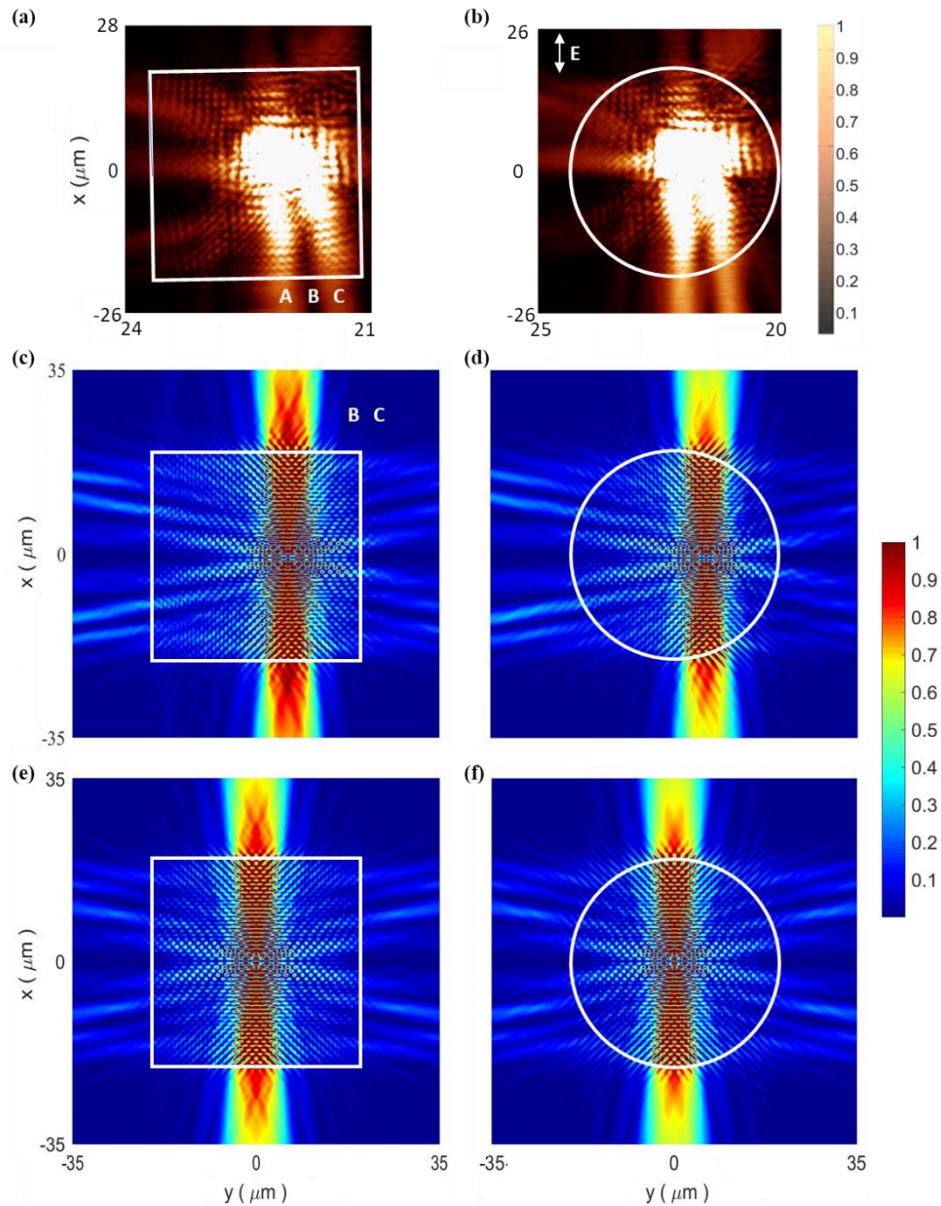


Fig. 4.3.2. 2: (a,b) Experimentally measured⁷ and (c-f) numerically simulated SPP intensity distributions on and near the square (40 μm width) and circular (40 μm diameter) SPPCs when (a-d) off-centre and (e-f) centrally illuminated with a focussed (N.A.=0.43) beam at 1550 nm wavelength. The polarisation of the incident light is indicated in (b).

⁷ Conducted by Jean-Sebastien Bouillard, member of Anatoly Zayats research group

It can be observed that displacing the illumination spot away from the SPPC geometrical centre has no effect on the spectrum of the excited SPP Bloch modes, governed by the illumination spot and the symmetry of the lattice. In the case of a centred illumination, the coupling efficiency in the two counter-propagating eigenmode parts is the same, while some variations are observed for the off-centred illumination.

Experimentally, the refraction is clearly observed in Fig. 4.3.2.2 on the boundary at larger angles. This opens a potential route for wavelength demultiplexing as, at this interface, SPP beams of different wavelengths will be refracted at different angles. In the simulations, the refraction is underestimated as the model uses dipoles positioned on smooth metal film to simulate the grating. As a result, the difference in effective refractive index between the nanostructured area and the smooth metal film is not as large as in the experimental case where the apertures are filled with air.

Comparison of the field distributions for the square and circular SPPCs shows much smaller differences than for the collimated illumination of the entire crystal (Fig. 4.3.1.1, Fig. 4.3.2.2). This is, as discussed above, a direct consequence of the reduced lateral width of the SPP beams excited under the focussed illumination conditions. Fig. 4.3.2.3 shows the numerically calculated SPP intensity around the square and circular structures, at a distance $29\ \mu\text{m}$ from the SPPC centre, for off-centred and centred illumination (Fig. 4.3.2.3 (a, c)), produced by taking annular cross-sections from the numerically calculated images Fig. 4.3.2.2 (c-f), and the corresponding experimentally measured SPP intensity for off-centre illumination around the square and circular SPPCs, $29\ \mu\text{m}$ away from the SPPC, (Fig. 4.3.2.3 (b, d)), extracted by taking annular cross-sections from the experimentally measured images shown in Fig. 4.3.2.2 (a-b).

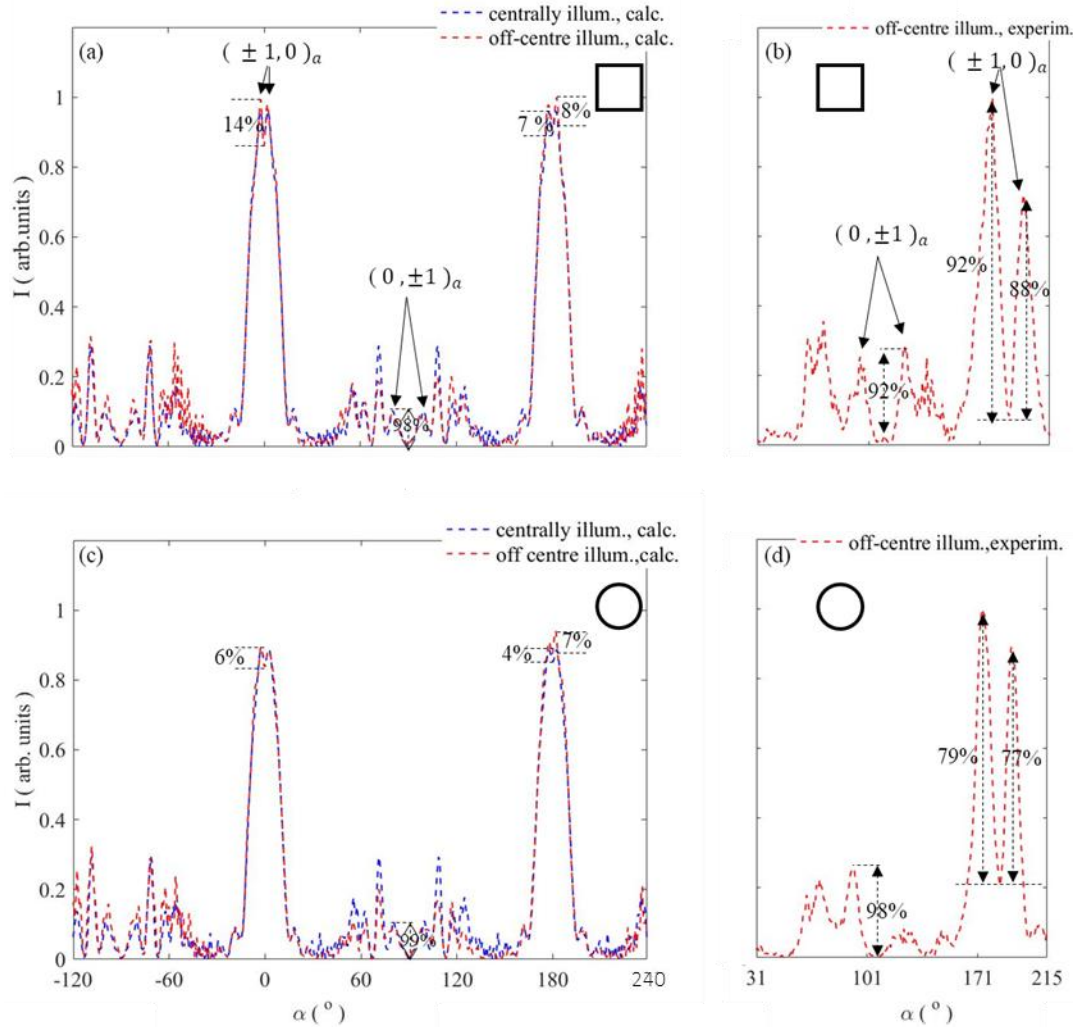


Fig. 4.3.2.3: (a,c) Numerically calculated and (b,d) experimentally measured cross-sections of the SPP intensity distributions around the square and the circular structures at a distance of 29 μm from the SPPC centre, when this is centrally/off-centre illuminated with strongly focused illumination (N.A:0.43) of 1550 nm wavelength

As expected, the $(\pm 1, 0)$ eigenmodes on the Au-air interface are excited with a higher efficiency due to the orientation of incident light polarisation. Both $(\pm 1, 0)$ and $(0, \pm 1)$

eigenmodes split into two parts, an effect referred to the bibliography as SPP forking [112]. The physical origin of the $(\pm 1, 0)$ Bloch mode splitting is different for this of the $(0, \pm 1)$ Bloch modes resulting to different values for the through-peak intensity ratios. For $\alpha = 0^\circ$, and $\lambda = 1550$ nm the $(\pm 1, 0)$ Bloch mode group velocity $\left(\frac{d\omega}{dk}\right)$ is zero (flat area in the Fig. 4.1. 1), resulting to the $(\pm 1, 0)$ Bloch modes to excite but not propagate at this direction, leading to the observed $(\pm 1, 0)$ Bloch mode splitting [112]. However, for any small $\alpha \neq 0^\circ$, the $(\pm 1, 0)$ Bloch mode is strongly coupled to, resulting, for a finite step of integration, to a small peak-through intensity difference. The SPP fork peak-through intensity difference can be controlled by the crystal boundary shape. In both the experiment and the simulation, the peak-through intensity difference is higher in the case of the square structure than the case of the circular structure. Since the scattering efficiency of the holes-scatterers comprising the crystal is smaller than the dipole-emitting small metal spheres used to simulate them in the numerical model, the peak-through intensity difference is much stronger in the experiment than the simulation. The peak-through intensity difference for the square structure is 88%-92% in the experiment (off-centred illumination), while in the simulation is 7% for central illumination and ranges from 6% to 14% for off-centre illumination. For the circular structure the peak-through intensity difference is 77%-78% in experiment (off-centred illumination) and in the simulation is 4% when centrally illuminated and 4%-7% for off-centred illumination.

On the other hand the $(0, \pm 1)$ Bloch mode splitting is due to the polarisation of the incident beam. Since the incident beam is x-polarised, SPPs propagating at $\alpha = 90^\circ$ and $\alpha = 270^\circ$ cannot be excited due to the inherent TM nature of the SPP waves; however, since the incident beam is strongly focused and contains a range of wavevectors the $(0, \pm 1)$

Bloch modes can excite/propagate at directions such as $\alpha = 99.5^\circ$ and $\alpha = 80.5^\circ$. This leads to the $(0, \pm 1)$ Bloch mode splitting with a through-peak intensity difference as strong as 92% in the experiment, 99% for off-centred and 98% for centred illumination in simulation for the square boundary crystal, while the corresponding values for the circular structure is 98% in experiment, 98% for off-centred and 99% for centred illumination in simulation. The peak-through intensity difference is slightly stronger in simulation, as in the experiment the measurement can be affected by impurities on the surface of the sample or by the small deviation from ideal normal incidence illumination conditions.

The angular beam separation of the parts of the SPP fork, on the surrounding smooth film, can also be manipulated by engineering the local boundary curvature at the points where these refract onto the smooth film. Such an effect can be useful for microbeam splitting applications including situations that nanostructures/ molecules with small spatial separation need to be targeted.

Whilst typically for complex beam-profile and non-diffracting SPP beam generation specially designed lattice geometries are used to provide the required phase relations, the discussion above illustrates how regular plasmonic crystals can be used for this purpose with a controlled illumination, via the generation of different SPP Bloch modes in the crystal. Moreover, as has been shown above, a focussed illumination allows for the excitation of multiple, spatially separated SPP beams at the same wavelength, propagating in multiple directions around a microscale SPPC.

4.4 Summary

A numerical model for finite size SPPCs based on the point-dipole approximation was developed and compared to experimental results. The role of the boundary shape and the illumination conditions on the generation of plasmonic beams by finite size SPPCs has been investigated in the telecommunication wavelength range around 1550nm. Significant differences were identified in the excitation of broad SPP beams by plasmonic crystals with the same lattice but with different boundary shapes. The origin of these differences was explained by the relative phase-relations between the individual SPP scatterers at the boundary of the crystal, leading to complex interferences on the smooth metal film. In the case of the slowly varying boundary shapes considered in this work, the effect of the phase difference introduced by the various parts of the boundaries diminish for narrow beams due to the limited portion of the boundary that they interact with. One can, however, envisage more complex boundary shapes that would make full use of this phenomenon for plasmonic beams with reduced lateral sizes. Using focused illumination, multiple narrow SPP beam excitation can be achieved at the same wavelength. The size, shape and lattice of SPPCs, as well as the illumination conditions, can be engineered to further manipulate the parameters of the generated SPP beams such as the beam width, focusing power, propagation direction and angular separation. This highlights a robustness and alignment-independent integration in applications combining SPP crystals with optical communication components.

5. SPPC Wavelength Dispersion Properties

Wavelength division multiplexing and dense wavelength division multiplexing (DWDM) allow to launch multiple channels with different wavelengths through one single optical fibre/waveguide. The information travelling down an optical fibre/waveguide is multiplied by the number of wavelength channels used and subsequently the communications cost is reduced. The wavelength demultiplexer is the device which at the user end will separate the channels from each other according to their central wavelengths.

The current focus for researchers is to design on-chip, miniaturised wavelength demultiplexers, with the smallest footprint, able to separate channels with ever decreasing interchannel spacing and minimal crosstalk. A number of miniaturised, integrated wavelength demultiplexers have been developed over the last years such as multimode interference (MMI) couplers/ slot waveguide structures [113-118], passive and actively controlled silicon and photonic crystal nanoring-resonators filterbanks [119-122], plasmonic nanocavities[123], Mach-Zehnder interferometers, plasmonic nanocavities[123], Mach-Zehnder interferometers [124], and Y-branch devices [125], photonic crystal fibre filled with high-index difference semiconductor materials [126], and Y-branch devices [125], photonic crystal fibre filled with high-index difference semiconductor materials [126].

The wavelength demultiplexers which are based on multimode interference couplers/ slot waveguide structures rely on their ‘self-imaging’ ability, i.e. the ability of a planar multimode waveguide to duplicate the input field at periodic intervals along its

propagation[116, 127-131]. As a direct result of the self-imaging in a planar waveguide the entrance facet images on the exit facet if the phase changes experienced by the various modes propagating from the entrance facet to the exit facet differ exactly or by small deviations of integer multiples of π or 2π . In general, for this condition to be satisfied the length of the multimode interference section L_{MMI} must be an integer multiple of $(3L_\pi)$, ($L_{MMI}=h(3L_\pi)$), where L_π is the beat length of the two lowest order modes given by Eq. 5. 1. [130]

$$L_\pi = \frac{\pi}{\beta_0 - \beta_1} = \frac{4n_r W_e^2}{3\lambda_0} \quad \text{Eq. 5. 1}$$

For even values of h the output image will be an exact image of the input, while if h is an odd number the output will be a mirrored/inverted image of the input. Therefore, two wavelengths λ_1 and λ_2 can be demultiplexed using a planar multimode interference waveguide if this is designed to operate at an odd order h for λ_1 and an even order h for λ_2 . The length of the multimode interference section can be reduced to $L_{MMI}=h \cdot L_\pi$ if every third mode ($v=2,5,8,\dots$) is reduced to zero [130]. One possible way of attaining such selective excitation is by launching an even symmetric input field $\Psi(y, 0)$, for example a Gaussian beam, at $y = \pm W_e/6$, where the modes $v=2,5,8,\dots$ present a zero with an odd symmetry [130]. Thus, the condition that needs to be fulfilled to demultiplex λ_1 and λ_2 , is described by Eq. 6. 2 [116, 117], where p natural and q odd integer. Fig. 5.1 depicts a schematic of such a planar multimode interference waveguide.

$$L_{MMI} = pL_{\pi}^{\lambda_1} = (p + q)L_{\pi}^{\lambda_2} \quad \text{Eq. 5.2}$$

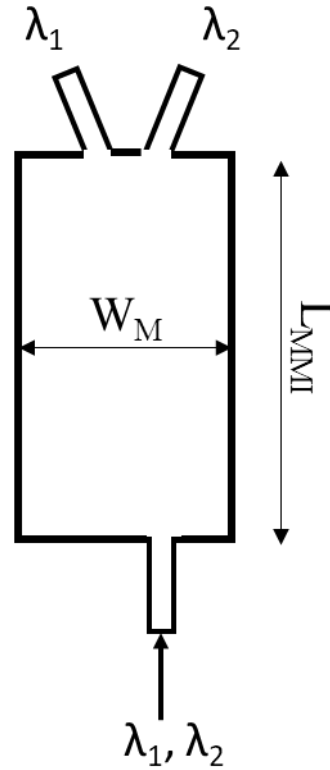


Fig. 5. 1: Schematic of self-imaging, multimode, planar waveguide

Such 1x2 multimode interference waveguides were cascaded to produce 1x4 [117] and 1x8 wavelength demultiplexers[118]. Indeed in 2015 D. Malka et al [117] suggested the cascade of three 1x2 slot waveguides to produce a 1x4 wavelength demultiplexer. Slot waveguides are comprised of a slot area of a low refractive index material (such as Alumina), between two areas of high-refractive index (such as silicon). This offers a high confinement of the light at the slot area, and thus a high power concentration in that area with no confinement losses [132]. In addition, slot waveguides, can be fabricated employing CMOS compatible materials and technology, enabling miniaturisation and

integration with electronic and photonic components in a silicon photonic chip [133]. The device had dimensions of 7.3 μm x 680 μm and was able to demultiplex the 1.4 μm , 1.45 μm , 1.5 μm and 1.55 μm wavelengths; the wavelengths were chosen to fit optical communications, and the alumina was chosen to be the slot material to fit the requirements for low absorption and low refractive index at the operating wavelengths. The insertion losses were below 0.7dB and the crosstalk below -8dB for all the four wavelengths while the linewidth was around 20 nm -22 nm.

In 2016 an 8-channel wavelength demultiplexer was proposed by cascading 7 multimode interference slot waveguide structures [118]. Instead of alumina, this time the slot material was chosen to be gallium nitride (GaN), surrounded again by silicon wafers. GaN has a lower refractive index than silicon, but a higher refractive index than silica. This combination was ideal for reducing the sensitivity of the device to the refractive index changes, which is crucial for devices with small channel spacing, while keeping the advantages of slot waveguides structures, namely high field confinement, minimised losses and short beat length, which enables the shortening/miniaturisation of the wavelength demultiplexer. The total length of the device was 6.6 mm and able to demultiplex 8 wavelengths, namely 1530 nm, 1535 nm, 1540 nm, 1545 nm, 1550 nm, 1555 nm, 1560 nm and 1565 nm, located at the C-band of optical communications, with a 5 nm channel spacing, low insertion loss⁸ (0.9-2.12 dB), low cross-talk⁹ (-19.97 dB - -13.77dB) , and 1.8-3.6 nm bandwidth.

⁸ Defined as $IL = -10 \log \left(\frac{P_w}{P_i} \right)$, where P_i is the power in the input waveguide and P_w the power at the desirable output waveguide port

⁹ Defined as $C.T_n = \frac{1}{N-1} \sum_1^{N-1} 10 \log \left(\frac{P_m}{P_n} \right)$, where N the number of channels , P_n the power transmission for the suitable channel and P_m the interference power transmission from the other port

Alternative geometries to rectangular planar waveguides are ring resonators. The resonance wavelength of ring resonators can be specified by engineering the geometrical parameters, namely the radius, the height and the width, and the effective refractive index. In 2004, V.R. Almeida et al experimentally demonstrated a silicon ring resonator whose resonance wavelength was shifting by actively control the free carrier- concentration, and subsequently the structure refractive index, using short, lower-power laser pump-pulses [119]. Although in general the silicon nonlinear optical properties are generally weak, they managed to enhance the light sensitivity to small refractive index changes by highly increasing the light-confinement in the structures. In 2011, M. S Dahlem et al, reported the fabrication of a reconfigurable filterbank, comprised of twenty channels, each based on two silicon-on-insulator microrings, eleven of which were precisely tuned to a specific frequency/wavelength and routing the corresponding signal into the respective drop port [120]. [119]. Although in general the silicon nonlinear optical properties are generally weak, they managed to enhance the light sensitivity to small refractive index changes by highly increasing the light-confinement in the structures. In 2011, M. S Dahlem et al, reported the fabrication of a reconfigurable filterbank, comprised of twenty channels, each based on two silicon-on-insulator microrings, eleven of which were precisely tuned to a specific frequency/wavelength and routing the corresponding signal into the respective drop port [120]. The resonant frequency/wavelength of each of these filters was specified by designing the radius of the ring, i.e. the optical path, and the width of the ring, which would determine the effective refractive index value; further thermo- optic control of the resonant frequency was offered by heating the microrings. The filterbank was designed to have 124 GHz (~ 1 nm) channel spacing, 20 GHz channel bandwidth and > 30 dB

extinction ratio at $\pm 80\text{GHz}$ from the channel centre. The crosstalk between the channels was -45 dB . In 2015, H. Alipour-Banaei et al proposed a passive two-dimensional, 4-channel wavelength demultiplexer based on four photonic crystal ring resonators. The resonance wavelengths were specified by designing the geometrical parameters, radius and lattice, of 4 cores-photonic crystal ring resonators [121]. The device offered a 3 nm channel spacing, high transmission efficiency ($> 95\%$) and high quality factor ($Q(=\lambda/\Delta\lambda)> 2600$). The bandwidth of each channel was 0.6 nm , while the cross-talk between the channels was less than -19 dB . Following this, C.-T. Wu et al, reported , in 2017 a metal-insulator-metal nanoscale ring resonator able to separate two communication wavelengths, namely 1310 nm and 1550 nm , based on the fact that the ratio of the orders of resonant transmittance peaks for two different high-order modes of the ring resonator is close to the ratio these two wavelengths and thus the resonance wavelengths of the nanoscale ring were able to be tuned to these wavelengths by varying its refractive index and its inner and outer radii [122]. The two wavelengths were able to demultiplex by couple in two different plasmonic waveguides. It is important to point out that although in the previous publications each ring resonator was filtering one wavelength, in this one, one ring resonator filters two wavelengths reducing the number of resonators needed to build a wavelength demultiplexer by a factor of two. The combination of the nanoscale ring resonator and the two plasmonic waveguides formed a wavelength demultiplexer with a -30 dB crosstalk and a 4 dB insertion loss¹⁰, demonstrating performance figures similar to conventional integrated optics demultiplexers in a nanoscale structure.

¹⁰ Defined as $IL=-10\log\left(\frac{P_w}{P_i}\right)$, where P_i is the power in the input waveguide and P_w the power at the desirable output waveguide port

Similar to the ring resonators, the resonance wavelength of a plasmonic nanocavity is also dictated by its geometrical features. In 2015 C. Lu et al experimentally demonstrated the demultiplexing of two wavelengths, namely 840 nm and 920 nm, with a 2.3 μm footprint assembly of 2 asymmetric multicomponent nanocavities on a slab Au/PVA/Air configuration, distributed on the left and right of a nanoslit [123]. Free space light is coupled into SPPs through the nanoslit and propagate right and left; if the SPP modes match the cavity modes, a large part of them will penetrate through the cavity and propagate forward, while the SPP modes that do not couple the cavity modes will be reflected. The device was offering a contrast intensity ratio between -10.3 dB and -13.7 dB, an operation wavelength band of 200 nm, was planar and easy to fabricate, while the splitting wavelengths could be easily adjusted by varying the structural parameters of the nanocavities.[123]. Free space light is coupled into SPPs through the nanoslit and propagate right and left; if the SPP modes match the cavity modes, a large part of them will penetrate through the cavity and propagate forward, while the SPP modes that do not couple the cavity modes will be reflected. The device was offering a contrast intensity ratio between -10.3 dB and -13.7 dB, an operation wavelength band of 200 nm, was planar and easy to fabricate, while the splitting wavelengths could be easily adjusted by varying the structural parameters of the nanocavities. Similar to the ring resonators, the resonance wavelength of a plasmonic nanocavity is also dictated by its geometrical features. In 2015 C. Lu et al experimentally demonstrated the demultiplexing of two wavelengths, namely 840 nm and 920 nm, with a 2.3 μm footprint assembly of 2 asymmetric multicomponent nanocavities on a slab Au/PVA/Air configuration, distributed on the left and right of a nanoslit [123]. Free space light is coupled into SPPs through the nanoslit and propagate

right and left; if the SPP modes match the cavity modes, a large part of them will penetrate through the cavity and propagate forward, while the SPP modes that do not couple the cavity modes will be reflected. The device was offering a contrast intensity ratio between -10.3 dB and -13.7 dB, an operation wavelength band of 200 nm, was planar and easy to fabricate, while the splitting wavelengths could be easily adjusted by varying the structural parameters of the nanocavities.

Another way to achieve miniaturised wavelength demultiplexing is using a silicon-nitride (Si_3N_4) photonic crystal fibre, as suggested earlier this year (2019) [126]. R. Dadabayev et al. demonstrated through simulations that red, green and blue (RGB) light can be demultiplexed after propagating 5.5 mm in a photonic crystal fibre, in which several air-holes had been replaced by Si_3N_4 rods. The photonic crystal fibre (PCF) structure was based on one input channel, air-holes zones, Si_3N_4 rods and three output channels. The PCF geometric parameters and the locations of the air-hole and the Si_3N_4 areas were optimised in order to obtain an efficient light coupling between Si_3N_4 neighbouring channels for the operating wavelengths while filtering out the other wavelengths in order to obtain the best insulation between the channels. The device was able to spatially separate red, green and blue light with low insertion loss (1.675-2.26 dB) and low crosstalk (-23.95 --20.77 dB)

In all the above papers, the design of the device was based on the specification of a few geometric parameters and the choice of the materials/ dielectric constants and resulted in devices with a fairly large footprint, of millimetres or hundreds of microns. A different approach to the design of low cost, small footprint, small channel spacing and low crosstalk wavelength demultiplexers is attempted over the last years from the group of

Prof. J. Vuchovic, department of electrical engineering, university of Stanford [134-139]. Their approach is to inverse design silicon photonics devices, including wavelength demultiplexers, by specifying a set of performance metrics, including the device area, input and output modes (eg. TE, TM, mode number), extinction ratio and insertion loss, or in other words specifying the coupling efficiencies between a set of input and output modes at various frequencies [140] , and allowing the model to navigate through not necessarily periodical structures towards the minimisation of the difference between the designed device performance and the required one. The model has been constrained to design structures that can be fabricated, having no smaller features that the state-of-art technology allows, and are robust to fabrication imprecision. To date , they have managed to design and experimentally test an $8 \mu\text{m}^2$ wavelength demultiplexer able to separate two wavelengths, 1300nm and 1550 nm, with wide bandwidth (>100 nm) [136], and a $24.75 \mu\text{m}^2$ three-channel wavelength demultiplexer, operating at optical communications, with 40 nm channel spacing, 1500 nm, 1540 nm and 1580 nm [138, 139]. Both devices have low peak insertion loss ($< 2\text{dB}$) and relatively low crosstalk (< -10.7 dB).

Despite the great progress towards miniaturised wavelength demultiplexers, made over the last years, micron scale demultiplexers able to separate signals with a couple of nanometers channel spacing have not been yet achieved. In chapter 3 we have seen that the SPPC eigenmodes flatten close to the bandgap areas, which means that for a small change in the SPP frequency/wavelength, the direction in which the eigenmode propagates should experience a large change. This is the concept which is at the heart of the next section (5.2) where the wavelength dispersion properties of SPPCs with a 1400 nm square lattice and two boundary shapes, namely square and circular, are investigated

at the vicinity of the SPP bandgap formed by the crossing of the $(0, \pm 1)$ eigenmodes at the Au-air interface. While in section 5.3 we experimentally demonstrate the simultaneous excitation of the SPP eigenmodes at the two metal-dielectric interfaces, Au-air and Au-glass, of the 1530 nm square lattice, SPPC sample described in chapter 4.

The SPP waves launching on the smooth metal film, surrounding the SPPC structures were imaged in the far-field using a high-sensitivity near infrared camera. To enable the SPP waves far-field imaging, the SPPC samples were surrounded by a 1.5 μm width and 60 μm (or 120 μm) internal radius scattering ring (shown in Fig. 5. 1. 1(inset)) , which was coupling the SPP waves back to light. Although the scattering efficiency of the scattering ring was not measured, due to the symmetry of the scattering ring, the ratio of the light intensity between any two points on the scattering is directly connected with the SPP intensity ratio between these two points. Thus the SPP intensities on two points of the scattering ring can be compared by comparing the light intensity at these two points.

The structures were characterised in terms of the wavelength angular beam separation, the passband, and the crosstalk as defined below

(i) Wavelength angular beam separation

If two SPP signals with wavelengths λ_1 and λ_2 propagate at angles α_1 and α_2 (Fig. 5.1) correspondingly, the wavelength angular beam separation (WABS) is defined as the ratio of the difference between their angular positions over their wavelength difference Eq. 5. 1 [48, 49].

$$WABS = \frac{\alpha_2 - \alpha_1}{\lambda_2 - \lambda_1}$$

Eq. 5. 1

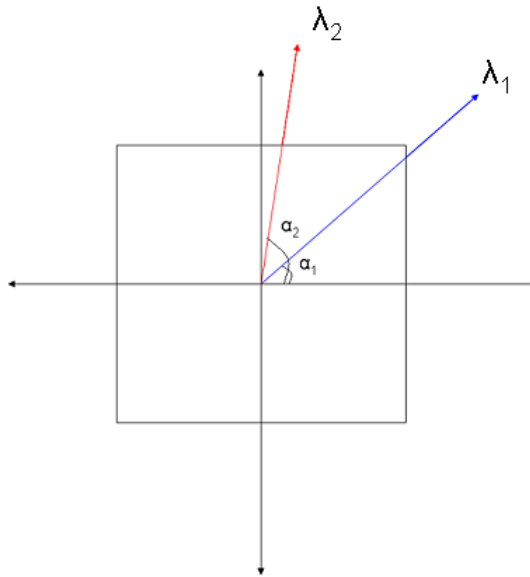


Fig. 5. 1: Schematic description of the wavelength angular beam separation

(ii) Full Width Half Maximum (FWHM)/ 3dB Passband

The full width half maximum (FWHM), also known as 3dB passband, is the wavelength/frequency range over which a value of one property, such as transmission, is above half of its maximum value, i.e. $\lambda_2 - \lambda_1$ (Fig. 5. 2).

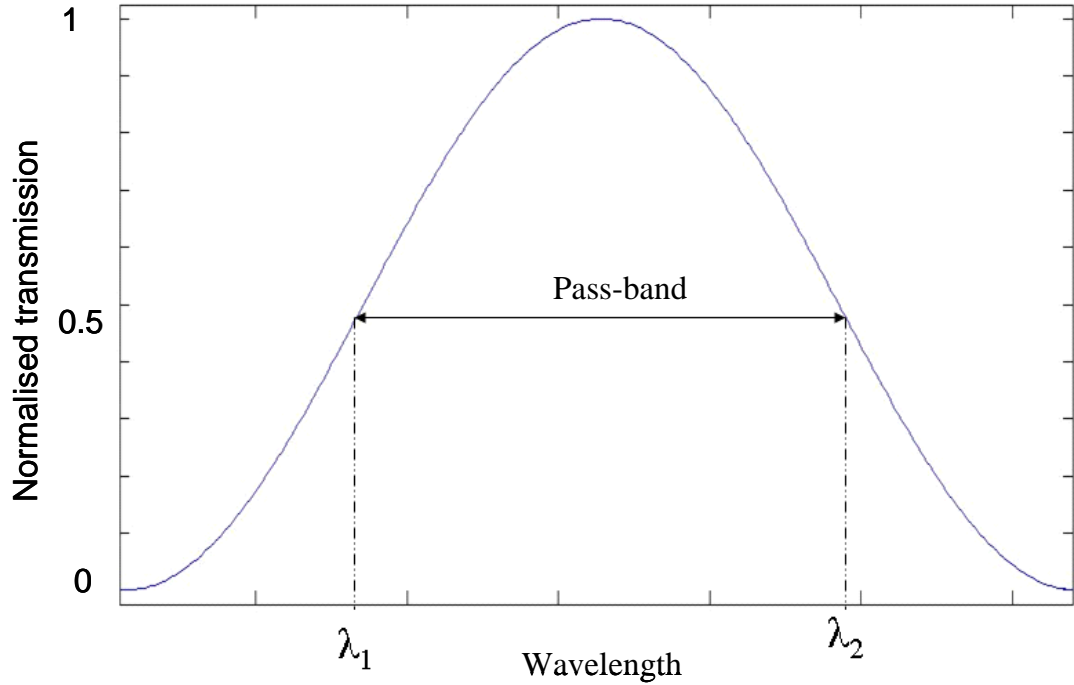


Fig. 5. 2: Schematic description of the passband

(iii) Crosstalk

“Crosstalk is the unwanted coupling between signal paths” [141]. If λ_1 and λ_2 are supposed to be detected at the directions ‘ α_1 ’ and ‘ α_2 ’ respectively. The crosstalk suffered by the signal propagated at the wavelength λ_1 , is the ratio of the λ_1 signal detected at the direction ‘ α_1 ’, over the λ_1 signal detected at the direction ‘ α_2 ’ (Eq. 5. 2). Crosstalk is the unwanted coupling between signal paths [141]. If λ_1 and λ_2 are supposed to be detected at the directions ‘ α_1 ’ and ‘ α_2 ’ respectively. The crosstalk suffered by the signal propagated at the wavelength λ_1 , is the ratio of the λ_1 signal detected at the direction ‘ α_1 ’, over the λ_1 signal detected at the direction ‘ α_2 ’. (Eq. 5. 2)

$$\text{Crosstalk (dB)} = 10 \log \left(\frac{P_{\alpha_2}(\lambda_1)}{P_{\alpha_1}(\lambda_1)} \right) \quad \text{Eq. 5.2}$$

5.1 Experimental Arrangement/Procedure

The experimental arrangement used for the characterisation of the SPPC wavelength dispersive properties is depicted in Fig. 5.1. 1.

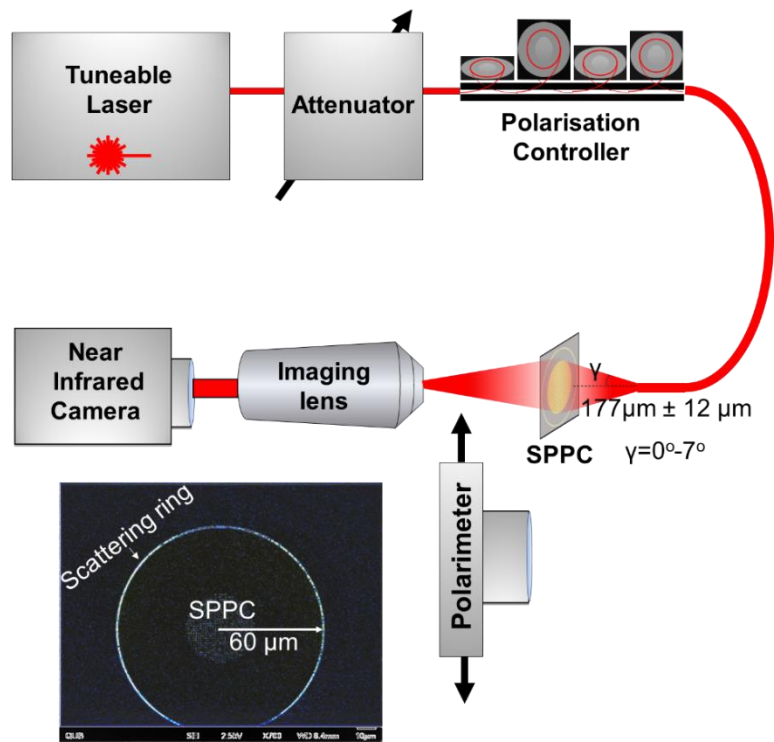


Fig. 5. 1. 1: Experimental arrangement used to investigate the SPPCs' wavelength dispersive properties

The SPPC samples, described at the previous chapter, with two values of period ($D_1=1400\text{nm}$ and $D_2=1530\text{ nm}$) were illuminated with monochromatic, polarised laser beam (Photonetics (1280-1345nm) or Anritsu (1499-1580nm) tuneable laser respectively)

using a single mode antireflection coated patchcord (NA=0.13) placed about $177 \mu\text{m} \pm 15 \mu\text{m}$ away from the SPPC sample. The distance between the patchcord and SPPC samples was chosen such that the illuminating light spot would be of the order of the SPPC size. Since the SPPCs had a $40 \mu\text{m}$ width, square boundary ones, or $40 \mu\text{m}$ diameter, circular boundary ones, the illuminating spot on the SPPC samples should be around $20 \mu\text{m}$ radius. According Gaussian optics the spot radius ω at a distance z from the end of the patchcord can be calculated using Eq. 5. 1. 1

$$\omega = \omega_0 \sqrt{1 + \left(\frac{z}{z_R}\right)^2} \quad \text{Eq. 5. 1. 1}$$

where ω_0 is the spot radius at the end of the illuminating patchcord, λ the illuminating light wavelength and z_R is calculated by Eq. 5. 1. 2.

$$z_R = \frac{\pi\omega_0^2}{\lambda} \quad \text{Eq. 5. 1. 2}$$

Taking into consideration that most of the optical power travelling through the optical fibre is confined at the core, the spot radius at the end of the fibre was assumed equal to the patchcord core radius, $\omega_0 = 4 \mu\text{m}$. The central wavelengths of the used lasers (Photonetics, Anritsu) were 1.3 and $1.5 \mu\text{m}$

$$\text{For } \lambda=1.3\mu\text{m} \xrightarrow{\text{Eq. 5. 1. 2}} z_R=39\mu\text{m} ,$$

$$\text{for } \lambda =1.5\mu\text{m} \xrightarrow{\text{Eq. 5. 1. 2}} z_R=34\mu\text{m}$$

$$(\text{Eq. 5. 1. 1}) \Rightarrow z = z_R \sqrt{\left(\frac{\omega}{\omega_0}\right)^2 - 1} \Rightarrow z = 164 \mu\text{m} - 189 \mu\text{m}$$

The reason for using an antireflection coated patchcord is that, during the characterisation of the SPPC wavelength dispersion properties, it was experimentally found that a non- antireflection coated patchcord led to the formation of a Fabry-Perot cavity between the patchcord and the SPPC. This Fabry-Perot cavity affected the wavelength dispersion properties characterisation by adding a sinusoidal component to the wavelength dependence of the SPP wave power detected at the surrounding defect ring, which was patchcord-sample distance dependent and not relevant to the SPPC wavelength dispersion properties. The use of an antireflection coated patchcord eliminated this Fabry-Perot cavity.

The range of angles over which the SPPC was illuminated can be calculated from Eq. 5. 1. 3.

$$\gamma = \text{asin}\left(\frac{N.A.}{n_0}\right) \quad \text{Eq. 5. 1. 3}$$

where N.A(= 0.13) is the patchcord numerical aperture, n_0 the refractive index of the medium surrounding the fibre, which in our case is air ($n_0=1$) and γ the maximum incident angle. Thus the illuminating range of angles were $\gamma=\pm 7^\circ$ deviation from the normal incidence.

Illumination of the SPPC samples with the appropriate wavelength and polarisation excites SPP eigenmodes on the SPPC surface. Some of the SPP waves couple immediately back into light, from the periodic corrugation of the SPPC itself, and contribute to the direct trasmission through the SPPC, and some travel towards the SPPC boundary where they refract, before launching on the surrounding smooth metal film. The SPP waves couple back to light when they reach the scattering ring. The far-field intensity on the

SPPC and the surrounding ring was imaged, using a microscope objective (x10), on a high dynamic range (1800:1) near- infrared camera (Goodrich SUI).

As shown in Fig. 5. 1. 2, the polarisation of the illuminating light was controlled using a polarisation controller and measured with a polarimeter which was mounted on a motorised translation stage to go in and out of the experimental arrangement. Since the SPPC samples and microscope objective were experimentally verified not to affect the transmitted light polarisation state, the illuminating light polarisation state was measured after the SPPC samples for convenience. An attenuator was used between the laser and the polarisation controller in order to allow the laser to work at an optimum laser output power but protect the sensitive infrared camera from damage due to overexposure.

In order to characterise the wavelength dispersion properties of a SPPC sample for a defined polarisation state, the SPPC was illuminated with -13 dB power, the illuminating light wavelength was varied in the wavelength range 1280 nm-1346 nm, using Photonics tuneable laser, for the characterisation of the SPPC samples with a 1400 nm period or in the wavelength range 1499 nm - 1580 nm, using Anritsu tuneable laser, for the characterisation of the SPPC samples with a 1530 nm period with a 0.005 nm resolution. The light intensity, which as mentioned before, is directly connected with the SPP intensity, on the SPPC and the scattering ring was imaged on the infrared camera for each value of the illuminating wavelength.

Since the dispersion properties are both wavelength and polarisation dependent, during the characterisation of the wavelength dispersion properties the polarisation of the illuminating light was kept constant within 0.009 Stokes vector precision, i.e.

$$|\vec{S}_m - \vec{S}_d| \leq 0.009 \quad \text{Eq. 5. 1. 4}$$

where \vec{S}_m , the Stokes vector of the measured polarisation state and \vec{S}_d the Stokes vector of the desired polarisation state. A Stokes vector deviation of 0.009 would allow a 0.005 deviation for each of the s_1, s_2, s_3 parameters. Since the polarisation state of the illuminating laser beam depends on the temperature, on mechanical movement, but more importantly on the wavelength itself, the polarisation state was checked and adjusted to fulfil Eq. 5. 1. 4 every 1 nm, which was experimentally tested to be the maximum wavelength change before the wavelength dependence of the polarisation controller resulted in a change in a possible polarisation change. During the characterisation of the SPPC samples, every 1 nm step the polarimeter was moved into the experimental arrangement between the microscope objective and the camera, and the polarisation state of the illuminating light was measured and adjusted to the desired polarisation state if needed. After that, the polarimeter was moved out of the experimental arrangement in order to allow the capture of the SPP wave far-field distribution on the crystal and the defect ring.

The SPPC transmittance was calculated by dividing the transmitted power when the light is going through the SPPC sample, minus the background, with the transmitted power measured when the SPPC is removed from the path, minus the background, for each wavelength value, as described in chapter 3 (Eq. 3. 1. 3).

The whole experimental procedure had been automated using Labview. Most of the automation steps were straight forward, but the algorithm for setting up/optimising the

desired polarisation state was developed during the course of this work and is described in appendix 4.

5.2 Dense Wavelength Demultiplexing and Power Beam Splitting

The wavelength dispersion properties of SPPCs with a 1400 nm period square lattice, and either square or circular boundary were characterised following the procedure described in 5.1. Once the far-field intensity images were acquired, in order to recover the intensity distribution on the object plane, i.e. on the SPPC and the scattering ring itself, the obtained images were inverted with respect to the optical axis¹¹. Images of the SPP intensity distribution around the square and circular boundary SPPCs when illuminated with 1323 nm vertically polarised light are shown in Figs. 5. 2. 1 (a,b) . The images are saturated at the central area, SPPC nanostructured area, due to the direct light transmission through the crystal. The light observed around the angular positions $\alpha = 90^\circ$ and $\alpha = 270^\circ$ at the scattering ring is related to the SPP waves that excite on the SPPC surface, propagate into the smooth metal film after refracting on the SPPC boundary, and scatter into light so it can be imaged on the far-field. This indicates that the excited SPP eigenmodes are the $(0, \pm 1)$ on the Au-air interface, as expected from the transmission dispersion of the SPPCs plotted in Fig. 5. 2. 2 (c) and depicting the spectral area illuminated during the wavelength characterisation; the transmission dispersion and the spectrum of the excited eigenmodes do not depend on the SPPC boundary. In theory the SPP signal around the

¹¹ If the object is in a greater distance from a converging lens than its focal length, the image is real and inverted by the optical axis.

angular positions $\alpha = 90^\circ$ and $\alpha = 270^\circ$ should have the same power, any difference in power between the two is due to small vertical misalignment between the SPPC centre and the centre of the illuminating beam.

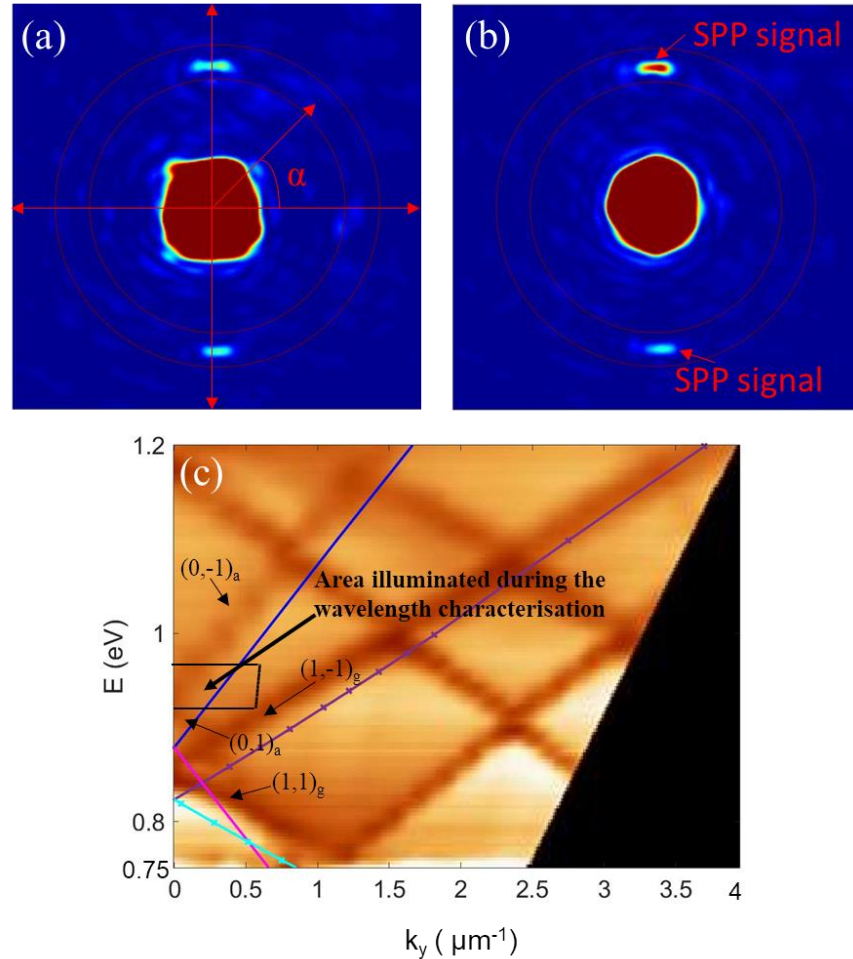


Fig. 5. 2. 1: Far-field images of the SPP intensity distribution around the 1400 nm period square lattice SPPC with (a) square and (b) circular boundary , when illuminated with 1323 nm vertically polarised light (c) Transmission dispersion of the 1400 nm period SPPC-the solid lines show the theoretical eigenmodes as calculated in section 3.1; the spectral area illuminated during the wavelength characterisation is also shown

To calculate the wavelength-dependent SPP distribution around the SPPC, the SPPC centre was first identified, as described in appendix 5, and the image was transformed into polar coordinates. Then a circular washer was defined at the scattering ring position, as shown in Figs. 5. 2. 2 (a,b) , and the SPP intensity was integrated over angular sections of 0.7° , which was the arc corresponding to one camera pixel and thus the smallest possible angular resolution (the detailed calculation is shown in appendix 6). The SPP transmittance as a function of the angular position α and the illuminating wavelength λ , was calculated as the ratio of the SPP power detected at each angular position for each illuminating wavelength value, over the detected power without the SPPC.

Fig. 5. 2. 2 shows the normalised SPP transmittance distribution as a function of the illuminating wavelength and the angular position α around SPPCs with a 1400 nm period square lattice, and circular and square boundary as measured when illuminated with a non-AR coated patchcord (Fig. 5. 2. 2 (a,d)), when fibre-sample cavity is mathematically filtered out (Fig. 5. 2. 2 (b,e)). The fine interference pattern seen in Fig. 5. 2. 2 (b, c) is due to the Fabry-Perot cavity formed between the two facets of the glass substrate (effective cavity length $1050 \mu\text{m} \pm 13 \mu\text{m}$). Fig. 5. 2. 2 (c,f) shows the normalised SPP transmittance distribution when the fibre-sample and substrate cavities are mathematically filtered out. The remaining coarse interference pattern corresponds to the Fabry-Perot cavity produced by the reflections between the SPPC centre, which is the origin of the SPP eigenmodes, and the SPPC boundary (effective cavity length of $26 \mu\text{m} \pm 13 \mu\text{m}$). The finesse of this cavity depends on the curvature of the boundary-it is more prominent for the case of the square boundary structure rather than the case of the circular

boundary structure- and its free spectral range¹² (FSR) can be controlled by the structure size.

It can also be seen that the maximum coupling efficiency to the eigenmode is experienced directly next to the bandgap and that at the vicinity of the bandgap the eigenmode splits into two parts, an effect referred in the bibliography as SPP forking [2, 89, 112] This can also be seen from Fig. 5. 2. 3 showing the far-field intensity SPP distributions around the circular boundary SPPC, when the illuminating light is vertically polarised and has a wavelength of (a)-(b) $\lambda=1280$ nm and $\lambda=1340$ nm , far away from the SPP bandgap formed from the crossing of the (0,1) and (0,-1) eigenmodes excited at the air-Au interface, and (c) $\lambda=1313$ nm at the bandgap vicinity, experimentally demonstrating the SPP forking effect and (d) $\lambda=1323$ nm , exactly next to the bandgap experimentally demonstrating the maximum coupling efficiency.

As referred in chapter 4, since the two prongs in which the (0, \pm 1) eigenmodes split, refract independently when they encounter the SPPC boundary, their angles of incidence/refraction depends on the boundary curvature at the points that each of them impinge the boundary. Thus, the angular separation between the two prongs can be controlled by the SPPC boundary [2]. In our experiment, as it can be seen in Fig. 5. 2. 4 (a) comparing the SPP angular distribution for the square and circular structures at the SPP forking wavelengths, the angular separation between the two parts of the SPP fork for the circular boundary (8.4°) is twice as much as this of the square one (4.2°).

¹² The wavelength separation between two adjacent transmission peaks

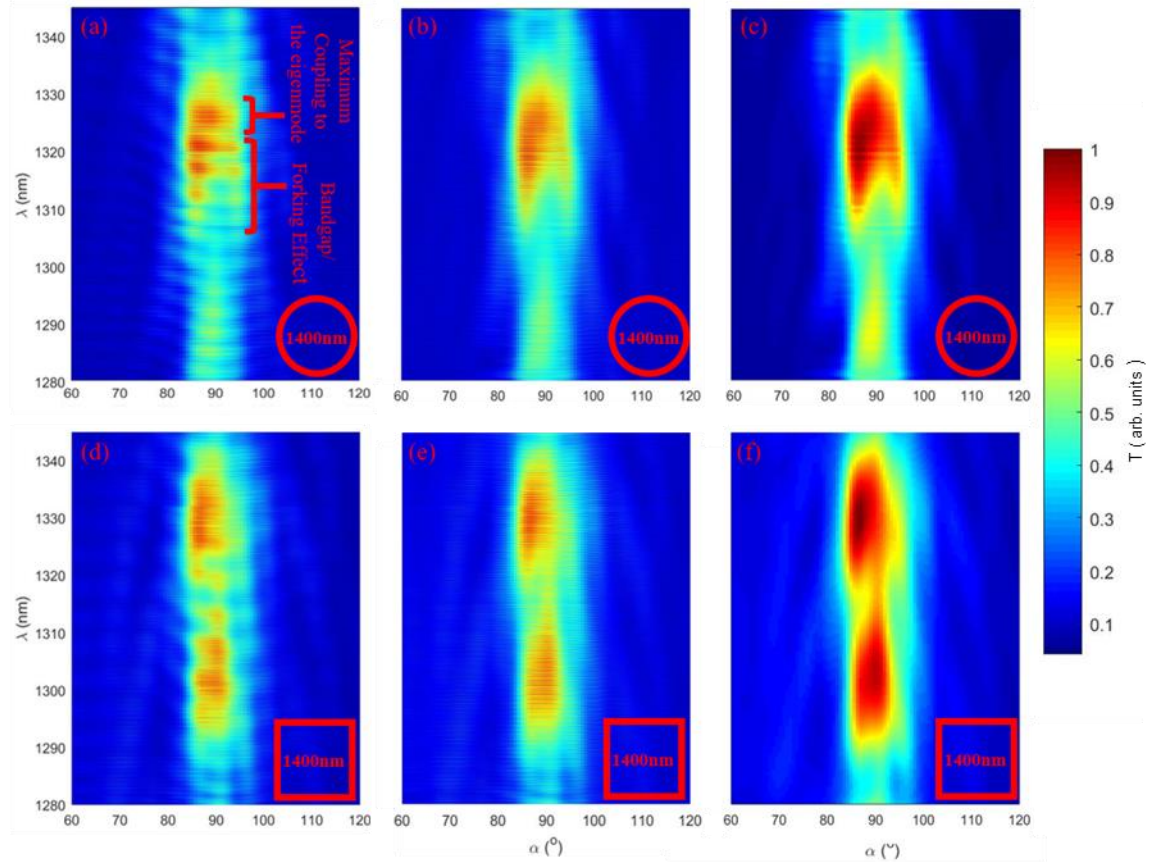


Fig. 5. 2. 2: Normalised angular distribution of the SPP signal transmittance as a function of the illuminating wavelength around 1400 nm period square lattice SPPCs with circular and boundary (a,d): as measured when illuminated with a non-AR coated patchcord, (b,e) when fibre-sample cavity is mathematically filtered out, (c,f) when both fibre-sample and substrate cavities are mathematically filtered out. The inset at each figure shows the boundary shape of the crystal.

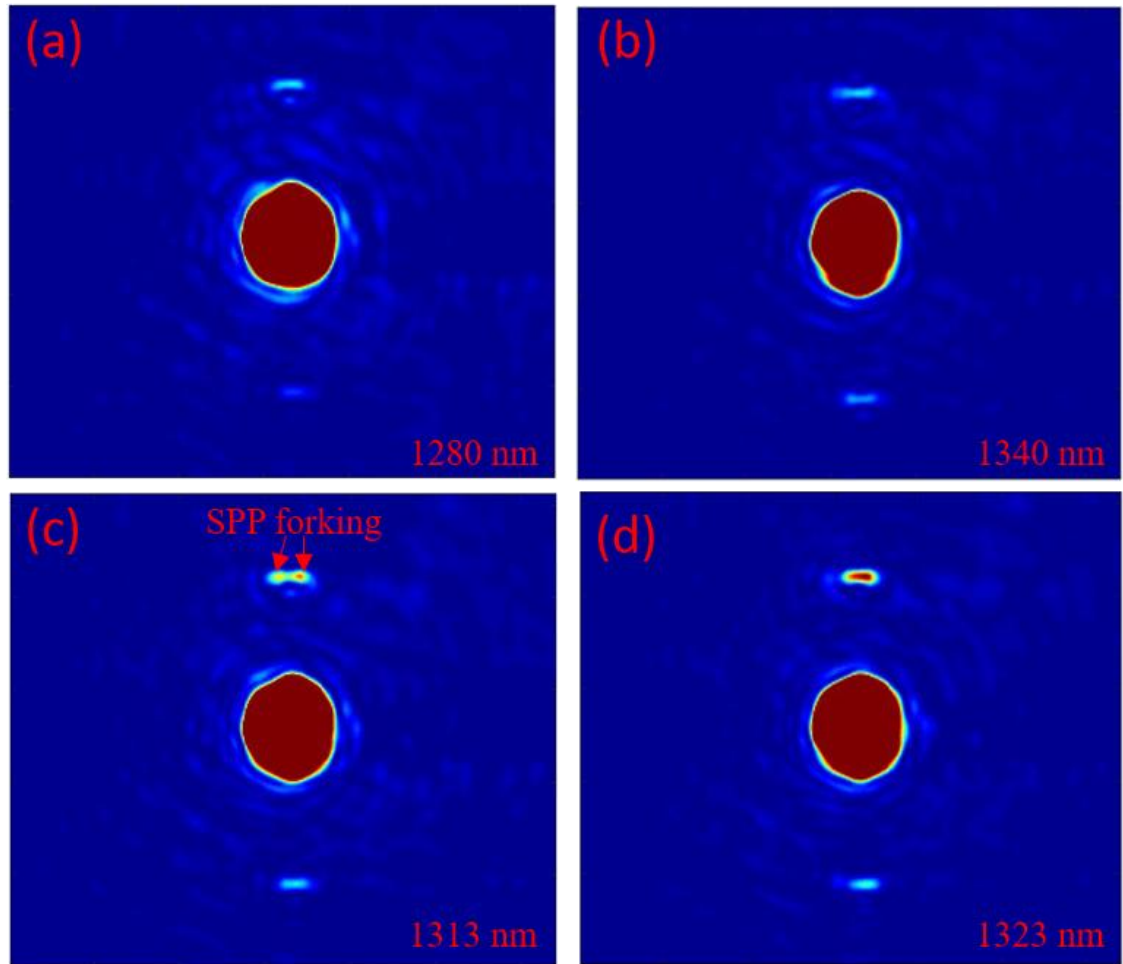


Fig. 5. 2. 3: Far-field intensity distributions measured for the circular boundary SPPC with 1400nm period square lattice when illuminated with (a) 1280 nm (b)1340 nm, (c) 1313 nm (d) 1323 nm vertically polarised light

The power ratio of the two prongs depend on the losses that they experience before detected and the number of scatterers that contribute to their excitation [2, 4]. As in our case the structures are symmetrical if the centre of the illuminating beam coincided with the centre of the crystal the two prongs will have the same intensity [2]. However, as it is

schematically shown in Fig. 5. 2. 4 (b), if a horizontal misalignment between the SPPC centre and the illuminating beam centre is introduced this symmetry breaks making the one prong to travel a slightly shorter length before meeting the scattering ring and converting into photons, resulting in a small difference between the SPP intensity coupling at the prongs; this difference is independent of the SPPC boundary. Furthermore, the number of scatterers contributing in the excitation/light-surface plasmon coupling for the one prong is smaller than this contributing to the other; a factor that outweighs any difference at the losses experienced by the two prongs (the two prongs travel equal distances in the high-loss surrounding smooth metal film but different distances in the low-loss nanostructured area) and leads to the smaller intensity of that prong. As it can be observed from Fig. 5. 2. 4 (a), the difference between the two parts of the SPP fork in circular structure is 18% , giving a power beam splitting ratio of about 5:4, while in the square structure is only 0.8% , giving a power beam splitting ratio of about 1:1 and indicating that the square structure is almost insensitive to misalignment (providing a power difference of less than 1%) [4].

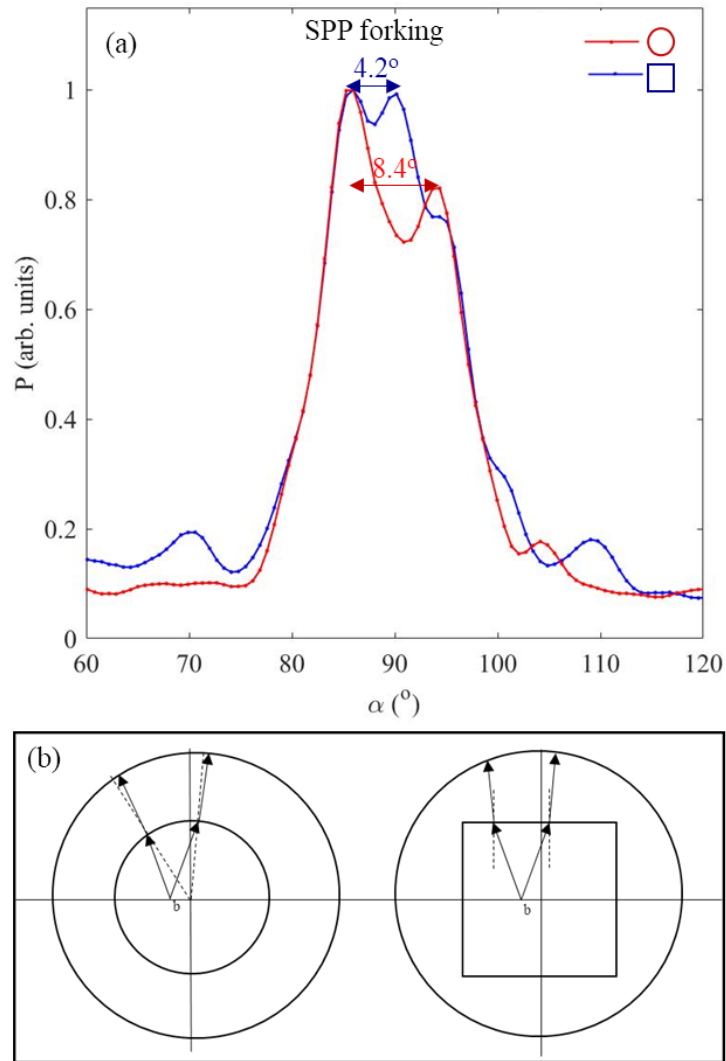


Fig. 5. 2. 4: (a) SPP signal angular distribution around SPPCs with a 1400 nm period square lattice, and square or circular boundary shape, illuminated at the vicinity of the bandgap spectral area formed by the cross-section of the $(0, \pm 1)$ eigenmodes (1319 nm and 1311 nm correspondingly) (b) Schematic sketch of the propagation of the two prongs of the SPP forks in the square and circular structures and the surrounding smooth film until they meet the surrounding scattering ring

The SPP forking effect can be used for power beam splitting applications. The square boundary structure would be suitable for applications requiring a robust/ not sensitive to alignment, 1x2 power beam splitter in which the two output channels will have the same power. On the other hand, the circular structure would be suitable for power beam splitters that require splitting ratios other than 1:1. The power ratio of the splitter would be able to be defined by the position of the illumination fibre/waveguide, or actively controlled through micro-positioning using piezoelectric systems[4]. On a reverse point of view the circular boundary structure, integrated with microdetectors could be used as micro-scale alignment sensor offering a position resolution of the order of a couple of microns [4].

From Fig. 5. 2. 2, it can also be seen that as expected from the SPPC transmission dispersion spectrum, one of the SPP prongs offers positive wavelength dispersion (the larger wavelength is detected in a greater angle) while the other offers negative wavelength dispersion (the larger wavelength is detected in a smaller angle); the positive/negative wavelength dispersion results in positive/negative SPPC refraction indices and thus in positive/negative refraction when the SPP waves launch on the smooth film as demonstrated in Fig. 5. 2. 4 (b).

The SPPCs were evaluated as potential miniaturised wavelength demultiplexers by taking cross-sections of the Fig. 5. 2. 2 to plot the power detected at selected angular positions α as a function of the illuminating wavelength¹³. Firstly, the wavelength dispersion properties were evaluated based on what is purely offered by the SPPC properties, i.e. after Fig. 5. 2. 2 (c, f), and then when the substrate cavity effect is not mathematically filtered out, i.e. by taking cross-sections in Fig. 5. 2. 2 (b,e). Fig. 5. 2. 5

¹³ The power at a given angular position α was calculated by integrating the intensity over two adjacent angular positions

shows the power detected at several angular positions α around the square and circular structure, after mathematically filtering out both the fibre-sample and the substrate cavities. The angular positions were carefully selected to allow the investigation of the wavelength angular beam separation for the spectral areas (a, b) away the bandgap and (c)-(f) at the SPP forking spectral area located at the vicinity of the bandgap. The fact that one part of the SPP fork offers positive wavelength dispersion and the other part offers negative wavelength dispersion is demonstrated in Fig. 5. 2. 5(c) and (f) . It can be observed that the SPPCs offers a wavelength angular beam separation of 1° - $1.62^{\circ}/\text{nm}$ but with extremely high crosstalk (-0.16dB - -0.04dB) compared to conventional integrated demultiplexers.

Fig. 5. 2. 6 (a-b) shows the power detected at several angular positions around the circular and the square structure before mathematically filtering out the substrate cavity. Although the wavelength angular beam separation is substantially increased (up to $36^{\circ}/\text{nm}$), and the crosstalk decreased (-0.45dB - -0.21dB) , the crosstalk offered by the set-up is still too high compared to conventional integrated demultiplexers.

If the set-up was to be used for dense wavelength demultiplexing it would need to be combined with high sensitivity detectors with a minimal detectable power difference less than 0.40 dB for the square structure and less than 0.20 dB , for the circular boundary structure. The assembly of the plasmonic crystal with high-sensitivity detectors can also be used as a planar microscale high-sensitivity wavemeter.

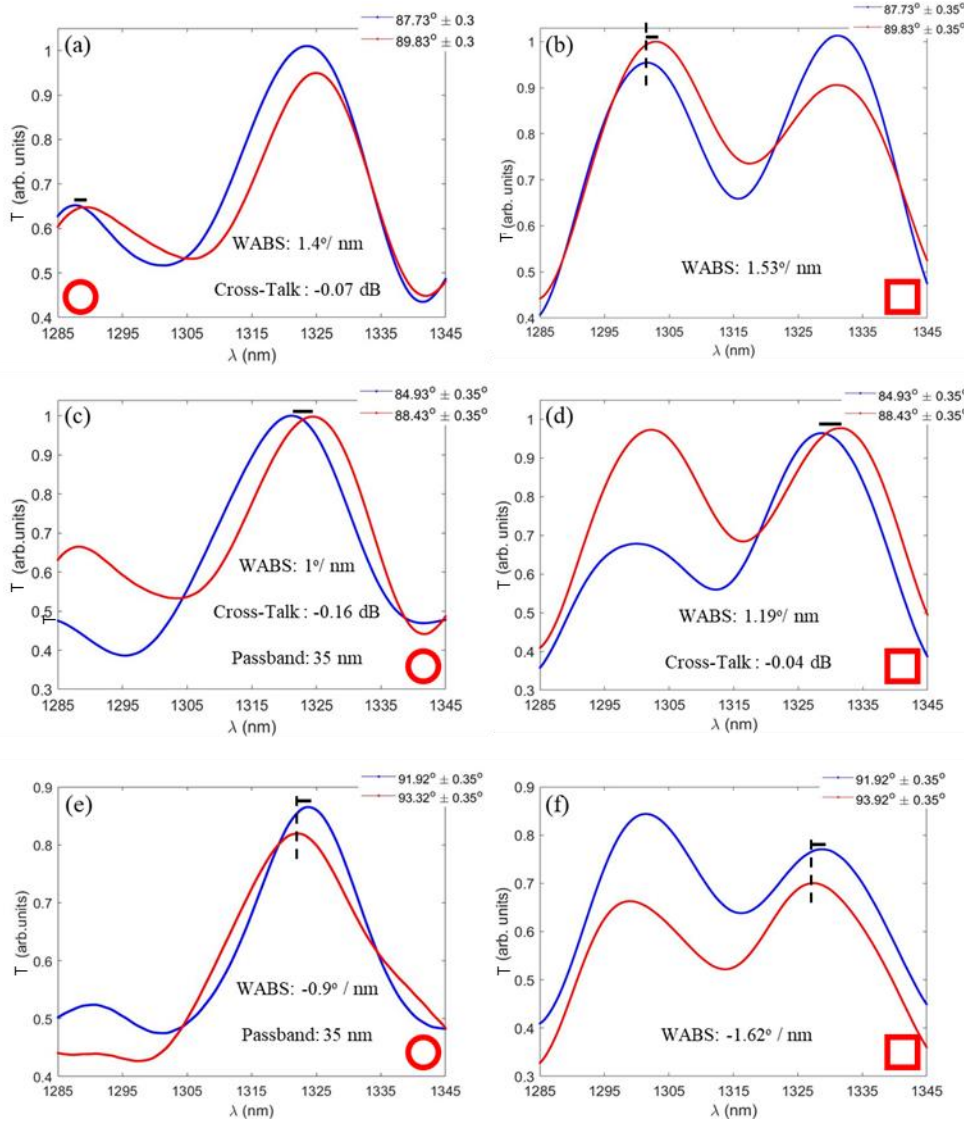


Fig. 5. 2. 5: SPP signal transmission spectrum at several angular positions around the 1400nm period square lattice, circular and square boundary SPPC, after mathematically filtering out the fibre-sample and the substrate cavity for the spectral area (a)-(b) away from the bandgap formed by the (-1,0)- (0,1) eigenmode crossing at the Au-air interface, (c)-(f) at the SPP forking spectral area , located at the vicinity of the bandgap, at angular positions representing the two parts of the SPP fork ; The SPPC boundary shape is shown at the inset.

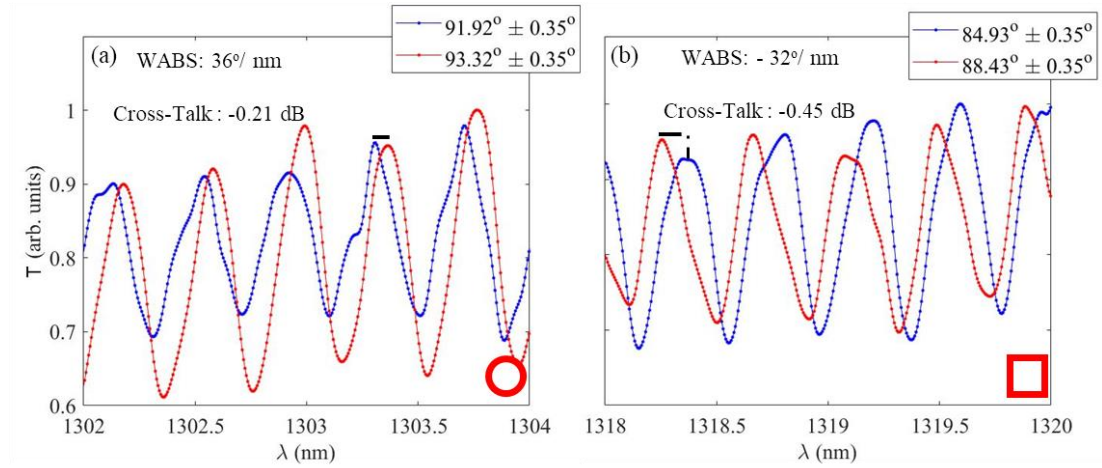


Fig. 5. 2. 6: SPP signal transmission spectrum at the SPP forking spectral area at angular positions representing the two parts of the SPP fork around the 1400nm period square lattice, as measured after removing the noise and patchcord-sample cavity. The substrate cavity has not been filtered and the SPPC boundary shape is shown at the inset.

Tables 5. 2. 1 (a) and (b) show the transmittance of the SPPCs (circular and square) for several wavelengths at the corresponding angular positions. Indeed, the square structure can be used two wavelengths to distinguish between two wavelengths with a 0.1 nm wavelength difference, if integrated with detectors whose the minimum detectable power difference would be less than -0.45 dB, while the circular structure can distinguish two wavelengths with a 0.06 nm resolution if integrated with detectors that the minimal detectable power difference would be smaller than -0.21 dB. Microscale wavemeters, with such a sensitivity could be used in detecting very small refractive index differences with applications in diagnostic medicine/ wearable detectors, optimising/calibrating the exact

refractive index of new material assemblies or detect small impurities in the device fabrication process which could be critical for micro/nano components of future technologies like optical/quantum computing.

| λ (nm) | T (a. u.) at $91.92^\circ \pm 0.35^\circ$ | T (a. u.) at $93.92^\circ \pm 0.35^\circ$ |
|---------------------|--|--|
| 1303.309 | 0.954 | 0.910 |
| 1318.364 | 0.894 | 0.952 |

| λ (nm) | T (a. u.) at $84.93^\circ \pm 0.35^\circ$ | T (a. u.) at $88.43^\circ \pm 0.35^\circ$ |
|---------------------|--|--|
| 1318.255 | 0.838 | 0.953 |
| 1318.364 | 0.926 | 0.835 |

Table 5.2.1: SPPC transmittance values T at given wavelength values λ and corresponding angular directions around the (a) circular and (b) square boundary SPPCs

One possible reason for the high crosstalk is the illumination of an extended spectral area, due to the numerical aperture of the illuminating fibre. The difficulty here was to produce a collimated beam with a spot radius $\omega_0 \approx 20 \mu\text{m}$, such as to illuminate the SPPC but not the scattering ring. At the wavelength range examined the flat area of the $(\pm 1, 0)$ eigenmodes cover only 2° , so the maximum range of illumination angles to be covered should have been close to 0.2° . Alternatively at the wavelength range 1450 nm- 1500 nm the flat spectral area of the $(\pm 1, 1)$ eigenmodes at the Au-glass interface, which can be imaged at the scattering ring as well, is extended over 7° and it could potentially be characterised with an illumination system with a maximum of 0.7° range of illumination angles. A possible solution to this is the illumination of the sample through a waveguide/ photonic crystal fibre which would illuminate a much smaller range of angles or the use

of grin (gradient index) lens which is able to produce a small radius collimated beam if positioned at the end of a fibre. Indeed, near-infrared antireflective coated grin lenses able to produce a 120 μm diameter collimated lens when connected to a singlemode fibre patchcord are available commercially. In this scenario, we would need to have a scattering with a bigger internal radius (more than 100 μm), so it is not illuminated by the incident beam. Having a scattering ring with an internal radius of 346 μm positioned around the circular crystal or of 450 μm positioned around the square crystal, would be in advantage of the wavelength characterisation as according to Fig. 4. 3. 1. 2, these are the eigenmode focal distance for the two structures. If needed the focal distance can be reduced by reducing the SPPC size or manipulating its boundary curvature (as seen in Fig. 4. 3. 1.2). Furthermore it would be interesting to examine if differently shaped lattices produce eigenmodes with a more extended flat area and could form part of future work.

5.3 Broadband Wavelength Demultiplexing Based on Multiple Interfaces Eigenmode Excitation

In this section the wavelength dispersive properties of a circular boundary SPPC, with a 1530 nm period square were investigated. The sample was surrounded by a circular slit, scattering ring, of a 120 μm internal radius and a 1.5 μm width, similar to the samples described in the previous section. The far-field SPPC transmission dispersion of the sample was measured as described in section 3.2 and is shown in Fig. 5. 3. 1. The wavelength dispersive properties were characterised at the wavelength range 1499 nm - 1580 nm, following the procedure described in section 5.1. Fig. 5. 3. 1 shows the spectral

area which was illuminated during the characterisation, considering the range of illumination angles, 0° - 7° , and the scanned wavelength range.

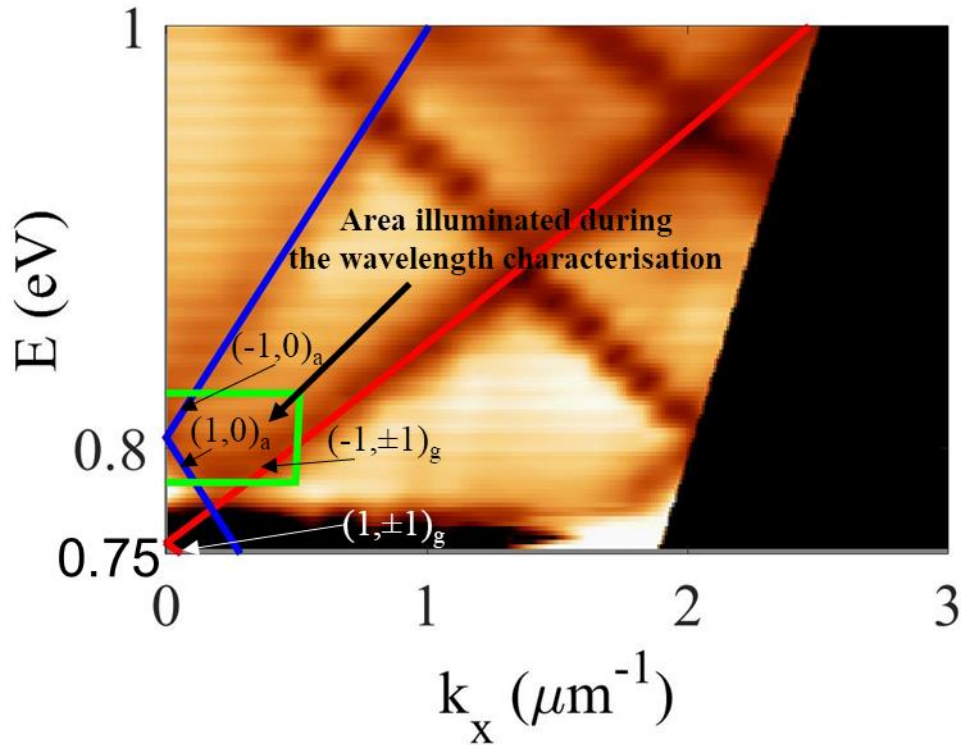


Fig. 5. 3. 1: Measured SPPC transmission dispersion (2D map) and (lines) eigenmode positions estimated from Eq. 3. 1. 1, notations “a” and “g” correspond to the modes of air-Au and glass-Au interfaces, respectively, the spectral area investigated during the wavelength characterisation is also shown

As it can be observed the excited eigenmodes were the $(-1, \pm 1)$ at the gold-glass interface and the $(\pm 1, 0)$ at the gold-air interface. Fig. 5. 3. 2 shows the far-field SPP intensity distribution on and around the SPPC when illuminated with horizontally polarised light with (a) a 1516 nm wavelength (b) a 1552 nm wavelength. In order to investigate the wavelength dependent angular SPP distribution around the SPPC the captured images were processed in the same way as in the case of the 1400nm period

SPPC, described in section 6.2. However, in this case the SPPC centre was identified by the crossing point of the $(-1, \pm 1)$ eigenmodes as shown in Fig. 5. 3. 2 (b). The SPP signal angular distribution around the SPPC centre for illuminating wavelengths $\lambda= 1516$ nm and $\lambda=1552$ nm and horizontal polarisation is in Fig. 5. 3. 2 (c). As expected from the transmission spectrum the $(\pm 1,0)$ eigenmodes at the gold-air interface and the $(-1,-1)$, $(-1,+1)$ eigenmodes at the gold-glass interface are excited and can be observed around the principal angles $\alpha=-1^\circ (+180^\circ)$, $\alpha=44^\circ (+180^\circ)$ and $\alpha=133^\circ (+180^\circ)$ The excitation of the $(\pm 1,0)$ eigenmodes at the gold-air interface is favored if the illumination wavelength is $\lambda= 1516$ nm , while the excitation of the $(-1, \pm 1)$ at the gold-glass interface is favored if the illumination wavelength is $\lambda= 1552$ nm.

The wavelength dependent SPP signal angular distribution around the 1530nm square lattice, circular boundary SPPC is shown in Fig. 5. 3. 3 (a) as measured, using an AR-coated patchcord, and (a) after mathematically filtering out the substrate cavity.

To investigate the wavelength spatial separation due to the coupling to the several eigenmodes, after mathematically filtering out the substrate cavity, the intensity around the principal angles $\alpha=-1^\circ$ and $\alpha=44^\circ$ in Fig. 5. 3. 3 (b) has been integrated and plotted as a function of the illuminating wavelength in Fig. 5. 3. 5 (a). It can be observed that by illuminating the SPPC with horizontally polarised light, a wavelength angular beam separation (WABS) of $1.51^\circ/\text{nm}$, with -1.03 dB crosstalk can be achieved due to the wavelength dependent coupling in the $(\pm 1,0)$ at the Au-air interface and the $(-1,1)$ Au-glass interface.

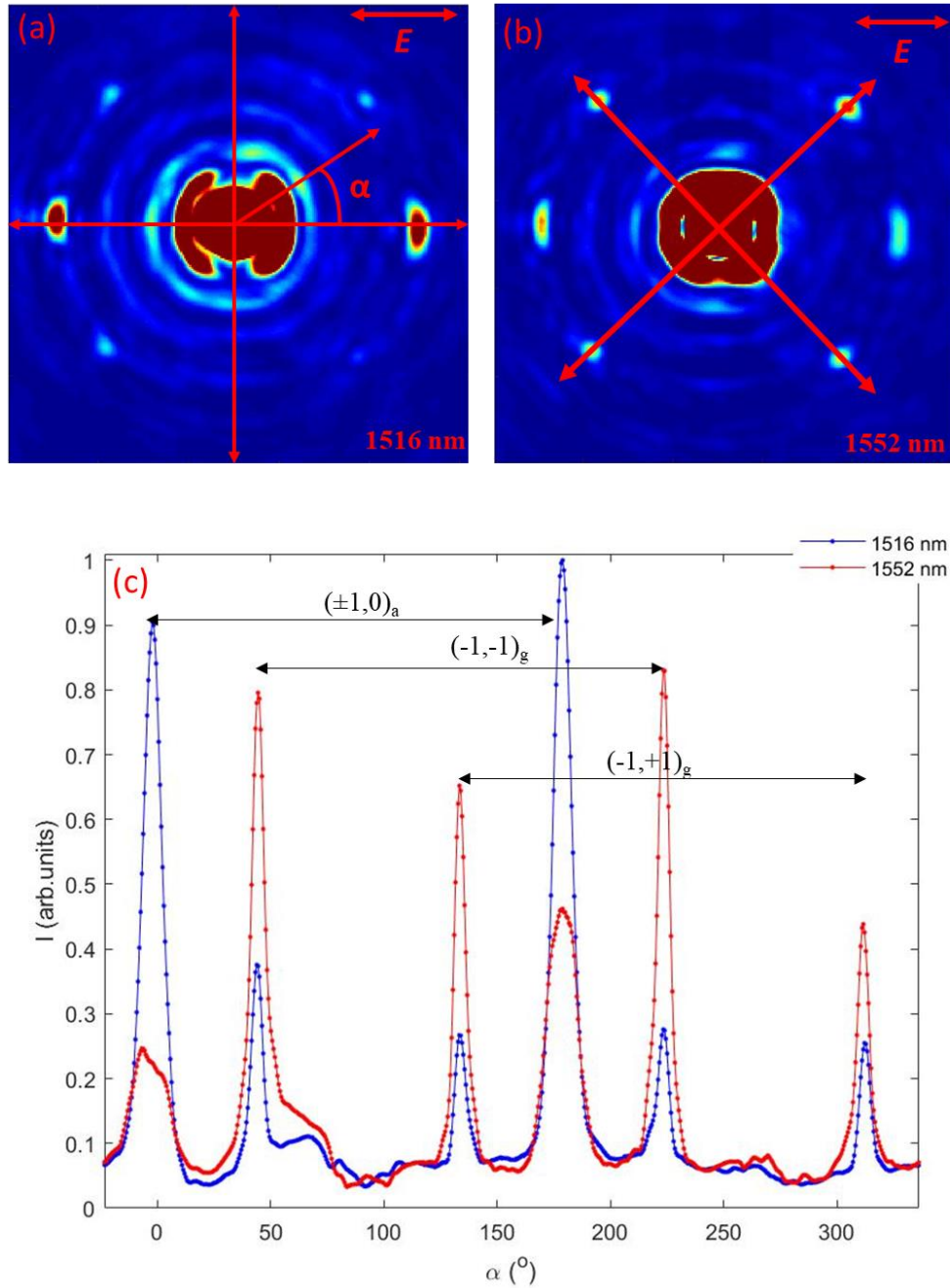


Fig. 5.3.2: (a-b) Far-field intensity distribution on and around the 1530nm square lattice SPPC, with circular boundary, when illuminated with horizontal polarisation and a wavelength of 1516nm and 1552nm (c) SPP transmittance angular distribution around the SPPC when illuminated with horizontally polarised light with a wavelength of 1516nm and 1552nm

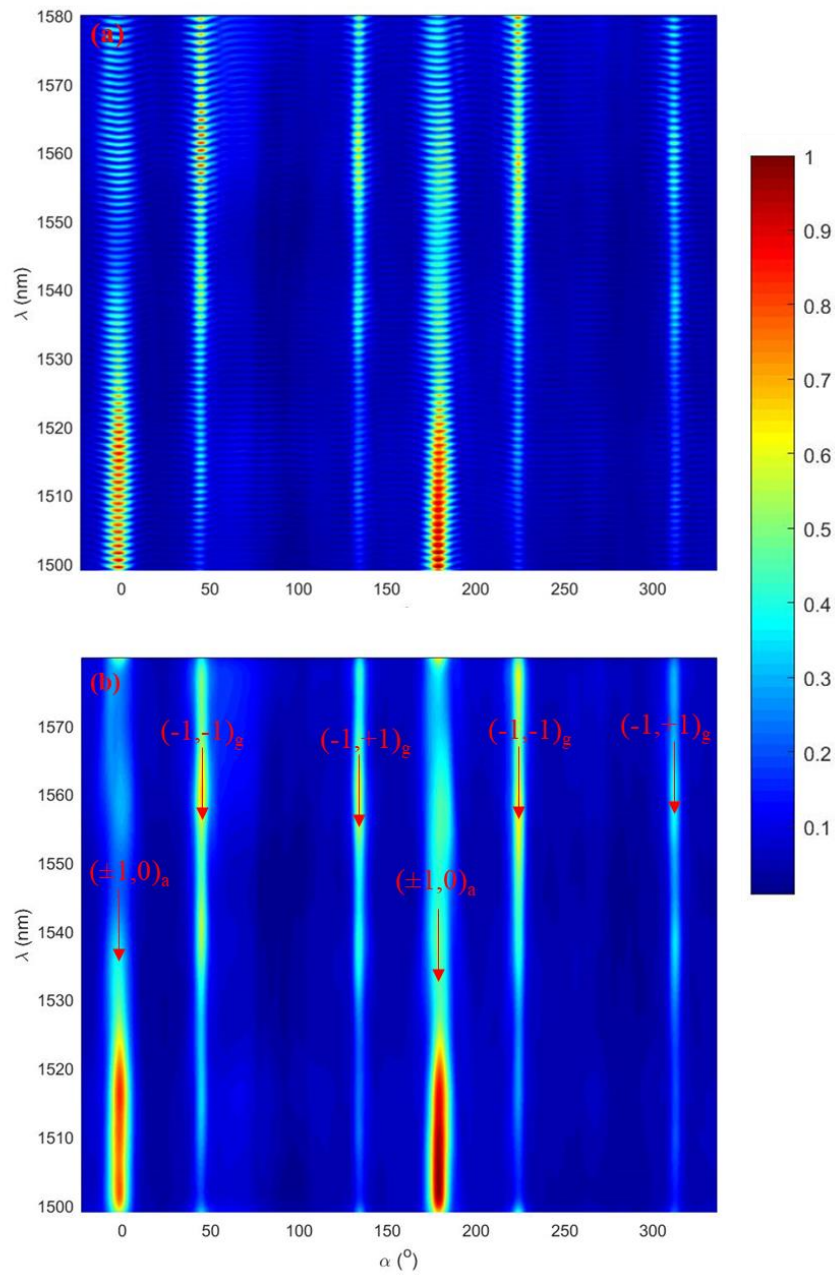


Fig. 5. 3. 3: Wavelength dependent SPP normalised transmittance angular distribution around the circular SPPC with a 1530nm period square lattice, when illuminated with horizontally polarised light (a) as measured using an antireflection-coated patchcord (b) after mathematically filtering out the substrate cavity

Due to the TM nature of the SPPs, the coupling to the eigenmodes is both wavelength and polarisation dependent, favoring the excitation of the eigenmode which is aligned with the electric field vector. In the case of the horizontal polarisation the eigenmodes in favor are the $(\pm 1, 0)_a$, while if the polarisation is linear with azimuth angle 45° , the eigenmode in favor is the $(-1, -1)_g$. The experiment was repeated with the polarisation of the illuminating light to be linear with azimuth angle 45° . Fig. 5. 3. 4 shows the wavelength dependent SPP normalised transmittance angular distribution around the SPPC when illuminated with linear polarised angle with 45° azimuth angle at the wavelength range 1499 nm- 1581 nm, using an AR-coated patchcord (a) as measured and (b) after mathematically filtering out the substrate cavity. Similar to the case of the horizontal polarisation, to investigate the wavelength spatial separation due to the coupling to the several eigenmodes, after filtering out the substrate cavity, the SPP intensity around the principal angles $\alpha = -1^\circ$ and $\alpha = 44^\circ$, from Fig. 5. 3. 4 (b), were integrated and plotted as a function of the illuminating wavelength in Fig. 5. 3. 5 (b). It can be observed that when the SPPC is illuminated with light linearly polarised with 45° azimuth angle, it can offer a wavelength angular beam separation of $2.14^\circ/\text{nm}$, with -0.59 dB cross-talk, due to the coupling at the $(\pm 1, 0)_a$ and $(-1, -1)_g$ eigenmodes.

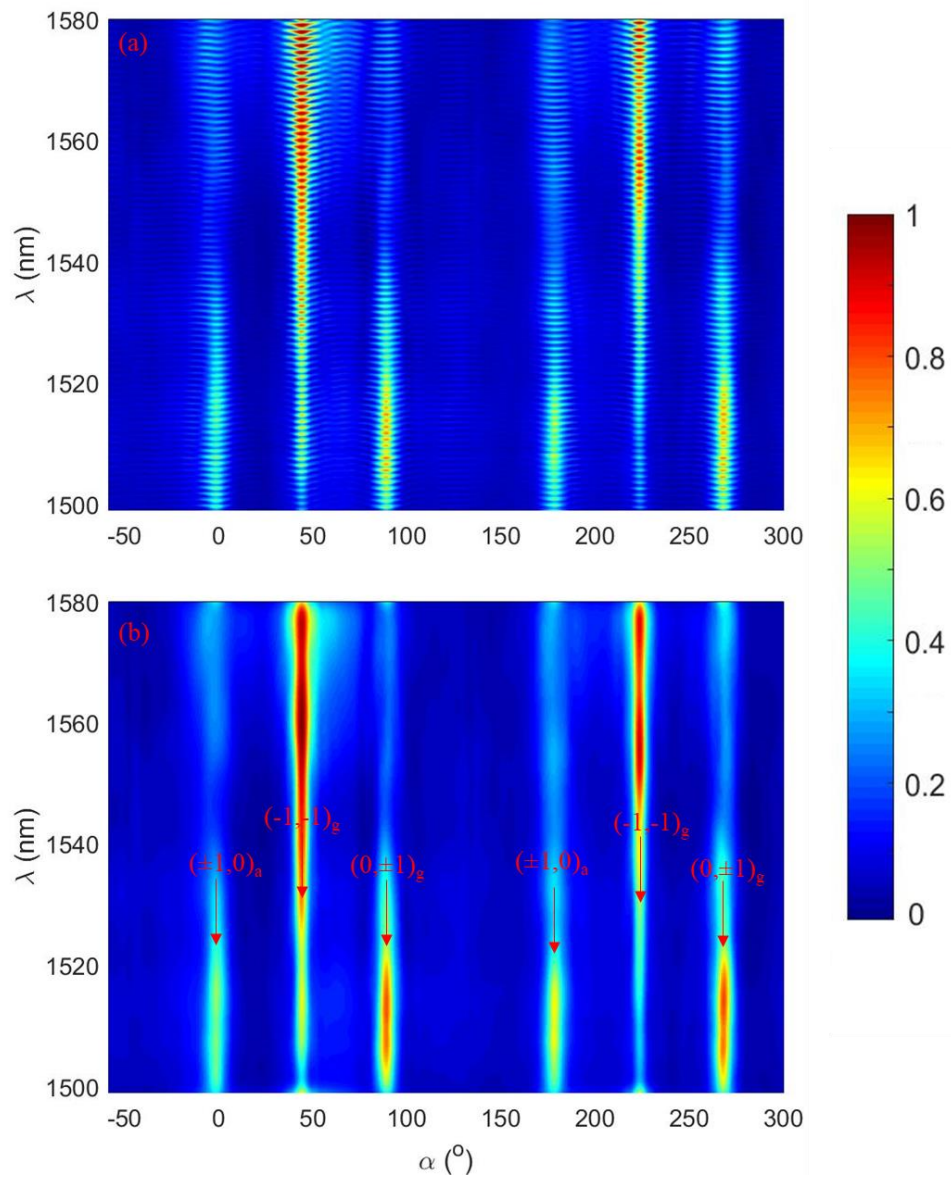


Fig. 5. 3. 4: Wavelength dependent SPP normalised transmittance angular distribution around the circular SPPC with a 1530nm period square lattice, when illuminated with linearly polarised light with a 45° azimuth angle (a) as measured using an antireflection-coated patchcord (b) after mathematically filtering out the substrate cavity

The coupling to the eigenmodes is both wavelength and polarisation dependent; due to the TM nature of the SPPs is parallel to the SPP wave direction, the excitation of the eigenmode which is aligned with the electric field of the illumination beam is in favor. In particular when the polarisation is linear with azimuth angle 0° the coupling to the $(\pm 1, 0)_a$ is favored while if the azimuth angle is 45° the coupling to the $(-1, -1)_g$ is favored. Fig. 5. 3. 5 (a) shows the SPP power detected around the principals angles $\alpha = -1^\circ$ and $\alpha = 44^\circ$ when the crystal is illuminated with horizontal polarisation, it can be observed that the coupling to the two different eigenmodes, $(\pm 1, 0)_a$ and $(-1, -1)_g$ respectively offers $1.51^\circ/\text{nm}$ wavelength angular beam separation (WABS), while the cross-talk is -1.03 dB. Similarly, for the case that the crystal is illuminated with 45° linear polarisation the detected powers around the principals angles $\alpha = -1^\circ$ and $\alpha = 44^\circ$ offer $2.14^\circ/\text{nm}$ wavelength angular beam separation and -0.59 dB (Fig. 5. 3. 5 (b)). From Fig. 5. 3. 5 (a) and (b) it can be observed that signals at the wavelength range of 1500 nm- 1520 nm are preferentially coupling to the $(\pm 1, 0)_a$ eigenmodes and detected around $\alpha = -1^\circ$, while signals at the wavelength range of 1550 nm- 1570 nm are preferentially coupling to the $(-1, -1)_g$ eigenmode and detected around $\alpha = 44^\circ$. However, if both signals have the same polarisation the cross-talk is significant high. One way to decrease the cross-talk is the signal at the wavelength range 1500 nm- 1520 nm to be horizontally polarised and the signal at the wavelength range to be linearly polarised with 45° azimuth angle. In that case the signals can be spatially separated with a -3 dB cross-talk, as it can be observed from Fig. 5. 3. 5 (c) comparing the SPP signal detected around the angular position $\alpha = -1^\circ$ when the illuminating light is horizontally polarised, with the SPP signal detected around the angular position $\alpha = 44^\circ$ when the illuminating light is linearly polarised with a 45° azimuth angle.

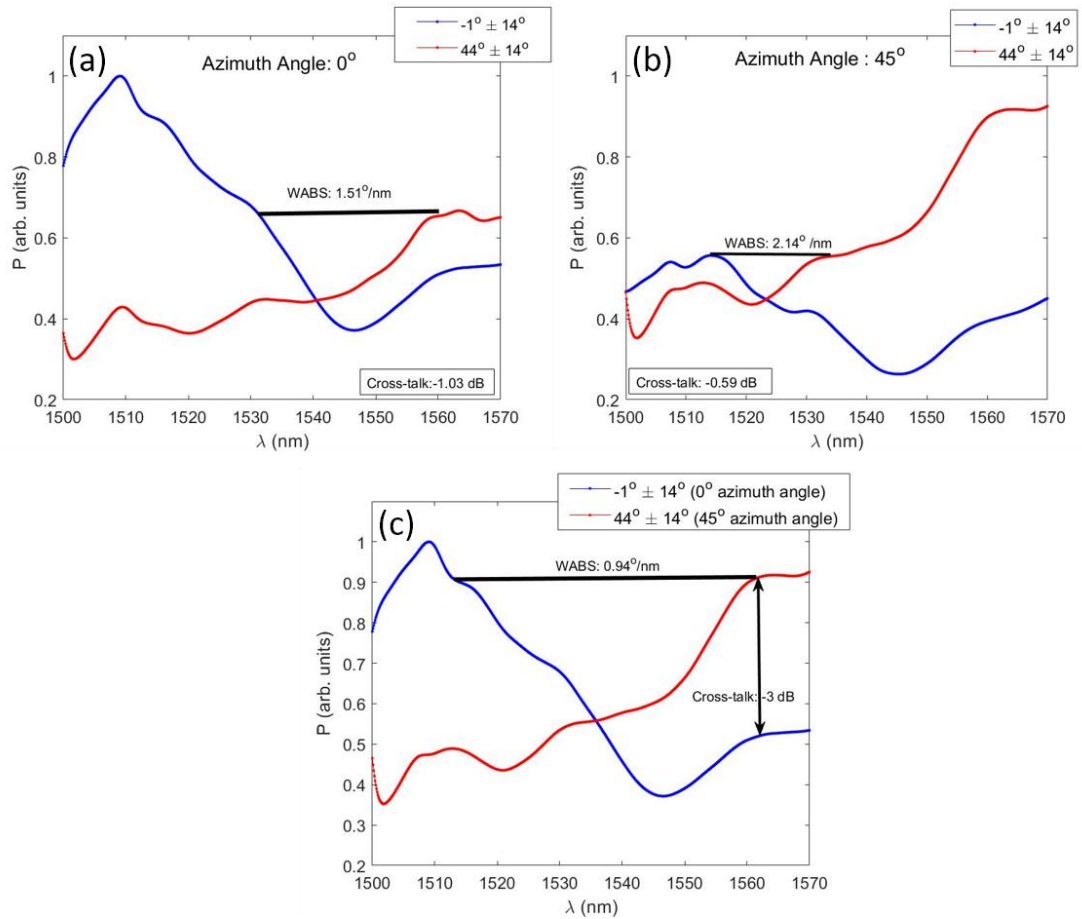


Fig. 5.3.5: SPP transmission spectrum at -1° and 44° corresponding to the $(0,1)_a$ and $(1,1)_g$ eigenmodes respectively when the sample is illuminated with linear polarisation of (a) azimuth angle 0° (b) azimuth angle of 45° and (c) azimuth angle that maximises each of the eigenmode, i.e 0° for the $(0,1)_a$ eigenmode, detected at the angular position -1° , and 45° for the $(1,1)_g$ eigenmode, detected at the angular position 44° .

In conclusion the SPPC behaves as a broadband wavelength demultiplexer, with a 55 nm channel spacing, separating 1509 nm and 1564 nm with a -3 dB crosstalk if the two channels are linear polarised with azimuth angles 0° and 45° respectively. The broadband wavelength demultiplexer offers an above 20 nm wide, -1.55 dB passband-the wavelength range over which the value of the signal is at least 75% of its maximum value. The device is based on the simultaneous coupling of the incident light into SPP eigenmodes of two different metal dielectric interfaces, namely air-Au and glass-Au. The SPPC provides both the coupling of photons to SPPs and the wavelength demultiplexing, the SPP waves propagate on the different metal-dielectric interfaces until when they reach the scattering ring, couple back into light and start propagating again together.

The range of available eigenmodes can be manipulated by increasing the number of interfaces passively by choosing the appropriate metal / dielectric (composite) material with the desired refractive index or actively control the dielectric refractive index, e.g. by using liquid crystals and applying electric field [69] or by controlling the metal free-carrier concentration by applying lower-power pump pulses [119]. In addition, the available eigenmodes can be increased by aligning several SPPCs on top of each other or be choosing to illuminate spectral areas/ design SPPCs with a higher density of eigenmodes.

5.4 Summary

In this chapter we have experimentally demonstrated a microscale $1 \times 2 / 1 \times 4$ (2 at each facet) power beam splitter based on a SPPC. The beam splitting is due to the SPP coupling to the $(0, \pm 1)$ eigenmodes, at the air-Au interface, close to their cross-point. As seen in the previous chapters, when two eigenmodes cross, a bandgap is formed causing

the SPP eigenmodes to flatten and the SPP group velocity $\left(\frac{d\omega}{dk}\right)$ to become zero. A group velocity equal to zero means that the SPP wave does not propagate in that direction, and thus the SPP beam splits. The splitting ratio and the angular separation of the 2/4 prongs can be controlled by the SPPC boundary and the alignment between the SPPC centre and the centre of illumination. Some boundary shapes such as square, are more robust to misalignment between the SPPC centre and illumination beam centre and are offering 1:1 power ratio between the prongs. Other boundary shapes, such as circular are more sensitive to SPPC-illumination beam misalignment, opening the route of controlling the power ratio between the prongs through passive careful design or active control of the SPPC- illumination beam alignment. Such sensitive to misalignment beam splitters can be used as microscale detectors able to detect misalignment in the order of nanometers.

The wavelength dispersion of the $(0, \pm 1)$ eigenmodes, at the air-Au interface, were also characterised following the initial assumption that at the vicinity of the eigenmode flat areas, where $\left(\frac{d\omega}{dk}\right)$ is very small, a small change in wavelength would result in a big change in the SPP propagation direction, making SPPCs suitable for dense wavelength demultiplexing applications. Since it was shown that the Fabry-Perot cavity formed between the facets of the glass substrate affects the SPPC wavelength dispersion properties, these were characterised as experimentally measured and after mathematically filtering out the substrate cavity. In this way the eigenmode wavelength dispersion was isolated from the substrate Fabry-Perot cavity influence. The wavelength angular beam separation (WABS) offered from the positive and negative wavelength dispersion, experienced from the $(-1,0)$ and $(+1,0)$ eigenmodes, respectively, at the air-Au interface was $1^\circ-1.62^\circ/\text{nm}$ which would be a very desirable feature for microscale dense wavelength

demultiplexers. However, the extremely high crosstalk levels (greater than -0.16 dB) were prohibitive for their practical implementation as dense wavelength demultiplexers. The 700 nm glass substrate Fabry-Perot cavity, enhanced the WABS to $32^\circ/\text{nm}$ - $36^\circ/\text{nm}$ and decreased the crosstalk; nevertheless, the crosstalk levels (-0.45 dB - - 0.21dB) remained too high compared to conventional wavelength demultiplexers.

If the set-up were to be used for dense wavelength demultiplexing, they would need to be combined with high sensitivity detectors with a minimal detectable power difference less than 0.20 dB, for the circular boundary structure, and less than 0.40 dB, for the square structure and a high cut-off power threshold (about -0.45 dB less than the maximum value). Alternatively, devices that do not transmit power less than the above-mentioned cut-off power threshold could be used. The assembly of the SPPCs with the high-sensitivity detectors can perform as microscale wavemeters, able to distinguish signals with a 0.06 nm (circular) or 0.1 nm (square) wavelength difference. Such wavemeters can be used for the detection of small refractive index differences, with potential applications in diagnostic medicine and high-precision nanofabrication.

Some possible reasons for the high crosstalk are the illumination of an extended spectral area, due to the numerical aperture of the illuminating fibre, and the placement of the scattering ring very close to the SPPC, where the eigenmode spreads over an extended range of angles. The use of an alternative illumination set-up such as a grin lens, which would provide a collimated illumination of a diameter around 120 μm , and the placement of the scattering closer to the focusing point of the eigenmodes, located around 346 μm away from the circular structure centre, or 450 μm away from the square structure centre, could result in the elimination of the crosstalk.

In addition, in section 5.3, a broadband wavelength demultiplexer with a 55 nm channel spacing and a -1.55dB-passband at least 20 nm wide has been experimentally demonstrated. The device was based on the coupling of light to an SPPC eigenmodes excited on both its metal dielectric interface, namely Au-air and Au-glass and detecting simultaneously by positioning a scattering ring around the SPPC. Combining wavelength and polarisation modulation channels with central wavelengths 1509 nm and 1564 nm were able to spatially separate with a -3 dB crosstalk, if the channels were linearly polarised at azimuth angles 0° and 45° respectively. The SPPC polarisation dispersive properties will be extensively in the next chapter.

6. Multiple-Level Polarisation Demultiplexing based on SPPCs

Polarisation characterises the vectorial nature of electromagnetic (EM) radiation, which represents a fundamental property separate from its frequency and intensity. In optical communications and signal processing, the polarisation of a carrier wave is an additional degree of freedom that can be used for information management. For example, multiplexing signal in two orthogonal polarisation states doubles the bandwidth of the system [142, 143]. Alternatively, one can use polarisation shift-keying for encoding digital signal in different polarisation states of a carrier wave [144].

Furthermore, there are many scientific fields including astronomy, chemistry, sensing, air pollution monitoring, structure stress imaging and quantum information technology, in which determining the state of polarisation is of paramount importance [145-148]. The measurement of the polarisation reveals rich information about the structure and composition of materials, the handedness of chiral molecules, and generally the nature of scattering, emission and absorption phenomena [149, 150]. Polarisation can be used to ascertain the texture and orientation of surfaces in remote sensing applications, help defeat fog, camouflage and image clutter [145] and is an important control parameter in engineering light-matter interactions, including in waveguiding [145] and is an important control parameter in engineering light-matter interactions, including in waveguiding [145] and is an important control parameter in engineering light-matter interactions, including

in waveguiding [151-156], nanofabrication [157, 158], nanofabrication [157, 158] and biomedicine [159]. and biomedicine [159]. and biomedicine [159].. Polarisation can be used to ascertain the texture and orientation of surfaces in remote sensing applications, help defeat fog, camouflage and image clutter [145] and is an important control parameter in engineering light-matter interactions, including in waveguiding [151-156], nanofabrication [157, 158] and biomedicine [159].. Polarisation can be used to ascertain the texture and orientation of surfaces in remote sensing applications, help defeat fog, camouflage and image clutter [145] and is an important control parameter in engineering light-matter interactions, including in waveguiding [151-156], nanofabrication [157, 158] and biomedicine [159].

Despite this vast technological potential, polarisation is seldom measured, compared to, for example, intensity or frequency. Measuring the state of polarisation is an inherently tricky problem. The major reason is that both the amplitude and phase information of orthogonal state of polarisations should be specified at the same time. This is addressed in the state-of-the-art polarimeters by dividing the signal up either in space or in time [145, 160]. Because a set of polarisers, waveplates, beam-splitters and detectors are used to build a polarimetric system, the system becomes bulky and complex, which hinders the future development for mobile, compact, integrated and miniature optical devices for many applications such as monitoring the polarisation in fibre links, integrated nanophotonic platforms and in vivo polarisation sensing. In this context, plasmonics provide an unprecedented opportunity in the development of subwavelength waveguide circuitry and the miniaturisation of photonic components for light manipulation [1, 47, 56]. Since surface plasmon polaritons (SPPs), are intrinsically TM-polarised [56], they

are very attractive for polarisation management [47]. SPPs preserve their polarisation state during propagation and, in turn, their propagation direction can be controlled with the polarisation of the excitation light. Benefiting from the TM nature of SPPs, the polarisation division-multiplexing in plasmonic interconnects can be further simplified, compared to the long-haul optical interconnects at which advanced channel coding techniques are required due to the random variation of the polarisation state of light in fibers. The excitation of the SPP waves is a highly broadband effect ranging from ultraviolet to infrared [1].

In this chapter a four-level polarisation discriminator, able to uniquely resolve and spatially separate four linearly polarised photonic/plasmonic signals with azimuth angles $\theta = 0^\circ, 45^\circ, 90^\circ,$ and 135° , based on a two-dimensional surface plasmon polaritonic crystal (SPPC), has been experimentally demonstrated. The device can be used for four-level polarisation shift-keying or as polarimetric miniaturised device for measuring the s_1, s_2 Stokes parameters of photonic/plasmonic signals. It is nondestructive as it capitalises on the high-transmittance of the light through the nanostructure area and the weaker scattering in SPP waves that launch on the surrounding smooth film, as well as on the fact that the light tunneling through the nanostructure area maintains its polarisation, and can be used in line in systems that the signal needs to be monitored without being absorbed. It is also planar and microscale, circular with a $40 \mu\text{m}$ diameter, which makes it easy to combine with electronic devices or other plasmonic and planar dielectric components in integrated photonic chips. It is self-calibrated within the 1dB colorless bandwidth of 7 nm, while it can operate in a 40 nm wavelength range with calibration. Furthermore, the operating wavelength can be moved to any wavelength from ultraviolet to infrared by

changing the period of the structure. The concept has also been expanded to propose a novel miniaturised polarimeter, able to provide full polarimetric functionality and determine all the 3 Stokes parameter, s_1 , s_2 and s_3 , based on the combination of two SPPCs and a high-birefringence fibre length. Following the realisation of the four-level polarisation discriminator , [5, 52] and its proposed application as part of a microscale polarimeter [6], a number of compact microscale polarimeters have been realised based on the polarisation-dependent excitation of SPPs in nanoslits, bull's eyes apertures and chiral structures [7, 8, 14] or metasurfaces [9-13, 161, 162].

6.1 Experimental Procedure

The four-level polarisation discriminator, experimentally demonstrated in this chapter, was based on the SPPC crystal, circular boundary with a 1530 nm period square lattice characterised in section 5.3. As shown in Fig. 5. 3. 1 the SPPC has been designed such that the $(\pm 1,0)$ and $(0,\pm 1)$ SPP Bloch modes of the Au-air interface are spectrally situated close to the $(-1,\pm 1)$ modes of the Au-glass interface, in the center of the Brillouin zone. The $(0,\pm 1)$ eigenmode replaces the $(\pm 1,0)$ one under the orthogonally polarised illumination. When the SPPC is illuminated with a 7° divergent beam, corresponding spectral region is highlighted in Fig. 5. 3. 1 all the four Bloch modes can be excited at the same time. In order to investigate the simultaneous excitation of the four different eigenmodes and its effect on the polarisation dispersion properties of the SPPC, the experimental arrangement shown in Fig. 5. 1. 1 was used.

Fig. 6. 1. 1 shows the intensity distribution on and around the SPPC under the illumination with linearly polarised light at azimuth angles $\theta = 0^\circ, 45^\circ, 90^\circ,$ and 135° . The central area is the image of the SPPC itself and is saturated due to the high direct transmission through the crystal. The SPP waves observed at the spatially separated angles of $\alpha = 0^\circ, 45^\circ, 90^\circ,$ and 135° correspond to the SPP eigenmodes discussed above; SPP waves corresponding to the same eigenmodes are observed in the counterpart hemisphere. The observed SPP waves are launched by the crystal on the surrounding smooth Au film and observed into the far field after being converted into photons by the scattering ring ($120 \mu\text{m}$ internal radius, $1.5 \mu\text{m}$ width) surrounding the crystal.

The captured images were quantitatively analysed as in chapter 6. The SPP power detected at the different angles around the SPPC depends both on the wavelength and the orientation of the polarisation of the incident light with respect to the crystal axes. As seen in before, due to the TM nature of the SPP waves, the coupling efficiency to one eigenmode for a given wavelength is maximised when the electric field orientation of the incident light on the crystal coincides with the eigenmode orientation ($\alpha=\theta$ and $\theta+\pi$) [1, 49]. The wavelength dependence of the SPP detected power is a combination of the wavelength-dependent coupling efficiency to the several excited eigenmodes and the propagation of the eigenmodes on interfaces with unequal refractive indices, Au-air interface and Au-glass interface.

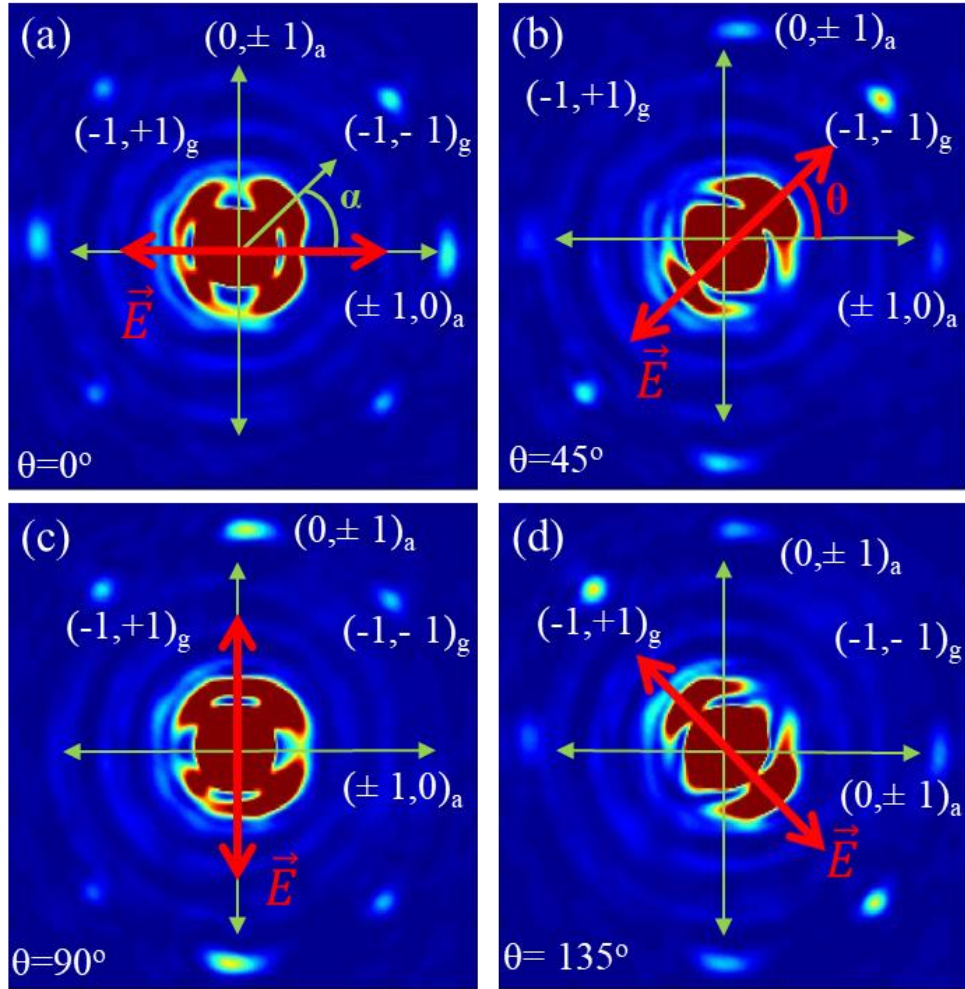


Fig. 6. 1. 1: Far-field intensity distributions measured for the SPPC in Fig. 7.

1. 1 (a) when illuminated with linearly polarized light with a 1539 nm wavelength and azimuth angles equal to a) 0° , b) 45° , c) 90° , and d) 135°

To investigate the wavelength dependence of the coupling efficiency combined with the propagation losses experienced by the four eigenmodes, the illuminating light polarisation state was set to be linear with azimuth angles $\theta = 0^\circ, 45^\circ, 90^\circ$, and 135° and its wavelength was varied from 1520 nm to 1560 nm with 1 nm step, for each of the

polarisation states. Fig. 6. 1. 2 (a) shows the SPP power integrated over $\Delta\alpha=\pm 15^\circ$ angular range around the four principal angles $\alpha= 0^\circ, 45^\circ, 90^\circ,$ and 135° of the scattering ring corresponding to the excited eigenmodes $(\pm 1,0)_a, (-1,-1)_g, (0,\pm 1)_a$ and $(-1,1)_g$, respectively, where notations “a” and “g” correspond to the modes of air-Au and glass-Au interfaces, as a function of the illuminating wavelength, after mathematically filtering out the substrate cavity. Since the eigenmodes propagate symmetrically with respect to the centre of the crystal, the detected power around angles with a 180° difference were added together to eliminate any power fluctuations due to misalignment between the fibre and the sample. The four eigenmodes have been plotted for the case that the polarisation state of the illuminating light is that required to maximise the coupling efficiency.

For a polarisation discriminator, to be self-calibrated, the polarisation states to be detected should have similar powers. Around the operating wavelength of 1539 nm, there is a 7 nm range over which there is less than 1 dB variation in the power around the four principal angles of the crystal, this range is defined in Fig. 7. 1. 3 (a) as “1 dB colorless bandwidth” and it is the wavelength range over which the device can operate without calibration. The device can work at the rest of the wavelength range between 1520 nm and 1560 nm if the detected power coupling to each eigenmode at a wavelength λ is calibrated, i.e. multiplied with a correcting factor equal to $\frac{P_{max,1539}}{P_{max,\lambda}}$ where $P_{max,1539}$ and $P_{max,\lambda}$, the power detected at each of the eigenmodes when the polarisation of the incident light is aligned with the direction of the eigenmode and the illuminating wavelength is 1539 nm and λ , respectively. Furthermore, the operating wavelength can be tuned to any value between ultraviolet to infrared by changing the structure period.

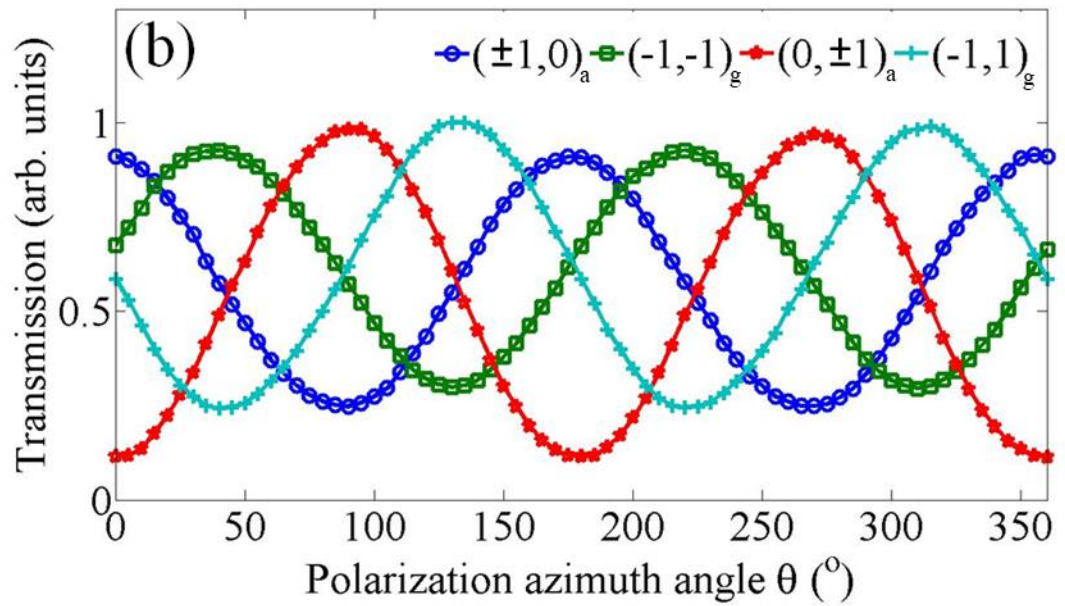
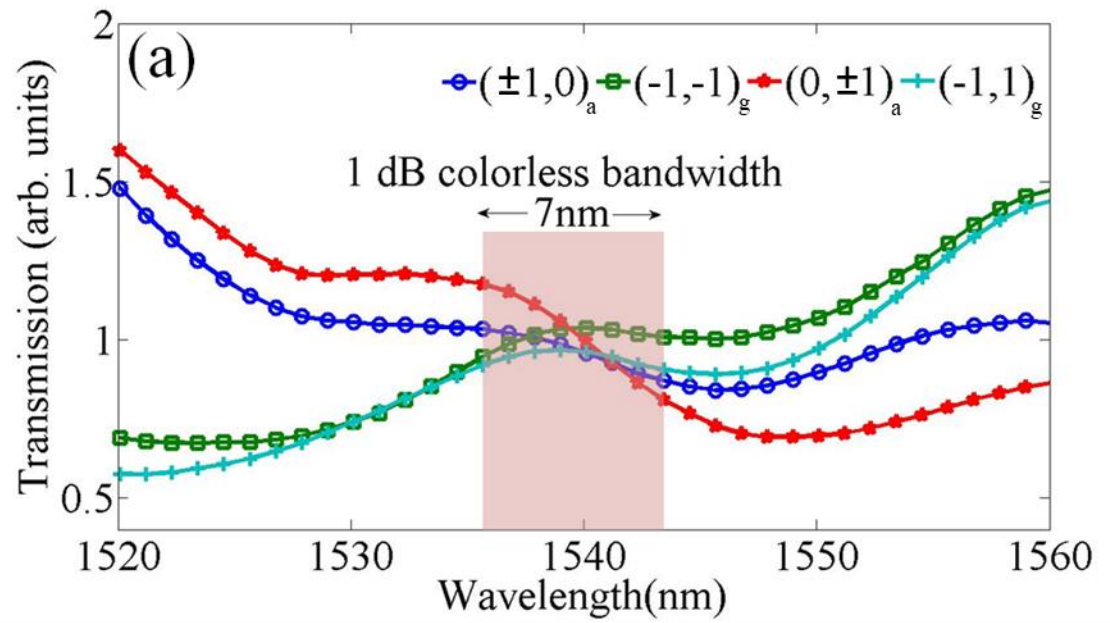


Fig. 6. 1. 2: a) Wavelength and b) polarisation dependences of the SPP signal transmission at the angular positions corresponding to the excited eigenmodes, measured at the scattering ring around the crystal

The polarisation dispersion properties of the device were characterised at its operating wavelength, $\lambda=1539$ nm. The polarisation state of the illuminating light was set to be linear with azimuth angle varied from 0° to 360° with a 5° step. Fig. 7. 1. 3 (b) shows the signal measured around the principal angles corresponding to the excited eigenmodes, as a function of the incident polarisation azimuth angle θ . It can be observed that signals polarised at azimuth angles $\theta = 0^\circ, 45^\circ, 90^\circ,$ and 135° can be uniquely analysed with a 6 dB extinction ratio and spatially separated at corresponding angles around the SPPC, making the device suitable for (being part of a) polarisation demultiplexer in photonic/plasmonic systems that use polarisation modulation to increase the bandwidth. Furthermore, the device can be used as a polarimetric device, to identify the azimuth angle of any photonic/plasmonic signal by measuring the power coupling to the four eigenmodes and thus identifying the Stokes parameters s_1 and s_2 .

The polarisation state of any photonic/plasmonic signal can be identified using the dimensionless Stokes parameters $s_1 = \frac{P_{LH}-P_{LV}}{P}$, $s_2 = \frac{P_{L+45^\circ}-P_{L-45^\circ}}{P}$, $s_3 = \frac{P_{RC}-P_{LC}}{P}$, where $P= P_{LH}+ P_{LV}$ and $P_{LH}, P_{LV}, P_{L+45^\circ}, P_{L-45^\circ}, P_{RC}$ and P_{LC} are the powers of the signal after passing through a polarising filter that allows only the part of the signal that is linearly polarised with azimuth angles 0° (horizontally polarised), 90° (vertically polarised), 45° , and -45° (or 135°), and right and left circularly polarised, respectively. The s_1 and s_2 Stokes parameters can be identified using the 4-level polarisation discriminator and measuring the power coupling to the four eigenmodes using the equations:

$$s_1 = \frac{P_{(\pm 1,0)} - P_{(0,\pm 1)}}{P_{(\pm 1,0)} + P_{(0,\pm 1)}}$$

$$s_2 = \frac{P_{(-1,-1)} - P_{(-1,1)}}{P_{(\pm 1,0)} + P_{(0,\pm 1)}}$$

Fig. 6. 1. 3 shows the comparison of the s_1 and s_2 parameters of 60 randomly elliptically polarised signals, at the operating wavelength, 1539 nm, as measured with the SPPC four-level polarisation discriminator and a benchtop polarimeter. The measurements are in good agreement. The polarisation discriminator/analyser is nondestructive since it capitalises on the high-transmission of the light through the nanostructured area and the weaker scattering into SPP waves that launch on the surrounding film, as well as on the fact that the light tunnelling through the nanostructured area maintains its polarisation. Furthermore, the azimuth angle can be measured in real-time and therefore the device can be used in-line in systems, like optical networks, that the polarisation of the signal needs to be monitored without being absorbed. The structure is also expected to be compatible with current CCD manufacturing process, contributing to polarisation dependent micro-vision and multichannel sensing.

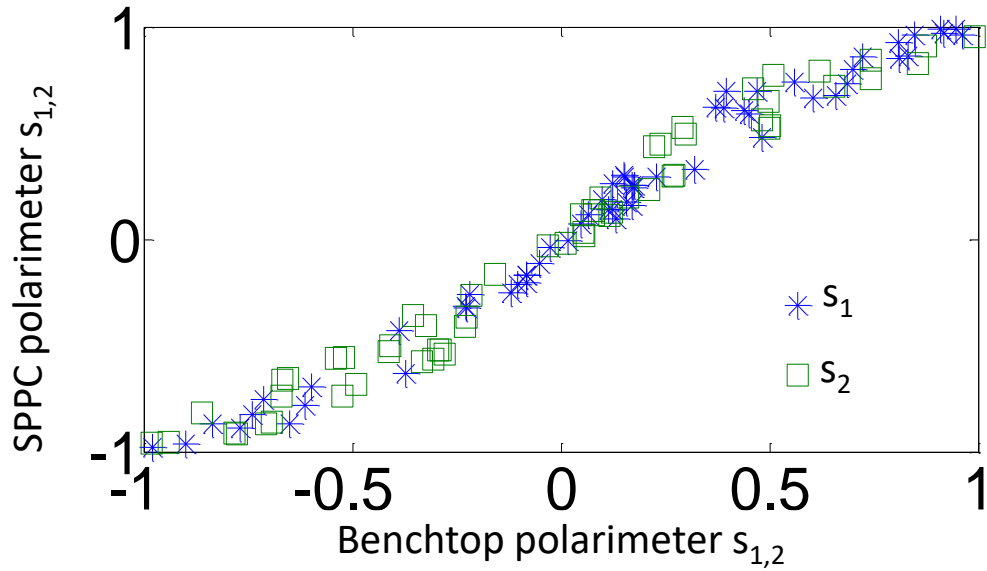


Fig. 6. 1. 3: Comparison of the S_1 and S_2 parameters of 60 random elliptical polarisation states as measured with the SPPC four-level polarisation discriminator and a benchtop polarimeter.

There are many of applications that use linear polarised light and in which the identification of the first two Stokes parameters is sufficient. However, in applications in which the helicity of the circular polarised light needs to be detected the identification of the third parameter is important. In order to realise a full polarimetric functionality it is necessary to be able to discriminate between left and right circular polarisation. This can be achieved by placing a $\lambda/4$ waveplate before the SPP based analyser. To make a compact, fibre-coupled polarimeter, a high-birefringence (HiBi) fibre can be used to provide this functionality. Circularly polarised light travelling over $(n+1/4)L$, where n integer and L the HiBi beat length, will be converted to a linear state of azimuth angle $+45^\circ$ if left circular (LC) and -45° if right circular (RC), which then can be resolved by the SPPC 4-

level polarisation analyser. Thus, the assembly of two SPPC structures and a $(n+1/4)L$ length of a high-birefringence fibre, shown in Fig. 6. 1. 5 (b), fulfils the same functionality as the bulky optical polarimeter shown in Fig. 6. 1. 5 (a), comprising a novel, microscale, compact and fibre-coupled polarimeter [6].

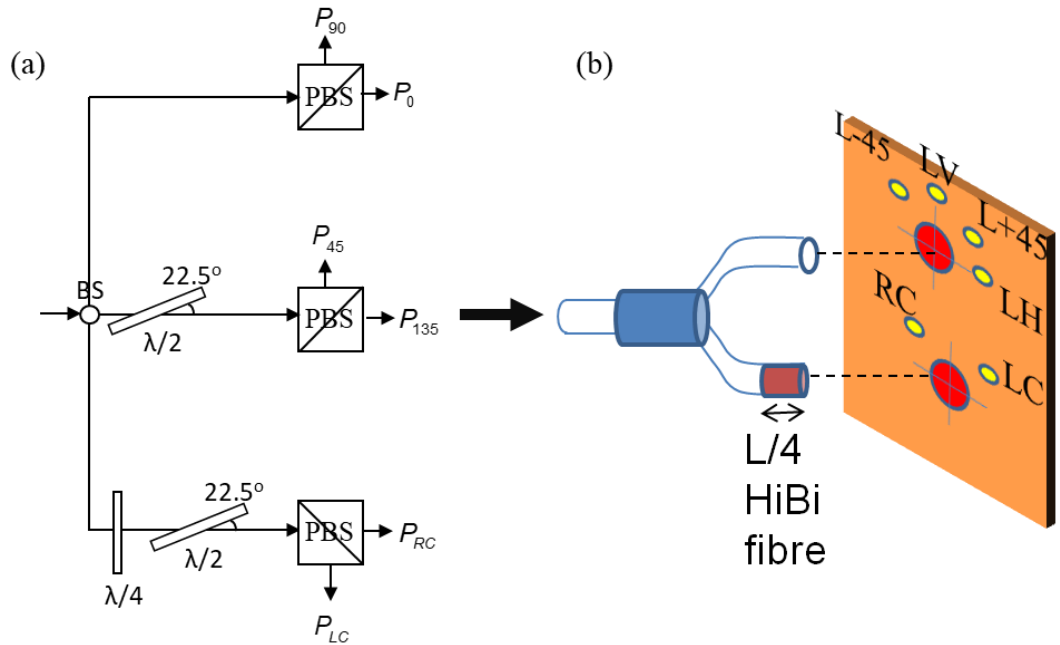


Fig. 6. 1. 5: The microscale polarimeter based on the SPPCs and high-birefringence assembly and its free space counterpart

Following the research presented in this chapter a number of research groups have realised compact microscale polarimeters that analyse the states of polarisations, determining the 3 Stokes parameters at a single detection based on the polarisation-dependent excitation of SPPs and metasurfaces. In particular in 2012 F. Afshinmanesh *et al.* realised a microscale, integrated plasmonic polarimeter based on the assembly of a set

of horizontal, vertical and diagonal nanoslits to identify the Stokes parameters s_1 and s_2 and a set of right-handed and left-handed chiral spiral grooves, to identify the s_3 Stokes parameter, all patterned on Au film and combined with silicon (Si) photodetectors [8]. The nanoslits behaved as linear polarisers scattering the light perpendicular to their axes while the right-handed spiral groove scattered the left circularly polarised light and vice versa. In 2014 Yu-Bo Xie *et al* presented a miniature polarisation analyser based on SPPs offering full polarimetric functionality by combining a set of bull's eye structures comprised of horizontal, vertical and diagonal apertures surrounded by 6 concentric periodical circular grooves, and a diagonal aperture surrounded with 6 elliptical periodical grooves [7]. The apertures surrounded with the circular grooves were behaving as linear polarisers scattering the light perpendicularly polarised to them, and thus were used for the identification of the Stokes parameters s_1 and s_2 and therefore the identification of the azimuth angle, while the circular grooves enhanced the coupling between the incident photons and the surface plasmons. The elliptical grooves provided the functionality of the $\lambda/4$ waveplate, transforming the circularly polarised to $\pm 45^\circ$ linearly polarised light, which then it was analysed with the diagonal aperture. All the bull's eyes structures were designed to scatter the corresponding polarisation with the same efficiency at the operating wavelength. Metasurfaces have been also applied to polarimeters by interweaving optical nanoantenna arrays [9-13, 161, 162]. These optical nanoantenna arrays determine the polarisation state of optical signals by diffracting four polarisation states, that form a basis for the state-of-polarisation space, in different directions either co-planar or in the far-field. Multifunctional polarimeters, which measure both a wavelength and a state of polarisation of incident light simultaneously have been also

suggested using the chromatic aberration of phase-gradient metasurfaces [11-13, 162]. Most of these compact, nanoscale polarimeters work in a narrow band around an operating wavelength, due to resonance nature of plasmonics and nanoantenna arrays. However, in 2018 an ultracompact, broadband, operating at a wavelength range of 300 nm, plasmonic polarimeter based on asymmetric geometric of the X-shaped apertures and the polarisation-sensitive excitation of surface plasmons was demonstrated by K. Lee *et al* [14]. Multifunctional polarimeters that measure two or more parameters of the incoming light simultaneously can be the next generation of optical systems, resulting in the increase of compactness. Their characteristics could either be optimised by design to work at a range of wavelengths or actively tuned to work at the desired wavelength range.

6.2 Summary

In conclusion a four-level polarisation discriminator/analyser, based on a SPPC able to uniquely spatially separate linearly polarised photonic/plasmonic signals with azimuth angles 0° , 45° , 90° and 135° has been experimentally demonstrated [5, 6, 52]. The device is based on an SPPC and is planar, micrometer scale, and easily integrable. It offers a 7 nm colorless bandwidth at which it is self-calibrated, while it can operate in a wider range of wavelength with simple calibration. Its operating wavelength can also be tuned across the whole range from ultraviolet to infrared by changing the SPPC period.

Such multi-level polarisation sensitive elements can be used to miniaturise the receiver for multi-level polarisation shift-keying systems, or for systems that combine polarisation and wavelength multiplexing to further increase the throughput in short-

distance transmission networks. It is also ideal for the miniaturisation of polarimetric systems and it can provide quality measurements of the s_1 and s_2 Stokes parameters, and thus unambiguously identify the azimuth angle of optical/plasmonic signals. Capitalising the high-transmittance through the nanostructure area and the weak coupling to SPP waves that launch in the surrounding smooth film, the device can offer non-destructive measurements of the azimuth angle used in-line in systems that the polarisation needs to be monitored but not absorbed like in optical networks. The device contributes in the miniaturisation of photonic circuits with applications in optical interconnects, microvision, multichannel sensing and in vivo medical measurements. Its combination with a length of high-birefringence fibre to detect the helicity and provide full polarimetric functionality, by determining in addition the s_3 Stokes parameter, has also been proposed [6]. The proposal of a microscale, compact polarimeter was welcomed from the scientific community which was inspired to realise several microscale compact polarimeters offering instant full polarimetric functionality based on the combination of polarisation-dependent excitation of SPPs in nanoslits, bull's eyes apertures and chiral structures [7, 8, 14] or metasurfaces [9-13, 161, 162]. Multifunctional polarimeters that measure two or more quantities of the incoming light simultaneously have also started to be realised [11-13, 162] and can be the next generation of optical systems, resulting in the increase of compactness. The operating wavelength of these devices depend on their geometrical characteristics and therefore can either be designed or actively tuned to work in the required wavelength ranging from ultraviolet to infrared.

7. Conclusions and future work

The research work described in this thesis was devoted to the further understanding of finite size SPPCs , the investigation of how their surface parameters can be manipulated to control the properties of the excited SPP beams, and the exploration of their potential use in short range optical interconnects for key telecommunications applications, such as information demultiplexing and power beam splitting, as well as the integration and the reduction in size, while aiming to increase sensitivity, of commonly used optical devices like polarimeters, wavemeters and misalignment detectors. The SPP eigenmodes excitation and propagation on SPPCs with several periods, boundary shapes and under several illumination conditions have been investigated both numerically and experimentally.

A numerical model, based on the point-dipole approximation, was developed during this thesis and was found to be in good agreement with experimental results taken with scanning near-field optical microscopy (SNOM). This can be used to explore the vast parameter space in the design of SPPCs that can allow the excitation of SPP beams and shape them to have the desired properties for each application.

By manipulating the SPPC boundary, the focusing (chapter 4) and the refraction (chapter 4 and 5) of the SPP beams launching from the SPPC to the surrounding film can be controlled. The excitation of SPP waves at several spectral areas, including the vicinity of the bandgaps has been investigated. Effects like the splitting of the SPP eigenmode at the vicinity of the bandgap, formed by the crossing of the two eigenmodes, has been

numerically and experimentally investigated (chapter 4 and 5). At the vicinity of the crossing point of two eigenmodes, the two eigenmodes flatten, the group velocity becomes zero, the SPP eigenmodes do not propagate and the SPP beam splits. At the vicinity of the crossing points of the $(0, -1)$ and $(0, 1)$ eigenmodes at the Au-air interface the SPP beams have been shown to split in $2/4$ (2 in each facet) prongs, with the prongs belonging one in the $(0,-1)$ eigenmode and the other in the $(0, 1)$ eigenmode, experiencing positive and negative wavelength dispersion/group velocity/refractive index respectively and thus positive/negative refractive index when crossing the SPPC boundary and launch on the surrounding smooth metal film. The angular separation between the two prongs and the sensitivity of the splitting ratio to the misalignment can be controlled by engineering the SPPC boundary. In particular the angular separation between the two prongs in which the $(0,\pm 1)$ eigenmode at the air-metal interface splits at the vicinity of the SPP bandgap, when excited at a $40\ \mu\text{m}$ diameter circular boundary SPPC with square lattice $1400\ \text{nm}$ period and detected $60\ \mu\text{m}$ from the SPPC centre, was double the angular separation by the equivalent square boundary one. The square structure splits in 1:1 ratio between the two prongs of the same facet and is more robust to the misalignment between the SPPC centre and the illumination spot centre. On the other hand the power ratio between the two prongs of the circular structure can be controlled by the SPPC-illumination spot centres misalignment, providing the opportunity to design micro-beam splitters with any random splitting ratio. Indeed a 1×2 power beam splitter with a splitting ratio 5:4, based on a circular boundary SPPC has been experimentally demonstrated during the course of this thesis. The splitting ratio of such a device can be actively controlled if connected with a piezoelectric microsystem. In inverse thinking such a

device can be used as microscale misalignment detector able to detect misalignment of the order of a couple micrometres.

Following the concept that at the vicinity of the spectral areas where the eigenmode dispersion tends to flat, i.e. $\left(\frac{dk_{SPP-Bragg}}{d\omega}\right) \gg 0$, the SPP wave will experience a large difference in its propagation direction for a small change in its frequency, which the same as the frequency of the illuminating light and inversely proportional to the illuminating light wavelength. The negative/positive wavelength dispersion of the SPPC eigenmodes were experimentally investigated along their potential suitability for dense wavelength demultiplexing. The SPPCs were illuminated using a single mode fibre (N.A: 0.13) and the SPP waves around the SPPC were imaged in the far-field after coupling back into light through a 60 μm internal radius and 1.5 μm width scattering ring surrounding the SPPC. As it was experimentally observed that the SPPC wavelength dispersion properties were affected by the Fabry-Perot cavity formed between the substrate facets, the wavelength dispersion properties were characterised both as measured and after mathematically filtering out the substrate cavity. In that way the eigenmode wavelength dispersion characterisation was isolated by the influence of the substrate cavity. SPPCs samples of a square lattice and square/circular SPPC boundaries were characterised in terms of wavelength angular beam separation (WABS), passband and crosstalk. Although the characterisation offered some highly desirable values for WABS the crosstalk values were extremely high compared to conventional demultiplexers. The WABS was $\pm 1^\circ/\text{nm}$ and the crosstalk more than -0.16dB if the substrate Fabry-Perot cavity was mathematically filtered out. The substrate Fabry-Perot cavity enhanced the SPPC wavelength demultiplexing ability, increasing the WABS to $\pm 32^\circ/\text{nm}$ - $36^\circ/\text{nm}$ and decreasing the

crosstalk to -0.45 dB (square boundary SPPC) - -0.21 dB (circular boundary SPPC). If the set-up was to be used for dense wavelength demultiplexing it would need to be combined with high sensitivity detectors with a minimal detectable power difference less than 0.40 dB for the square structure and less than 0.20 dB, for the circular boundary structure. The assembly of the plasmonic crystal with high-sensitivity detectors can also be used as a planar microscale high-sensitivity wavemeter. Indeed the square structure is able to distinguish wavelengths with a 0.1 nm wavelength difference, if combined with a detector with a minimal detectable power difference less than 0.40 dB, while the circular structure is able to distinguish wavelengths with a 0.5 nm wavelength difference is combined with a detector with a minimal detectable power difference less than 0.20 dB, Such wavemeters can be used for the detection of small refractive index differences, with potential applications in diagnostic medicine and high-precision nanofabrication.

In section 5.3 a broadband 2-channel microscale wavelength demultiplexer has been experimentally demonstrated based on the coupling to the SPP eigenmodes excited on the two different metal-dielectric interfaces of the SPPC, namely the Au-air and Au-glass interfaces. The $(\pm 1, 0)$ eigenmodes excited at the Au-air interface are spectrally located close to the $(-1, \pm 1)$ eigenmodes excited at the Au-glass interface. By illuminating the sample through a single-mode fibre (N.A: 0.13), i.e. illuminating simultaneously at the angles is 0° - 7° , the eigenmodes on both interfaces can be excited and couple back to light through the scattering ring connecting the two interfaces. The 2-channel broadband wavelength demultiplexer demultiplexes 1509 nm and 1564 nm, offering a 55 nm channel spacing. Due to the TM nature of the SPP eigenmodes, i.e. the preferential coupling of the light to the eigenmodes that propagate in a direction parallel to its electric field vector

the crosstalk between the two channels depend on the polarisation of the light travelling in these channels. When the wavelength multiplexing is combined with polarisation multiplexing, and each channel is polarised parallel to the eigenmode that it couples. i.e the channels at 1509 nm and 1564 nm, are linearly polarised with azimuth angles 0° and 45° respectively, the crosstalk is -3dB. The same is expected when the light traveling in the two channels is circularly polarised or unpolarised, as in that scenario- the light will not demonstrate any preferential coupling. However, in any other scenario in which the polarisation of the illuminating light reinforces the coupling either to the eigenmode detected around the angular positions $\alpha=-1^\circ$ or $\alpha=44^\circ$, then the crosstalk between the channels can increase up to -0.59 dB. This can be easily solved by adding the powers from detectors located at angular positions α and $\alpha+90^\circ$; the eigenmodes propagating in such directions have the same wavelength dispersion but converse coupling polarisation dependence.

Taking advantage of the TM nature of the SPP waves, a planar, micro-scale, 4-level polarisation discriminator has been experimentally demonstrated based on an SPPC. The device is able to uniquely spatially separate linearly polarised signals with azimuth angles 0° , 45° , 90° and 135° , and identify the s_1 and s_2 Stokes parameters of elliptically polarised signals. To provide a full polarimetric functionality-i.e. to identify all 3 Stokes parameters s_1 , s_2 and s_3 a combination of 2 SPPCs and a $\lambda/4$ length of a high-birefringence fibre was proposed [6]. This inspired a number of scientists to propose other combinations of plasmonic structures for polarimetric applications such as the combination of plasmonic nano-slits with chiral structures [15].

The main direction of future work would be to investigate ways to decrease the cross-talk and investigate if fine wavelength demultiplexing using SPPCs can be of practical use. One possible reason for the high crosstalk is the illumination of an extended spectral area, due to the numerical aperture of the illuminating fibre (N.A.:0.13), covering a range of illumination angles 0° - 7° . The difficulty here was to produce a collimated beam with a spot radius $\omega_0 \approx 20 \mu\text{m}$, such as to illuminate the SPPC but not the scattering ring. At the wavelength range examined the flat area of the $(0, \pm 1)$ eigenmodes cover only 2° , so the maximum incident range of incident angles to be covered should have been close to 0.2° , corresponding to a numerical aperture equal to 0.0035. Alternatively a more extended flat spectral area is located at the wavelength range 1450 nm- 1500 nm, close to the centre of the Brillouin zone, where the $(\pm 1, 1)$ eigenmodes at the Au-glass interface are crossing. This area is extended over 7° and it could potentially be characterised with an illumination system with a maximum of 0.7° range of illumination angles, corresponding to a numerical aperture equal to 0.012. A possible solution to this is the illumination of the sample through a waveguide/ photonic crystal fibre which would illuminate a much smaller range of angles or the use of grin (gradient index) lens which is able to produce a small radius collimated beam if positioned at the end of a fibre. Indeed, near-infrared antireflective coated grin lenses able to produce a $120 \mu\text{m}$ diameter collimated lens when connected to a singlemode fibre patchcord are available commercially. In this scenario, we would need to have a scattering with a bigger internal radius (more than $100 \mu\text{m}$), so it is not illuminated by the incident beam. Having a scattering ring with an internal radius of $346 \mu\text{m}$ positioned around the circular crystal or of $450 \mu\text{m}$ positioned around the square crystal, would be in advantage of the wavelength characterisation as according to

Fig. 4. 3. 1. 2, these are the eigenmode focal distance for the two structures. If needed the focal distance can be reduced by reducing the SPPC size or by manipulating its boundary curvature (as seen in Fig. 4. 3. 1.2). Furthermore, it would be interesting to examine if differently shaped lattices produce eigenmodes with a more extended flat area. The design of an SPPC with a more extended spectral area over which the eigenmode would be flat, would also be beneficial as this would give a larger range of angles to investigate. The spectral area over which the ‘flatness’ of the eigenmode is extended depends mainly on the structure of the lattice and less from the shape/ size of the holes as this will change the refractive index distribution along the SPPC surface. An extended spectral area over which $\left(\frac{dk_{SPP-Bragg}}{d\omega}\right) \gg 0$ would give a larger range of angles α around the SPPC to investigate. Another factor which can be engineered to increase the angular separation of the various SPP beams is the SPPC boundary. For this the model described in section 4.2 could be used to optimise the boundary shape before manufacturing the sample.

Appendix 1: Derivation of the dispersion relation of surface plasmon polaritons-smooth metal-dielectric interface

The dispersion relation of a surface plasmon on a smooth metal-dielectric interface can be easily derived starting from the Maxwell' equations (Eq. app. 1. 1)

$$\left. \begin{aligned} \vec{\nabla} \vec{D} &= \rho_{ext} \\ \vec{\nabla} \vec{B} &= 0 \\ \vec{\nabla} \times \vec{E} &= -\frac{\partial \vec{B}}{\partial t} \\ \vec{\nabla} \times \vec{H} &= \vec{J}_{ext} + \frac{\partial \vec{D}}{\partial t} \end{aligned} \right\} \text{Eq. app. 1. 1}$$

where \vec{D} the dielectric displacement, \vec{E} the electric field, \vec{H} the magnetic field and \vec{B} the magnetic induction or magnetic flux density, while ρ_{ext} and \vec{J}_{ext} the external charge and current densities, which in our case is zero, and the constitutive relations (Eq. app. 1. 2), which always stand for linear, isotropic and nonmagnetic media [85]), which always stand for linear, isotropic and nonmagnetic media [85]

$$\left. \begin{aligned} \vec{D} &= \epsilon_0 \epsilon \vec{E} \\ \vec{B} &= \mu_0 \vec{H} \end{aligned} \right\} \text{Eq. app. 1. 2}$$

where ϵ_0 , μ_0 the dielectric permittivity and the permeability of the vacuum and ϵ the relative dielectric constant of the medium.

For simplicity an one-dimensional problem can be assumed, i.e. the SPP wave to propagate along the x-direction and to show no spatial variation in the y-direction. Thus the propagating SPP waves can be described by the general formulas

$$\left. \begin{aligned} \vec{E}_{1,2}(x, y, z) &= \vec{E}_{1,2} e^{ik_x x} e^{\pm k_{z1,2} z} \\ \vec{H}_{1,2}(x, y, z) &= \vec{H}_{1,2} e^{ik_x x} e^{\pm k_{z1,2} z} \end{aligned} \right\} \text{Eq. app. 1. 3}$$

where + is for $z > 0$ and – for $z < 0$, in order to describe waves confined to the surface.

For the case that the dielectric constant ϵ can be assumed constant over distances of the order of wavelength, Eq. app. 1. 1, Eq. app. 1. 2 and Eq. app. 1. 3 can be combined to produce the wave equation (Eq. app. 1. 4)

$$\nabla^2 \vec{E} + k_0^2 \epsilon \vec{E} = 0 \quad \text{Eq. app. 1. 4}$$

where $k_0 = \omega/c$, the wave vector of the propagating wave in vacuum.

Combining equations Eq. app. 1. 1, Eq. app. 1. 2 and Eq. app. 1. 3 and Eq. app. 1. 4 and assuming harmonic time dependence $\left(\frac{\partial}{\partial t} = -i\omega\right)$ we arrive at the set of coupled equations:

$$\left. \begin{aligned}
\frac{\partial E_y}{\partial z} &= -i\omega\mu_0 H_x \\
\frac{\partial E_x}{\partial z} - ik_x E_z &= i\omega\mu_0 H_y \\
ik_x E_y &= i\omega\mu_0 H_z \\
\frac{\partial H_y}{\partial z} &= i\omega\varepsilon_0 \varepsilon E_x \\
\frac{\partial H_x}{\partial z} - ik_x H_z &= -i\omega\varepsilon_0 \varepsilon E_y \\
ik_x H_y &= -i\omega\varepsilon_0 \varepsilon E_z
\end{aligned} \right\} \text{Eqs. App. 1. 5}$$

Eqs. App. 1. 5 allow two sets of self-consistent solutions with different polarisation properties of the propagating waves; the transverse magnetic (TM or p) modes and the transverse electric (TE or s) modes.

For the transverse magnetic (p-polarised) modes the non-zero components are E_x , E_z and H_y and thus the wave propagation is described by the Eqs. App. 1. 6.

$$\left. \begin{aligned}
E_x &= -i \frac{1}{\omega\varepsilon_0\varepsilon} \frac{\partial H_y}{\partial z} & (a) \\
E_z &= -\frac{k_x}{\omega\varepsilon_0\varepsilon} H_y & (b) \\
\frac{\partial H_y}{\partial z^2} + (k_0^2\varepsilon - k_x^2)H_y &= 0 & (c)
\end{aligned} \right\} \text{Eqs. App. 1. 6}$$

Applying equations (Eqs. App. 1. 6) at the dielectric ($z>0$) and the metal ($z<0$) areas and taking into account the general electric and magnetic field formulas (Eq. app. 1. 3) yield to the formulas Eqs. App. 1. 7 and Eqs. App. 1. 8 which describe the electric and magnetic field components in the two areas.

For $z>0$

$$\begin{aligned}
 H_y &= A_d e^{ik_x x} e^{-k_{zd} z} & (a) \\
 E_x &= iA_d \frac{1}{\omega \epsilon_0 \epsilon_d} k_{zd} e^{ik_x x} e^{-k_{zd} z} & (b) \\
 E_z &= -A_d \frac{k_x}{\omega \epsilon_0 \epsilon_d} k_{zd} e^{ik_x x} e^{-k_{zd} z} & (c)
 \end{aligned}
 \left. \vphantom{\begin{aligned} H_y \\ E_x \\ E_z \end{aligned}} \right\} \text{Eqs. App. 1. 7}$$

For $z<0$

$$\begin{aligned}
 H_y &= A_m e^{ik_x x} e^{k_{zm} z} & (a) \\
 E_x &= -iA_m \frac{1}{\omega \epsilon_0 \epsilon_m} k_{zm} e^{ik_x x} e^{k_{zm} z} & (b) \\
 E_z &= -A_m \frac{k_x}{\omega \epsilon_0 \epsilon_m} k_{zm} e^{ik_x x} e^{k_{zm} z} & (c)
 \end{aligned}
 \left. \vphantom{\begin{aligned} H_y \\ E_x \\ E_z \end{aligned}} \right\} \text{Eqs. App. 1. 8}$$

Continuity requirements for H_y and E_x at the interface yield to Eq. app. 1. 9 and Eq. app. 1. 10 correspondingly

$$A_d = A_m \quad \text{Eq. app. 1. 9}$$

$$\frac{k_{zm}}{k_{zd}} = -\frac{\epsilon_m}{\epsilon_d} \quad \text{Eq. app. 1. 10}$$

Eq. app. 1. 10 requires that $\text{Re}[\epsilon_m] < 0$ if $\epsilon_d > 0$, which means that the SPP waves can only exist at the a metal-dielectric interface.

Furthermore substituting the H_y at the wave equation Eqs. App. 1. 6 © with Eqs. App. 1. 7 (a) and Eqs. App. 1. 8 (a) for the metal and dielectric areas correspondingly yields to the equations Eq. app. 1. 11

$$\left. \begin{aligned} k_{z_m}^2 &= k_x^2 - k_0^2 \varepsilon_m \\ k_{z_d}^2 &= k_x^2 - k_0^2 \varepsilon_d \end{aligned} \right\} \text{Eq. app. 1. 11}$$

Combining Eq. app. 1. 10 and Eq. app. 1. 11 the dispersion relation (Eq. app. 1. 12) of the SPP waves on a smooth metal-dielectric interface is derived.

$$k_x = \frac{\omega}{c} \sqrt{\frac{\varepsilon_m \varepsilon_d}{\varepsilon_m + \varepsilon_d}} \quad \text{Eq. app. 1. 12}$$

Appendix 2: The transverse magnetic (TM) nature of surface plasmons (SPs)

In the case of s-polarised (transverse electric) modes, the non-zero components are H_x , H_z and E_y . Thus the equations describing the wave propagation are given by Eq. app. 2. 1. [85].

$$\left. \begin{aligned} H_x &= i \frac{1}{\omega \mu_0} \frac{\partial E_y}{\partial z} \\ H_z &= \frac{k_x}{\omega \mu_0} E_y \\ \frac{\partial^2 E_y}{\partial z^2} + (k_0^2 \varepsilon - k_x^2) E_y &= 0 \end{aligned} \right\} \text{Eq. app. 2. 1}$$

Applying equations Eq. app. 2. 1 for the dielectric ($z > 0$) and the metal ($z < 0$) areas and taking into account the general formulas (Eq. app. 1. 3) for the electric and magnetic fields, electric and magnetic field components can be described by the formulas Eq. app. 2. 2 and Eq. app. 2. 3 correspondingly.

For $z > 0$

$$\left. \begin{aligned} E_y &= A_d e^{ik_x x} e^{-ik_{zd} z} \\ H_x &= \frac{1}{\omega \mu_0} k_{zd} A_d e^{ik_x x} e^{-ik_{zd} z} \\ H_z &= \frac{k_x}{\omega \mu_0} A_d e^{ik_x x} e^{-ik_{zd} z} \end{aligned} \right\} \text{Eq. app. 2. 2}$$

For $z < 0$

$$\left. \begin{aligned} E_y &= A_m e^{ik_x x} e^{ik_{z_m} z} \\ H_x &= -\frac{1}{\omega \mu_0} k_{z_m} A_m e^{ik_x x} e^{ik_{z_m} z} \\ H_z &= \frac{k_x}{\omega \mu_0} A_m e^{ik_x x} e^{ik_{z_m} z} \end{aligned} \right\} \text{Eq. app. 2. 3}$$

Continuity requirement for E_y at the interface ($z=0$) yields

$$A_m = A_d = A \quad \text{Eq. app. 2. 4}$$

Continuity requirement for H_x at the interface, combined with Eq. app. 2. 4 yields

$$A \cdot (k_{z_d} + k_{z_m}) = 0 \quad \text{Eq. app. 2. 5}$$

Since confinement to the surface requires $\text{Re}[k_{z_d}] > 0$ and $\text{Re}[k_{z_m}] > 0$

$$(\text{Eq. app. 2. 5}) \quad \Rightarrow \quad A = 0 \quad \text{Eq. app. 2. 6}$$

Eq. app. 2. 6 indicates that surface plasmons can only be TM polarised.

Appendix 3: Green-tensor numerical model and Matlab code for the simulation of the SPP excitation and propagation on and around SPPCs

In this appendix the steps followed to solve the NxN linear equations system described by Eq. 4. 2. 1 to calculate the electric field at the SPPC holes, modeled as point scatterers are shown. Once the electric field at the point scatterers has been calculated, the electric field at any other point on and around the SPPC can be easily calculated.

i) Eq. 4. 2. 1 and Eq. 4. 2. 2 were combined in Eq. app. 3. 1.

$$\vec{E}_{sc_i}(\vec{r}) = \vec{E}_{sc_i}^0(\vec{r}) + \frac{k_0^2}{\epsilon_0} \sum_{i=1, i \neq j}^N \underline{G}_{SPP}(\vec{r}_i, \vec{r}_j) \underline{a}_d \vec{E}_{sc_j} \quad \text{Eq. app. 3. 1}$$

which was written in matrix format as

$$\vec{A} \cdot \vec{E}_{sc} = \vec{b} \quad \text{Eq. app. 3. 2}$$

and thus

$$\vec{E}_{sc} = \vec{A}^{-1} \vec{b} \quad \text{Eq. app. 3. 3}$$

where \vec{A} , is the matrix describing the interaction of each one of the scatterers with all the others and is given by Eq. app. 3. 4 , \vec{b} is the matrix describing the incident field upon the scatterers, and \vec{E}_{sc} is the matrix describing the electric field on each of the scatterers. The matrices \vec{b} and \vec{E}_{sc} are described in Eq. app. 3. 5.

$$\vec{A} = -k_0^2 \begin{bmatrix} -\frac{\epsilon_0}{k_0^2} & 0 & 0 & (\underline{Ga}_d)_{xx,1,2} & (\underline{Ga}_d)_{yy,1,2} & (\underline{Ga}_d)_{zz,1,2} & \dots & (\underline{Ga}_d)_{xx,1,N} & (\underline{Ga}_d)_{yy,1,N} & (\underline{Ga}_d)_{zz,1,N} \\ 0 & -\frac{\epsilon_0}{k_0^2} & 0 & (\underline{Ga}_d)_{yx,1,2} & (\underline{Ga}_d)_{yy,1,2} & (\underline{Ga}_d)_{yz,1,2} & \dots & (\underline{Ga}_d)_{yx,1,N} & (\underline{Ga}_d)_{yy,1,N} & (\underline{Ga}_d)_{yz,1,N} \\ 0 & 0 & -\frac{\epsilon_0}{k_0^2} & (\underline{Ga}_d)_{zx,1,2} & (\underline{Ga}_d)_{zy,1,2} & (\underline{Ga}_d)_{zz,1,2} & \dots & (\underline{Ga}_d)_{zx,1,N} & (\underline{Ga}_d)_{zy,1,N} & (\underline{Ga}_d)_{zz,1,N} \\ (\underline{Ga}_d)_{xx,2,1} & (\underline{Ga}_d)_{yy,1,2} & (\underline{Ga}_d)_{zz,1,2} & -\frac{\epsilon_0}{k_0^2} & 0 & 0 & \dots & (\underline{Ga}_d)_{xx,2,N} & (\underline{Ga}_d)_{yy,2,N} & (\underline{Ga}_d)_{zz,2,N} \\ (\underline{Ga}_d)_{yx,2,1} & (\underline{Ga}_d)_{yy,2,1} & (\underline{Ga}_d)_{yz,2,1} & 0 & -\frac{\epsilon_0}{k_0^2} & 0 & \dots & (\underline{Ga}_d)_{yx,2,N} & (\underline{Ga}_d)_{yy,2,N} & (\underline{Ga}_d)_{yz,2,N} \\ (\underline{Ga}_d)_{zx,2,1} & (\underline{Ga}_d)_{zy,2,1} & (\underline{Ga}_d)_{zz,2,1} & 0 & 0 & -\frac{\epsilon_0}{k_0^2} & \dots & (\underline{Ga}_d)_{zx,2,N} & (\underline{Ga}_d)_{zy,2,N} & (\underline{Ga}_d)_{zz,2,N} \\ \cdot & \cdot & \cdot & \cdot & \cdot & \cdot & \dots & \cdot & \cdot & \cdot \\ \cdot & \cdot & \cdot & \cdot & \cdot & \cdot & \dots & \cdot & \cdot & \cdot \\ \cdot & \cdot & \cdot & \cdot & \cdot & \cdot & \dots & \cdot & \cdot & \cdot \\ \cdot & \cdot & \cdot & \cdot & \cdot & \cdot & \dots & \cdot & \cdot & \cdot \\ (\underline{Ga}_d)_{xx,N,1} & (\underline{Ga}_d)_{yy,N,1} & (\underline{Ga}_d)_{zz,N,1} & (\underline{Ga}_d)_{xx,N,2} & (\underline{Ga}_d)_{yy,N,2} & (\underline{Ga}_d)_{zz,N,2} & \dots & -\frac{\epsilon_0}{k_0^2} & 0 & 0 \\ (\underline{Ga}_d)_{yx,N,1} & (\underline{Ga}_d)_{yy,N,1} & (\underline{Ga}_d)_{yz,N,1} & (\underline{Ga}_d)_{yx,N,2} & (\underline{Ga}_d)_{yy,N,2} & (\underline{Ga}_d)_{yz,N,2} & \dots & 0 & -\frac{\epsilon_0}{k_0^2} & 0 \\ (\underline{Ga}_d)_{zx,N,1} & (\underline{Ga}_d)_{zy,N,1} & (\underline{Ga}_d)_{zz,N,1} & (\underline{Ga}_d)_{zx,N,2} & (\underline{Ga}_d)_{zy,N,2} & (\underline{Ga}_d)_{zz,N,2} & \dots & 0 & 0 & -\frac{\epsilon_0}{k_0^2} \end{bmatrix}$$

Eq. app. 3. 4

$$\vec{b} = \begin{bmatrix} E_{sc,x,1}^{in} \\ E_{sc,y,1}^{in} \\ E_{sc,z,1}^{in} \\ E_{sc,x,2}^{in} \\ E_{sc,y,2}^{in} \\ E_{sc,z,2}^{in} \\ \cdot \\ \cdot \\ \cdot \\ \cdot \\ E_{sc,x,N}^{in} \\ E_{sc,y,N}^{in} \\ E_{sc,z,N}^{in} \end{bmatrix}, \quad \vec{E}_{sc} = \begin{bmatrix} E_{sc,x,1} \\ E_{sc,y,1} \\ E_{sc,z,1} \\ E_{sc,x,2} \\ E_{sc,y,2} \\ E_{sc,z,2} \\ \cdot \\ \cdot \\ \cdot \\ \cdot \\ E_{sc,x,N} \\ E_{sc,y,N} \\ E_{sc,z,N} \end{bmatrix}$$

Eq. app. 3. 5

ii) The Green dyadid tensor for every m-n scatterer pair, $\underline{G}_{mn}^{SPP}(p, \varphi, z)$, given by Eq. 4. 2. 8, was written in cartesian coordinates, $\underline{G}_{mn}^{SPP}(x, y, z)$, using Eq. app. 3. 6 and in a matrix format as shown in Eq. app. 3. 7.

$$\hat{p} = \frac{(x_m - x_n)\hat{x} + (y_m - y_n)\hat{y}}{\sqrt{(x_m - x_n)^2 + (y_m - y_n)^2}} \quad \text{Eq. app. 3. 6}$$

$$\underline{G}_{mn}^{SPP}(x, y, z) = -\frac{i\alpha k_{SPP} H_0^{(1)}(k_{SPP} p) e^{-\alpha k_{SPP}(z+z')}}{2(1-a^4)(1-a^2)} (\hat{x}, \hat{y}, \hat{z}) \begin{pmatrix} \alpha^2 x_{ef_{mn}}^2 & \alpha^2 x_{ef_{mn}} y_{ef_{mn}} & -i\alpha x_{ef_{mn}} \\ \alpha^2 x_{ef_{mn}} y_{ef_{mn}} & \alpha^2 y_{ef_{mn}}^2 & -i\alpha y_{ef_{mn}} \\ i\alpha x_{ef_{mn}} & i\alpha y_{ef_{mn}} & 1 \end{pmatrix} \begin{pmatrix} \hat{x} \\ \hat{y} \\ \hat{z} \end{pmatrix} \quad \text{Eq. app. 3. 7}$$

$$\text{where } x_{ef_{mn}} = \frac{x_m - x_n}{p_{mn}}, \quad y_{ef_{mn}} = \frac{y_m - y_n}{p_{mn}}, \quad \text{and } p_{mn} = \sqrt{(x_m - x_n)^2 + (y_m - y_n)^2}.$$

iii) The NxN $\vec{\vec{H}}$ matrix was formed

$$H(m,n) = \underline{G}_{mn}^{SPP}(x, y, z) \underline{a}_d,$$

where $m=1,2,3,\dots,N$, $n=1,2,3,\dots,N$, and \underline{a}_d is given by equation Eq. app. 3. 8

$$\underline{a}_d = a_0(\hat{x}, \hat{y}, \hat{z}) \begin{pmatrix} \frac{1}{1+\xi\beta} & 0 & 0 \\ 0 & \frac{1}{1+\xi\beta} & 0 \\ 0 & 0 & \frac{1}{1+2\xi\beta} \end{pmatrix} \begin{pmatrix} \hat{x} \\ \hat{y} \\ \hat{z} \end{pmatrix} \quad \text{Eq. app. 3. 8}$$

iv) The 4-dimensional $\vec{\vec{T}}$ matrix was formed as follows

$$T(t_1, t_2, t_3, t_4) = H_{mm}(t_1, t_2) \text{ if } t_3 \neq t_4$$

$$T(t_1, t_2, t_3, t_4) = -\frac{1}{k_0^2} \text{ if } t_3 = t_4 \text{ and } t_1 = t_2$$

$$T(t_1, t_2, t_3, t_4) = 0 \text{ if } t_3 = t_4 \text{ and } t_1 \neq t_2$$

where t_3 and t_4 run between 1:N corresponding to the scatterers, and t_1 and t_2 run between 1:3 corresponding to the x,y,z coordinates of the scatterers t_3 and t_4 , correspondingly.

- v) The values of the matrix \vec{T} where inserted in Eq. app. 3. 4 to calculate the matrix \vec{A}
- vi) The matrix \vec{b} (Eq. app. 3. 5) was formed depending on the illumination scheme, Using Eq. 4. 2. 11, for x-polarised collimated illumination, and Eq. 4. 2. 12 for x-polarised strongly focused illumination
- vii) The electric field values at the points of the scatterers, \vec{E}_{sc} , were calculated using Eq. app. 3. 3.
- viii) The electric field at any point P of the X-Y grid, besides the scatterer-points was calculated using Eq. app. 3. 9.

$$\vec{E}_P = -iak_{spp} \frac{k_o^2}{\epsilon_0} e^{-ak_{spp}(z+z_p)} \sum_{m=1}^N H_0^{(1)}(k_{spp}P) \underline{G}_{Pm}^{SPP} \underline{a}_d \vec{E}_{sc,m} \quad \text{Eq. app. 3. 9}$$

Appendix 4: Description of the algorithm to automatically set-up the desired polarisation state

App.4.1 Operational principle of the polarisation controller

Before analysing the algorithm used to automatically set-up the desired polarisation state, it is important to describe the operation principle of the Anritsu polarisation controller, used in the experiments. The polarisation controller consists of a four-fibre-loop assembly each one optimised to approximate a quarter-wave retarder. The polarisation is adjusted by independently adjusting each loop over an angular range of 180° (Fig. app. 4. 1. 1). This range is divided into 1000 equal steps (000-999) providing an adjustment resolution of 0.18° . For a given input polarisation state, the output polarisation state depends on the four fibre-loop positions.

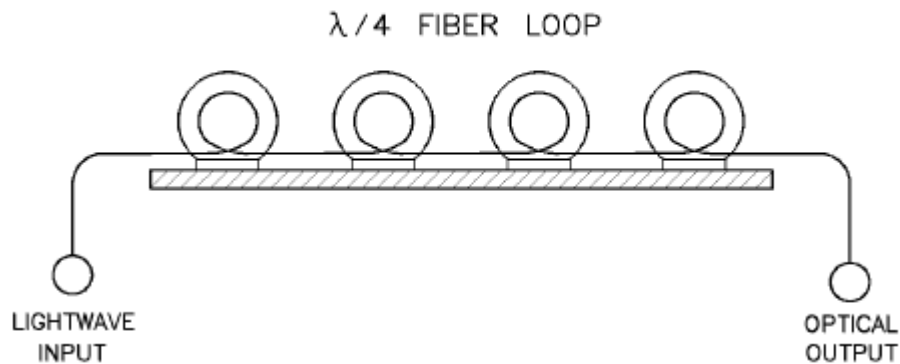


Fig. app. 4. 1. 1: Operation principle of the polarisation controller

App.4.2 Polarisation measurement with a polarimeter

A polarimeter expresses the measured polarisation state using the Stokes vector and the Poincare sphere. The Poincare sphere (Fig. app. 4. 2. 1) is a graphical tool in the real 3-dimensional space to describe polarised signals; any state can be uniquely represented by a point on or within a unit sphere centred on a rectangular xyz-coordinate system. Fully polarised signals are represented with a point on the sphere; the point coordinates are the normalised stokes parameters, while points close together represent similar polarisation states [163] Fully polarised signals are represented with a point on the sphere; the point coordinates are the normalised stokes parameters, while points close together represent similar polarisation states [163] Fully polarised signals are represented with a point on the sphere; the point coordinates are the normalised stokes parameters, while points close together represent similar polarisation states [163]) is a graphical tool in the real 3-dimensional space to describe polarised signals; any state can be uniquely represented by

a point on or within a unit sphere centred on a rectangular xyz-coordinate system. Fully polarised signals are represented with a point on the sphere; the point coordinates are the normalised stokes parameters, while points close together represent similar polarisation states [163]) is a graphical tool in the real 3-dimensional space to describe polarised signals; any state can be uniquely represented by a point on or within a unit sphere centred on a rectangular xyz-coordinate system. Fully polarised signals are represented with a point on the sphere; the point coordinates are the normalised stokes parameters, while points close together represent similar polarisation states [163]

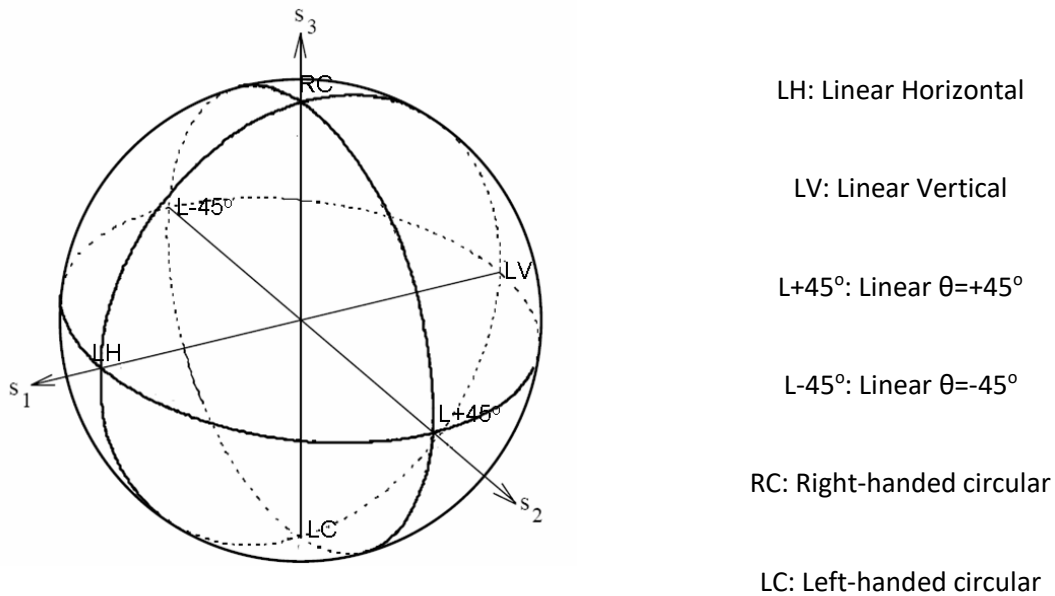


Fig. app. 4. 2. 2: Poincare sphere is a graphical tool to uniquely represent a polarisation state

The distance of the output polarisation state ($S_{1\text{measured}}, S_{2\text{measured}}, S_{3\text{measured}}$) and the desired output polarisation state ($S_{1\text{desired}}, S_{2\text{desired}}, S_{3\text{desired}}$) can be represented by the

distance of the two corresponding points on the Poincare sphere. Thus, the desired polarisation state can be considered to be set when this distance is smaller than the required precision, which in our case has been decided to be 0.009.

$$d = \sqrt{(s_{1measured} - s_{1desired})^2 + (s_{2measured} - s_{2desired})^2 + (s_{3measured} - s_{3desired})^2} < precision \quad \text{Eq. app. 4. 2. 1}$$

The Stokes vector distance d is a function of four parameters, the positions of the four fibre loops of the polarisation controller. The value of the function d can be calculated for any quadruplet (P_1, P_2, P_3, P_4) , where P_i the setting of the i polarisation controller paddle and $0 \leq P_i \leq 999$, by measuring the illuminating light polarisation and then calculate Stokes vector distance d using Eq. app. 4. 2.1. However, the actual formula which connects the P_i values to the polarisation state of the illuminating light is unknown. In order to set the desired polarisation state, the quadruplet which minimises or in other words sets this function value to be less than the required precision should be found; one way to deal with this requirement is to use the Nelder-Mead algorithm [164].

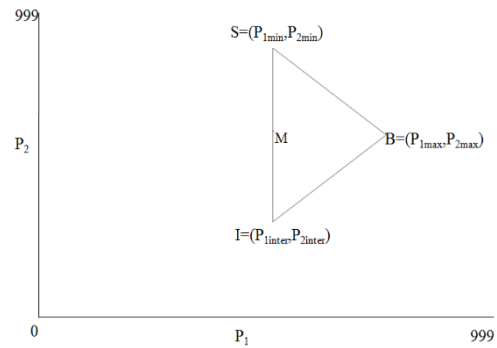
App.4.3 Description of the Nelder-Mead algorithm and its application to the automatic set-up of a specific polarisation state of a laser output beam

The problem of the automatic set-up of the desired polarisation state was solved applying the Nelder-Mead algorithm[164] for the minimization of the 4-variable unknown function d . The problem of the automatic set-up of the desired polarisation state was solved

applying the Nelder-Mead algorithm[164] for the minimization of the 4-variable unknown function d . The problem of the automatic set-up of the desired polarisation state was solved applying the Nelder-Mead algorithm[164] for the minimization of the 4-variable unknown function d . The problem of the automatic set-up of the desired polarisation state was solved applying the Nelder-Mead algorithm[164] for the minimization of the 4-variable unknown function d . The general idea of the method is that in order to minimise a n -variable function, the function values at $(n+1)$ vertices of a general simplex (generalised triangle) are compared and the one with the highest value is replaced with another one. Assuming that the polarisation was controlled by two paddles (P_1 and P_2) and the Stokes vector distance d was a 2-variable function; the $(n+1)$ dimensions general simplex would be actually degraded into a simple triangle located on a 2-D Cartesian system where the axes would extend from 0 to 999, since each point at this system corresponds to a duplet of polarisation controller settings (P_{1i}, P_{2i}) .

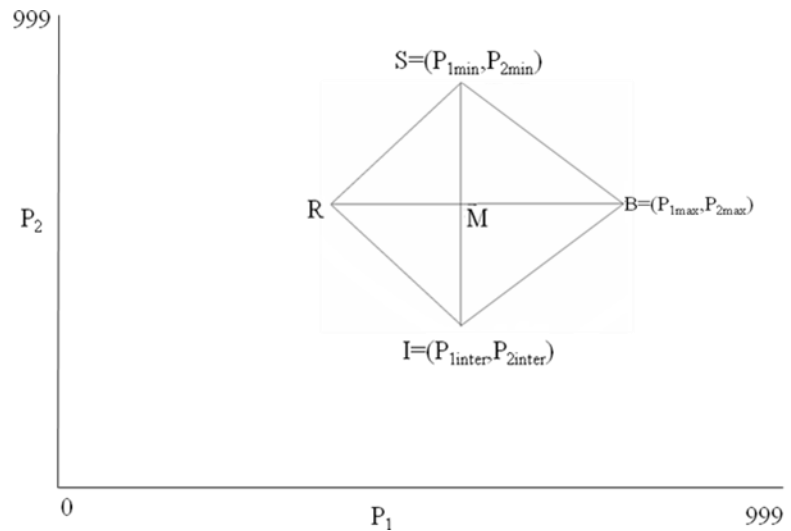
Polarisation would be measured at three points (P_{1i}, P_{2i}) , where $i=1,2,3$ and the Stokes vector distance d_i would be calculated for each of these three points. Let $B=(P_{1max}, P_{2max})$ be the point with the maximum Stokes vector d value, $S=(P_{1min}, P_{2min})$ the point with the minimum d value, and $I=(P_{1inter}, P_{2inter})$ the point at which the value of Stokes vector d is between the maximum and the minimum ones. The first step after the comparison is to calculate the middle point of the good side of the triangle.

$$M = \frac{S + I}{2} = \left(\frac{x_{\min} + x_{inter}}{2}, \frac{y_{\min} + y_{inter}}{2} \right)$$



Since the requirement would be to go far from the max point and closer to the good side, the reflection of the B (P_{1max}, P_{2max}) over the good side would be calculated.

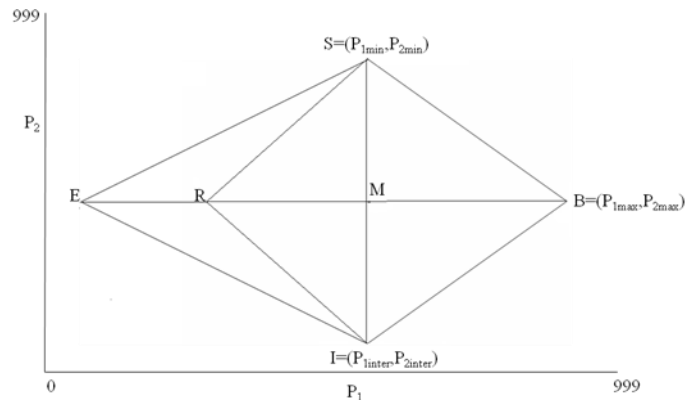
$$R = M - (M - B) \Rightarrow R = 2M - B$$



In order to check if this step fulfilled our requirement, the minimization of the function, or not, the f_R and f_B would be compared. If $f_R < f_B$, the move would appear to be in the correct direction, an additional step would be taken in the same direction by calculating the expansion E.

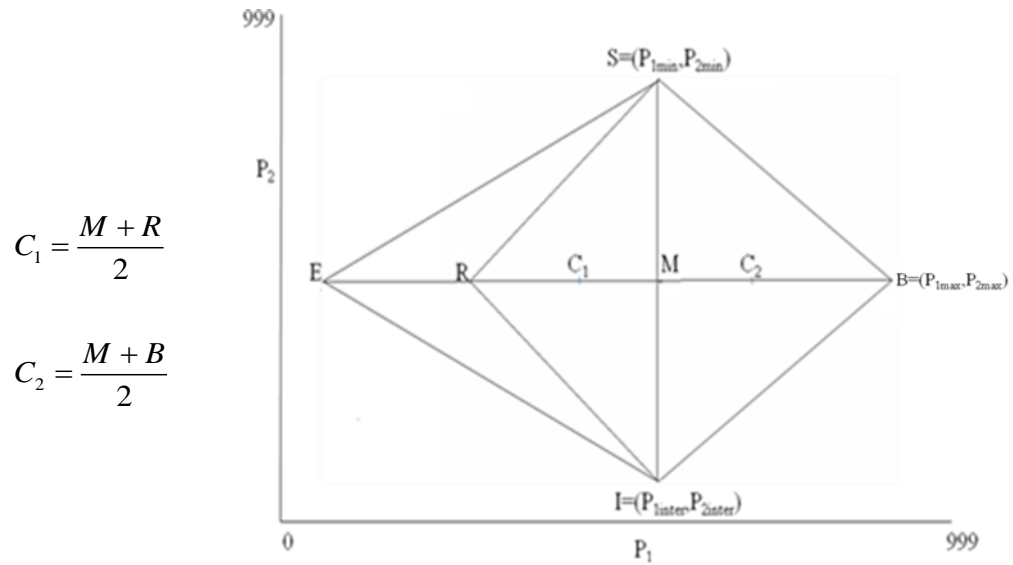
$$E = R + (R - M) \Rightarrow$$

$$\Rightarrow E = 2R - M$$

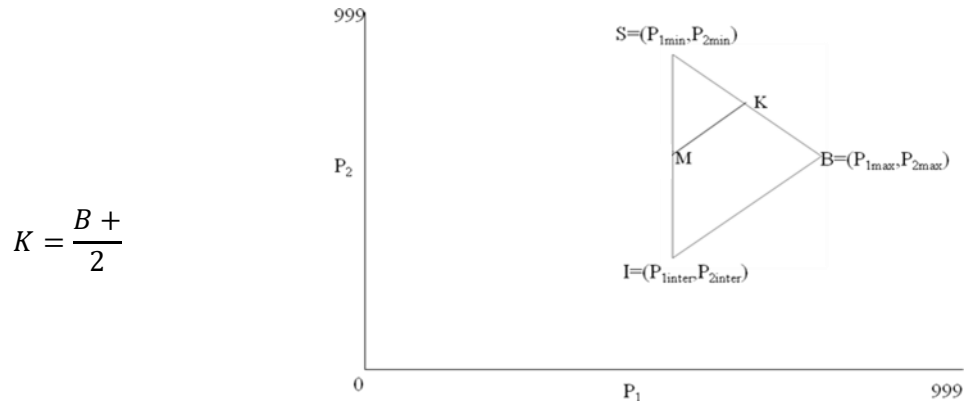


f_R and the f_E would be compared and the point having the smallest function value would be maintained; if $f_E < f_R$, the triangle $B\hat{I}S$ would be replaced with the triangle $E\hat{I}S$ otherwise it would be replaced with the triangle $R\hat{I}S$.

On the other hand if $f_R > f_B$, it would mean that we moved too far from the good side IS of the triangle and a closer to it point would have to be calculated. In order to decide towards which direction to move, one point at each side of the IS line would need to be calculated, C_1 and C_2 ; the function values would be compared and the point which would give the smaller d value would be selected and renamed to C .



In continue f_c would be compared with f_B ; if $f_c < f_B$, the $B\hat{I}S$ triangle would be replaced with the $C\hat{I}S$ triangle, otherwise both the B and the I points have to shrink towards the S point. In order to shrink towards the S point, I point would be replaced by M while B point would be replaced by the BS line middle point K; the triangle $B\hat{S}I$ would be replaced by the triangle $K\hat{S}M$.



This process would continue until the Stokes vector distance d corresponding to the polarisation controller settings (P_{1min}, P_{2min}) become smaller than the required precision

value,0.009; the polarisation controller settings required to set the illuminating light polarisation at the desired polarisation state would have been found.

At this point it is worth mentioning the three practical issues which were crucial for the implementation of the algorithm using the specific polarisation controller; these issues are again analysed for the case of the 2 paddle polarisation controller for simplicity. The settings of the polarisation controller paddles can only be integers, but the operations described above can also produce fractional numbers, therefore the calculated P_i values should be rounded to the closest integer before sent to the polarisation controller. Furthermore, as described above the polarisation controller settings should be at the range between 0 and 999, but the operations described above can also result to negative numbers or numbers larger than 999; in this case the P_i values should be folded into the 0-999 range. After characterising the polarisation controller, it was decided that the best way to fold P_i values into the 0-999 was to add 999, if P_i is negative, or subtract 999, if P_i is larger than 999. However, folding P_i values into the 0-999 range can lead to the case that one or more of the calculated B,I,S points coincide each other. In order to understand this case, let's consider the following example. If

$$B=(P_{1max}, P_{2max})=(-35,10)$$

$$S=(P_{1min},P_{2min})=(964,10)$$

and

$$I=(P_{1inter},P_{2inter})=(10,10)$$

since $P_{1max}<0$, it should be folded into the 0-999 range by adding 999. Then

$$B=(P_{1max}, P_{2max})=(-35+999,10)=(964,10)$$

and

$$B\equiv S.$$

When two or more of the B,I,S points coincided, the $B\hat{S}I$ triangle would be degraded to a line or even to a point. In order to avoid this situation, which may cause the algorithm to fail, a subroutine called “unequalization of the vertices” would be used at the beginning of each Nelder-Mead algorithm loop iteration. The subroutine would check if any of B,I, and S vertices are equal to each other and in case they were one of the equal vertices would add itself the vector (5,5); the subroutine would stop running when all the vertices were unequal. The choice of the vector (5,5) was such that would not dramatically change the output polarisation state, since the physical change inside the polarisation controller would be very small (0.9° for each fibre loop) but mathematically would keep the algorithm running.

Up to this point the application of the Nelder-Mead algorithm to the automatic set-up of a specific illuminating light polarisation state using a two paddle polarisation controller and a polarimeter has been described. Since the polarisation controller used in the experimental arrangement had four paddles the method described above was generalised and applied for the case that the Stokes vector distance d is a 4-variable function, $d=d(P_{1i}, P_{2i}, P_{3i}, P_{4i})$; in this case the $B\hat{S}I$ triangle became a 5-dimension general simplex. The steps of the generalised algorithm was exactly the same as described above with the difference that instead of comparing three points , they were comparing five points located at the 4-dimension system with axes extended from 0 to 999. The “unequalization of the vertices” subroutine compared five vertices instead of three and added the vector (5,5,5,5) to the one of the equals vertices, until all of them become unequal, instead of the vector (5,5).

One last modification was added to the algorithm in order to increase its time efficiency and ensure that a polarisation state would be set within a given time margin. The average time that the algorithm needed to find one polarisation state was 1-2mins. Therefore, there was a clock measuring the time for which one polarisation state was searched using the Nelder-Mead algorithm, if this time exceeded 4 min the search was restarted replacing one of the points in the 4 dimension space with a different point $P = (P_{1i}, P_{2i}, P_{3i}, P_{4i})$ which were randomly produced by the code.

The method was used both for the optimisation of the polarisation state during the characterisation of the SPPC wavelength dispersion properties and the setting up of the different polarisation states during the characterisation of the SPPC polarisation dispersion properties. Since during the polarisation characterisation, the scanned polarisation states were similar, all of them linear with an angle θ increasing from 0° to 180° with a step of 5° , the search of each polarisation state was initialised with one of 4-dimension space points to be the one that the previous one had ended.

Appendix 5: Define the SPPC centre using the SPP wave symmetry

Before calculating the SPP angular distribution, the centre of the structure was identified. The y-coordinate of the SPPC centre was identified using the SPP wave symmetry on the vertical axis; the y-coordinate of the SPPC centre coincides with the middle point between the SPP waves (Fig. app. 5. 1).

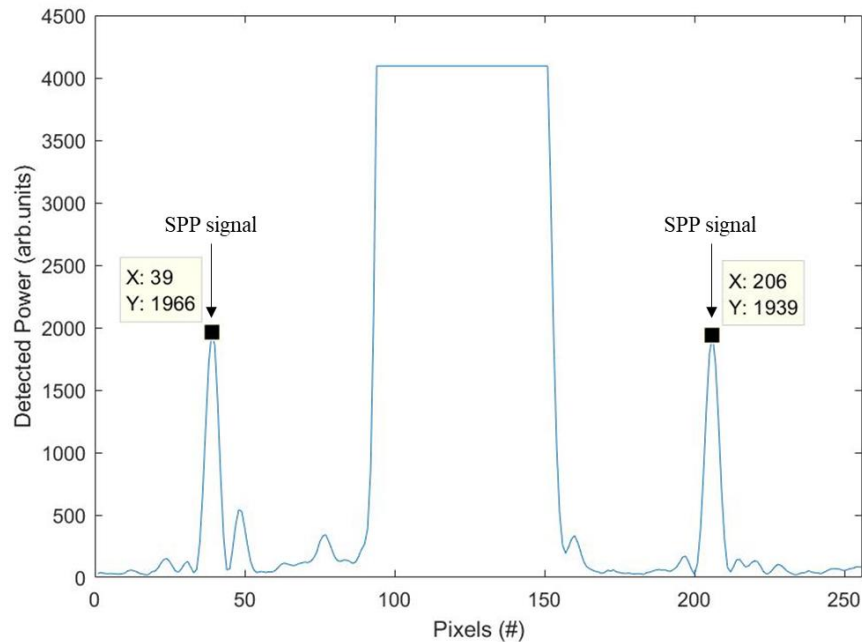


Fig. app. 5. 1: Detected power at pixels lying on the line connecting the two SPP waves on y -axis; the middle point between the SPP signal maxima which coincides with the centre of the SPPC, saturated area, is the middle of the SPPC

Then the intensity distribution over a horizontal line passing through the middle point between the SPP waves was plotted (Fig. app. 5. 2) and the x-coordinate of the SPPC was identified as the middle point of the saturated area.

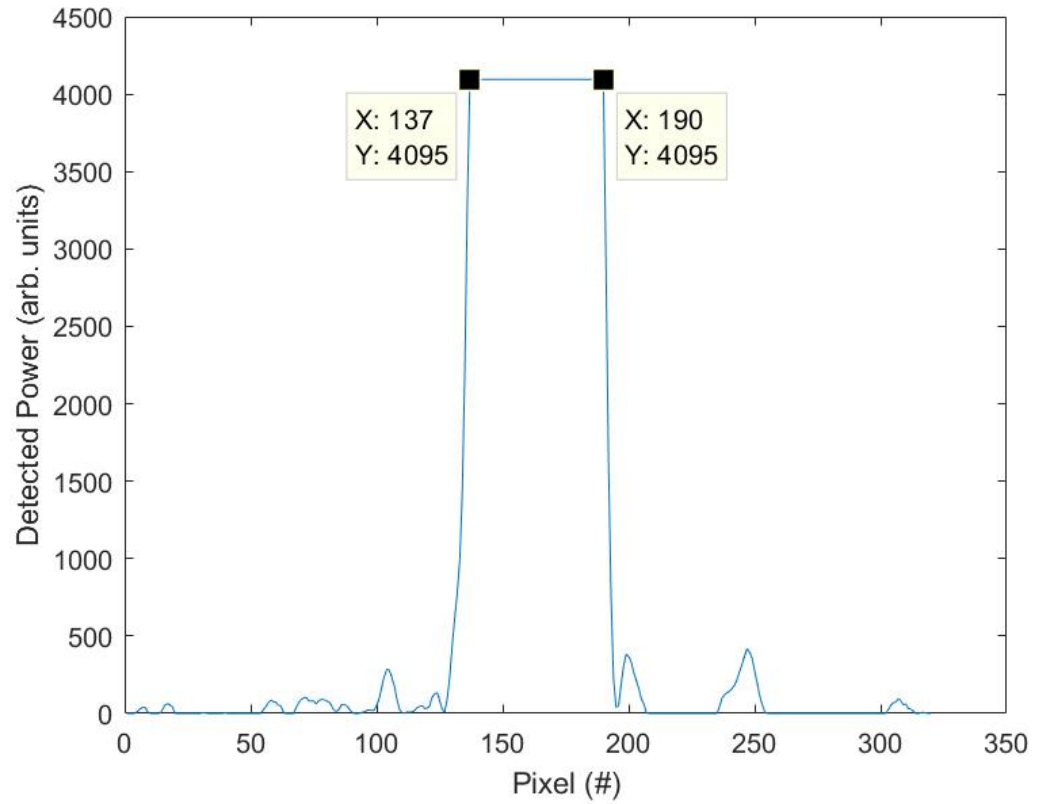


Fig. app. 5. 2: Detected power at pixels lying on a line parallel to the x-axis passing through the y-coordinate of the centre, calculated from Fig. app. 5. 1; the centre of the saturated area determines the x-coordinate of the SPPC centre

Appendix 6: Calculation of the minimum angular resolution using the camera pixel resolution

The smallest achievable angular resolution has been considered to be equal to the arc corresponding to one camera pixel. In order to calculate this arc, the image of the SPPC and the surrounding defect ring (Fig. app. 6. 1 (a)) was used, and the detected power at a line parallel to the y-axis and passing through the SPPC centre has been plotted in Fig. app. 6. 1 (b).

From Fig. app. 6. 1 (b), it can be seen that the diameter of the surrounding ring corresponds to 167 pixels and thus the arc corresponding to 1 pixel, and consequently the smallest angular resolution, is equal to $\text{atan}(2/161)=0.7^\circ$, as show in Fig. app. 6. 1 (a).

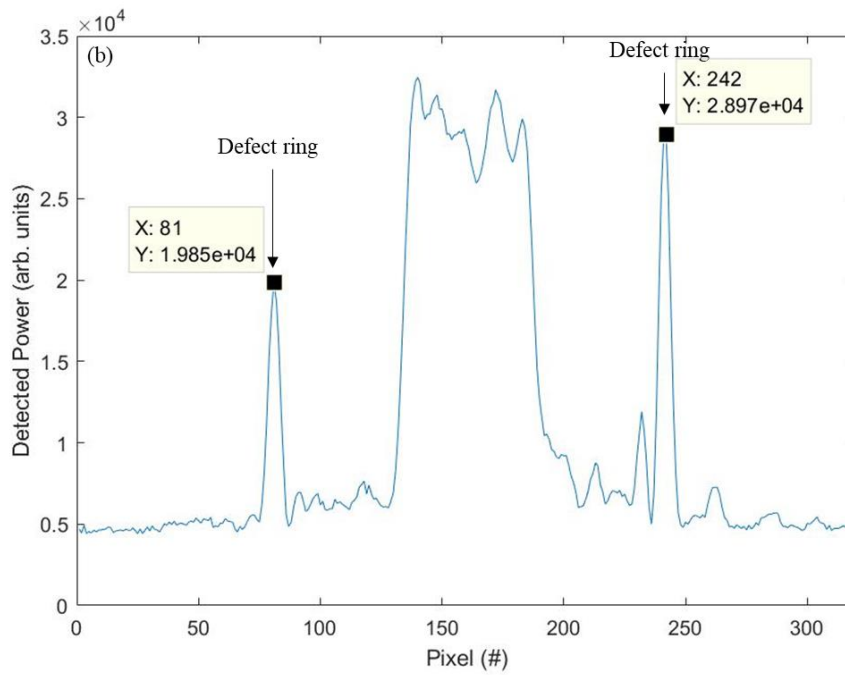
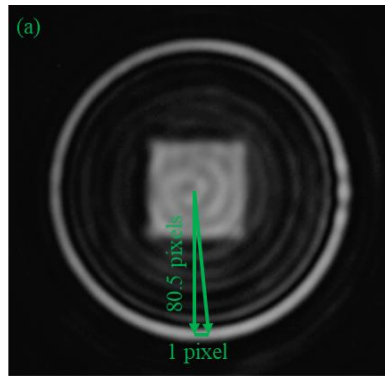


Fig. app. 6. 1: (a) Image of the SPPC and the scattering ring, showing the arc corresponding to 1 pixel (b) Detected power over a line parallel to the y-axis, passing through the SPPC centre

References

- [1] A. V. Zayats, I. I. Smolyaninov, and A. A. Maradudin, "Nano-optics of surface plasmon polaritons," , *Phys Rep*, vol. 408, no. 3-4, pp. 131-314, 2005
- [2] M. I. Benetou, J.-S. Bouillard, P. Segovia, W. Dickson, B. C. Thomsen, P. Bayvel, A. V. Zayats, "Boundary effects in finite size plasmonic crystals: focusing and routing of plasmonic beams for optical communications," *Nanotechnology*, vol. 26, no. 44, p. 444001, 2015
- [3] M. I. Benetou, J.-S. Bouillard, W. Dickson, B. C. Thomsen, P. Bayvel, and A. V. Zayats, "Visualization of high-order plasmonic Bloch modes in square-lattice plasmonic crystal," in *The 5th International Conference on Surface Plasmon Photonics Conference Proceedings (SPP5)*, , Busan, Korea, 2011.
- [4] M. I. Benetou, "SPPC Based Beam Splitter and Alignment Sensor: The Passive and Active Control of its Functionality Parameters," in *Frontiers in Optics + Laser Science APS/DLS*, Optical Society of America, Washington, DC, p. JW3A.68, 2019
- [5] M. I. Benetou, B. C. Thomsen, P. Bayvel, W. Dickson, and A. V. Zayats, "Four-level polarization discriminator based on a surface plasmon polaritonic crystal," *Applied Physics Letters*, vol. 98, no. 11, p. 111109, 2011.
- [6] M. I. Benetou, W. Dickson, B.C. Thomsen, P. Bayvel, and A. V. Zayats, "Microscale polarimeter based on a plasmonic crystal," in *The 5th International Conference on Surface Plasmon Photonics Conference Proceedings (SPP5)*, Busan, p. 135, 2011

- [7] Y.-B. Xie, Z.-Y. Liu, Q.-J. Wang, Y.-Y. Zhu, and X.-J. Zhang, "Miniature polarization analyzer based on surface plasmon polaritons," *Applied Physics Letters*, vol. 105, no. 10, p. 101107, 2014
- [8] F. Afshinmanesh, S. White Justin, W. Cai, and L. Brongersma Mark, "Measurement of the polarization state of light using an integrated plasmonic polarimeter," *Nanophotonics*, vol. 1, pp.125-129, 2012
- [9] A. Pors, M. G. Nielsen, and S. I. Bozhevolnyi, "Plasmonic metagratings for simultaneous determination of Stokes parameters," *Optica*, vol. 2, no. 8, pp. 716-723, 2015
- [10] J. P. Balthasar Mueller, K. Leosson, and F. Capasso, "Ultracompact metasurface in-line polarimeter," *Optica*, vol. 3, no. 1, pp. 42-47, 2016
- [11] E. Maguid, I. Yulevich, D. Veksler, V. Kleiner, M. L. Brongersma, and E. Hasman, "Photonic spin-controlled multifunctional shared-aperture antenna array," *Science*, Vol. 352, Issue 6290, pp. 1202-1206, 2016.
- [12] F. Ding, A. Pors, Y. Chen, V. A. Zenin, and S. I. Bozhevolnyi, "Beam-Size-Invariant Spectropolarimeters Using Gap-Plasmon Metasurfaces," *ACS Photonics*, vol. 4, no. 4, pp. 943-949, 2017
- [13] E. Maguid, I. Yulevich, M. Yannai, V. Kleiner, M. L Brongersma, and E. Hasman, "Multifunctional interleaved geometric-phase dielectric metasurfaces," *Light: Science & Applications*, Original Article vol. 6, p. e17027, 2017
- [14] K. Lee, H. Yun, S. E. Mun, G. Y. Lee, J. Sung, and B. Lee, "Ultracompact Broadband Plasmonic Polarimeter," *Laser & Photonics Reviews*, vol. 12, no. 3, p. 1700297, 2018

- [15] A. Espinosa-Soria, F. J. Rodríguez-Fortuño, A. Griol, and A. Martínez, "Full Measurement of the Stokes Parameters Using a Subwavelength Silicon On-Chip Polarimeter," *Advances in Science and Technology*, vol. 98, pp. 103-108, 2017
- [16] P. Dong, X. Liu, S. Chandrasekhar, L. L. Buhl, R. Aroca, and Y. K. Chen, "Monolithic Silicon Photonic Integrated Circuits for Compact 100+ Gb/s Coherent Optical Receivers and Transmitters," *IEEE Journal of Selected Topics in Quantum Electronics*, vol. 20, no. 4, pp. 150-157, 2014
- [17] S. Beppu, K. Kasai, M. Yoshida, and M. Nakazawa, "2048 QAM (66 Gbit/s) single-carrier coherent optical transmission over 150 km with a potential SE of 15.3 bit/s/Hz," *Optics Express*, vol. 23, no. 4, pp. 4960-4969, 2015
- [18] G. T. Reed, G. Z. Mashanovich, F. Gardes, and D. J. Thomson, "Silicon optical modulators", *Nature Photonics*, **vol 4**, pp. 518–526, 2010
- [19] N. Kinsey, M. Ferrera, V. M. Shalaev, and A. Boltasseva, "Examining nanophotonics for integrated hybrid systems: a review of plasmonic interconnects and modulators using traditional and alternative materials," *Journal of the Optical Society of America B*, vol. 32, no. 1, pp. 121-142, 2015
- [20] C. Haffner *et al.*, "All-plasmonic Mach–Zehnder modulator enabling optical high-speed communication at the microscale," *Nature Photonics*, vol. 9, p. 525, 2015
- [21] W. Cai, J. S. White, and M. L. Brongersma, "Compact, High-Speed and Power-Efficient Electrooptic Plasmonic Modulators," *Nano Letters*, vol. 9, no. 12, pp. 4403-4411, 2009

- [22] S. A. Maier, M. L. Brongersma, P. G. Kik, S. Meltzer, A. A. G. Requicha, and H. A. Atwater, "Plasmonics—A Route to Nanoscale Optical Devices," *Advanced Materials*, vol. 13, no. 19, pp. 1501-1505, 2001
- [23] D. K. Gramotnev and S. I. Bozhevolnyi, "Plasmonics beyond the diffraction limit," *Nature Photonics*, Review Article vol. 4, p. 83, 2010
- [24] J. A. Schuller, E. S. Barnard, W. Cai, Y. C. Jun, J. S. White, and M. L. Brongersma, "Plasmonics for extreme light concentration and manipulation," *Nature Materials*, Review Article vol. 9, p. 193, 2010
- [25] M. L. Brongersma and V. M. Shalaev, "The Case for Plasmonics," *Science*, vol. 328, no. 5977, p. 440, 2010.
- [26] J. A. Dionne, K. Diest, L. A. Sweatlock, and H. A. Atwater, "PlasMOStor: A Metal–Oxide–Si Field Effect Plasmonic Modulator," *Nano Letters*, vol. 9, no. 2, pp. 897-902, 2009
- [27] M. W. Knight, H. Sobhani, P. Nordlander, and N. J. Halas, "Photodetection with Active Optical Antennas," *Science*, vol. 332, no. 6030, p. 702, 2011
- [28] Y. H. Joo, S. H. Song, and R. Magnusson, "Long-range surface plasmon-polariton waveguide sensors with a Bragg grating in the asymmetric double-electrode structure," *Optics Express*, vol. 17, no. 13, pp. 10606-10611, 2009
- [29] J. Rosenberg, R. V. Shenoi, S. Krishna, and O. Painter, "Design of plasmonic photonic crystal resonant cavities for polarization sensitive infrared photodetectors," *Optics Express*, vol. 18, no. 4, pp. 3672-3686, 2010

[30] S. Y. Chou and W. Ding, "Ultrathin, high-efficiency, broad-band, omni-acceptance, organic solar cells enhanced by plasmonic cavity with subwavelength hole array," *Optics Express*, vol. 21, no. S1, pp. A60-A76, 2013

[31] T. Okamoto and K. Shinotsuka, "Improvement of light extraction efficiency and reduction of driving voltage in organic light emitting diodes using a plasmonic crystal," *Applied Physics Letters*, vol. 104, no. 9, p. 093301, 2014

[32] G. Lozano *et al.*, "Plasmonics for solid-state lighting: enhanced excitation and directional emission of highly efficient light sources," *Light: Science & Applications*, Original Article vol. 2, p. e66, 2013

[33] R. F. Oulton *et al.*, "Plasmon lasers at deep subwavelength scale," *Nature*, vol. 461, p. 629, 2009

[34] W. Zhou *et al.*, "Lasing action in strongly coupled plasmonic nanocavity arrays," *Nature Nanotechnology*, vol. 8, p. 506, 2013

[35] F. van Beijnum, P. J. van Veldhoven, E. J. Geluk, M. J. A. de Dood, G. W. 't Hooft, and M. P. van Exter, "Surface Plasmon Lasing Observed in Metal Hole Arrays," *Physical Review Letters*, vol. 110, no. 20, p. 206802, 2013

[36] D. A. B. Miller, "Attojoule Optoelectronics for Low-Energy Information Processing and Communications," *Journal of Lightwave Technology*, vol. 35, no. 3, pp. 346-396, 2017

[37] P. Kok, W. J. Munro, K. Nemoto, T. C. Ralph, J. P. Dowling, and G. J. Milburn, "Linear optical quantum computing with photonic qubits," *Reviews of Modern Physics*, vol. 79, no. 1, pp. 135-174, 2007

- [38] A. Shacham, K. Bergman, and L. P. Carloni, "Photonic Networks-on-Chip for Future Generations of Chip Multiprocessors," *IEEE Transactions on Computers*, vol. 57, no. 9, pp. 1246-1260, 2008.
- [39] J. Paniccia Mario, "A perfect marriage: optics and silicon," *Optik & Photonik*, vol. 6, no. 2, pp. 34-38, 2011
- [40] D. Dai and E. Bowers John, "Silicon-based on-chip multiplexing technologies and devices for Peta-bit optical interconnects," in *Nanophotonics* vol. 3, issue, 4-5, p. 283, 2014
- [41] W. L. Barnes, A. Dereux, and T. W. Ebbesen, "Surface plasmon subwavelength optics," *Nature*, vol. 424, no. 6950, pp. 824-830, 2003
- [42] D. F. P. Pile *et al.*, "Two-dimensionally localized modes of a nanoscale gap plasmon waveguide," *Applied Physics Letters*, vol. 87, no. 26, p. 261114, 2005
- [43] A. V. Zayats and I. I. Smolyaninov, "Near-field photonics: surface plasmon polaritons and localized surface plasmons," *Journal of Optics A: Pure and Applied Optics*, vol. 5, no. 4, pp. S16-S50, 2003
- [44] C. Billaudeau, S. Collin, C. Sauvan, N. Bardou, F. Pardo, and J.-L. Pelouard, "Angle-resolved transmission measurements through anisotropic two-dimensional plasmonic crystals," *Optics Letters*, vol. 33, no. 2, pp. 165-167, 2008
- [45] C. Zhao and J. Zhang, "Plasmonic Demultiplexer and Guiding," *ACS Nano*, vol. 4, no. 11, pp. 6433-6438, 2010
- [46] L. Salomon, F. Grillot, A. V. Zayats, and F. de Fornel, "Near-field distribution of optical transmission of periodic subwavelength holes in a metal film," *Phys Rev Lett*, vol. 86, no. 6, pp. 1110-1113, 2001

- [47] E. Laux, C. Genet, T. Skauli, and T. W. Ebbesen, "Plasmonic photon sorters for spectral and polarimetric imaging," *Nat Photonics*, vol. 2, no. 3, pp. 161-164, 2008
- [48] M. I. Benetou, W. Dickson, V. Mikhailov, B. Thomsen, P. Bayvel, and A. V. Zayats, "Dispersive properties of surface plasmon polaritonic crystals with different boundary shapes," *IEEE Leos Annual Meeting Conference Proceedings*, Belek-Antalya, Turkey, pp. 100-101, 2009
- [49] V. Mikhailov, G. A. Wurtz, J. Elliott, P. Bayvel, and A. V. Zayats, "Dispersing light with surface plasmon polaritonic crystals," *Phys Rev Lett*, vol. 99, no. 8, 2007
- [50] J. Elliott, I. I. Smolyaninov, N. I. Zheludev, and A. V. Zayats, "Wavelength dependent birefringence of surface plasmon polaritonic crystals," *Phys Rev B*, vol. 70, no. 23, 2004
- [51] A. V. Zayats, W. Dickson, I. I. Smolyaninov, and C. C. Davis, "Polarization superprism effect in surface polaritonic crystals," *Applied Physics Letters*, vol. 82, no. 25, pp. 4438-4440, 2003
- [52] M. I. Benetou, W. Dickson, B.C. Thomsen, P. Bayvel, and A. V. Zayats, "Surface plasmon polaritonic crystal polarisation demultiplexer for 4 level polarisation-shift-keying," in *Photon10*, Southampton, UK, 2010.
- [53] H. A. Bethe, "Theory of Diffraction by Small Holes," *Physical Review*, vol. 66, no. 7-8, pp. 163-182, 1944
- [54] T. W. Ebbesen, H. J. Lezec, H. F. Ghaemi, T. Thio, and P. A. Wolff, "Extraordinary optical transmission through sub-wavelength hole arrays," *Nature*, vol. 391, no. 6668, pp. 667-669, 1998

- [55] R. H. Ritchie, E. T. Arakawa, J. J. Cowan, and R. N. Hamm, "Surface-Plasmon Resonance Effect in Grating Diffraction," *Physical Review Letters*, vol. 21, no. 22, pp. 1530-1533
- [56] H. Raether, *Surface plasmons*. Berlin: Springer, 1988
- [57] S. C. Kitson, W. L. Barnes, and J. R. Sambles, "Full Photonic Band Gap for Surface Modes in the Visible," *Physical Review Letters*, vol. 77, no. 13, pp. 2670-2673, 1996
- [58] R. A. Watts, J. B. Harris, A. P. Hibbins, T. W. Preist, and J. R. Sambles, "Optical excitation of surface plasmon polaritons on 90° and 60° bi-gratings," *Journal of Modern Optics*, vol. 43, no. 7, pp. 1351-1360, 1996
- [59] L. Martín-Moreno *et al.*, "Theory of Extraordinary Optical Transmission through Subwavelength Hole Arrays," *Physical Review Letters*, vol. 86, no. 6, pp. 1114-1117, 2001
- [60] P. Lalanne and J. P. Hugonin, "Interaction between optical nano-objects at metallo-dielectric interfaces," *Nature Physics*, vol. 2, no. 8, pp. 551-556, 2006
- [61] T. D. Visser, "Surface plasmons at work?," *Nature Physics*, vol. 2, no. 8, pp. 509-510, 2006
- [62] R. H. Ritchie, "Plasma Losses by Fast Electrons in Thin Films," *Physical Review*, vol. 106, no. 5, pp. 874-881, 1957
- [63] T. J. Kim, T. Thio, T. W. Ebbesen, D. E. Grupp, and H. J. Lezec, "Control of optical transmission through metals perforated with subwavelength hole arrays," *Optics Letters*, vol. 24, no. 4, pp. 256-258, 1999

- [64] C. Genet and T. W. Ebbesen, "Light in tiny holes," *Nature*, Review Article vol. 445, p. 39, 2007
- [65] W. L. Barnes, T. W. Preist, S. C. Kitson, and J. R. Sambles, "Physical origin of photonic energy gaps in the propagation of surface plasmons on gratings," *Phys Rev B*, vol. 54, no. 9, pp. 6227-6244, 1996
- [66] W. L. Barnes, S. C. Kitson, T. W. Preist, and J. R. Sambles, "Photonic surfaces for surface-plasmon polaritons," *Journal of the Optical Society of America A*, vol. 14, no. 7, pp. 1654-1661, 1997
- [67] I. I. Smolyaninov, W. Atia, and C. C. Davis, "Near-field optical microscopy of two-dimensional photonic and plasmonic crystals," *Physical Review B*, vol. 59, no. 3, pp. 2454-2460, 1999
- [68] A. Kristensen *et al.*, "Plasmonic colour generation," *Nature Reviews Materials*, Review Article vol. 2, p. 16088, 2016
- [69] W. Dickson, G. A. Wurtz, P. R. Evans, R. J. Pollard, and A. V. Zayats, "Electronically controlled surface plasmon dispersion and optical transmission through metallic hole arrays using liquid crystal," *Nano Lett*, vol. 8, no. 1, pp. 281-286, 2008
- [70] Y. G. Chen *et al.*, "Hybrid phase-change plasmonic crystals for active tuning of lattice resonances," *Optics Express*, vol. 21, no. 11, pp. 13691-13698, 2013
- [71] C. H. Chu *et al.*, "Laser-induced phase transitions of Ge₂Sb₂Te₅ thin films used in optical and electronic data storage and in thermal lithography," *Optics Express*, vol. 18, no. 17, pp. 18383-18393, 2010

[72] A. G. Brolo, R. Gordon, B. Leathem, and K. L. Kavanagh, "Surface Plasmon Sensor Based on the Enhanced Light Transmission through Arrays of Nanoholes in Gold Films," *Langmuir*, vol. 20, no. 12, pp. 4813-4815, 2004

[73] A. G. Brolo, E. Arctander, R. Gordon, B. Leathem, and K. L. Kavanagh, "Nanohole-Enhanced Raman Scattering," *Nano Letters*, vol. 4, no. 10, pp. 2015-2018, 2004

[74] P. R. H. Stark, A. E. Halleck, and D. N. Larson, "Short order nanohole arrays in metals for highly sensitive probing of local indices of refraction as the basis for a highly multiplexed biosensor technology," *Methods*, vol. 37, no. 1, pp. 37-47, 2005

[75] W. Yue *et al.*, "Enhanced extraordinary optical transmission (EOT) through arrays of bridged nanohole pairs and their sensing applications," *Nanoscale*, vol. 6, no. 14, pp. 7917-7923, 2014

[76] X. Han, K. Liu, and C. Sun, "Plasmonics for Biosensing," *Materials*, vol. 12, no. 9, 2019

[77] C. Lu, Z. Qi, X. Hu, Z. Ni, and Y. Cui, "Selectively enhanced Raman scattering with triple-resonance nanohole arrays," *Optics Communications*, vol. 452, pp. 494-498, 2019

[78] B. Cherif *et al.*, "Clinically Related Protein–Peptide Interactions Monitored in Real Time on Novel Peptide Chips by Surface Plasmon Resonance Imaging," *Clinical Chemistry*, vol. 52, no. 2, p. 255, 2006

[79] J. A. Lofgren *et al.*, "Comparing ELISA and Surface Plasmon Resonance for Assessing Clinical Immunogenicity of Panitumumab," *The Journal of Immunology*, vol. 178, no. 11, p. 7467, 2007

- [80] V. Malyarchuk *et al.*, "High performance plasmonic crystal sensor formed by soft nanoimprint lithography," *Optics Express*, vol. 13, no. 15, pp. 5669-5675, 2005
- [81] J. A. Maynard *et al.*, "Surface plasmon resonance for high-throughput ligand screening of membrane-bound proteins," *Biotechnology Journal*, vol. 4, no. 11, pp. 1542-1558, 2009
- [82] H. Gao *et al.*, "Using the Angle-Dependent Resonances of Molded Plasmonic Crystals To Improve the Sensitivities of Biosensors," *Nano Letters*, vol. 10, no. 7, pp. 2549-2554, 2010
- [83] J.-C. Yang, J. Ji, J. M. Hogle, and D. N. Larson, "Metallic Nanohole Arrays on Fluoropolymer Substrates as Small Label-Free Real-Time Bioprobes," *Nano Letters*, vol. 8, no. 9, pp. 2718-2724, 2008
- [84] N. C. Lindquist, A. Lesuffleur, H. Im, and S.-H. Oh, "Sub-micron resolution surface plasmon resonance imaging enabled by nanohole arrays with surrounding Bragg mirrors for enhanced sensitivity and isolation," *Lab on a Chip*, vol. 9, no. 3, pp. 382-387, 2009
- [85] Maier and S. A., *Plasmonics-fundamentals and applications*. Bath, 2006
- [86] H. W. Gao, W. Zhou, and T. W. Odom, "Plasmonic Crystals: A Platform to Catalog Resonances from Ultraviolet to Near-Infrared Wavelengths in a Plasmonic Library", *Adv Funct Mater*, vol. 20, no. 4, pp. 529-539, 2010
- [87] A. V. Zayats, L. Salomon, and F. de Fornel, "How light gets through periodically nanostructured metal films: a role of surface polaritonic crystals," (in English), *J Microsc-Oxford*, vol. 210, pp. 344-349, 2003

- [88] A. Drezet, D. Koller, A. Hohenau, A. Leitner, F. R. Aussenegg, and J. R. Krenn, "Plasmonic crystal demultiplexer and multiports," *Nano Lett*, vol. 7, no. 6, pp. 1697-1700, 2007
- [89] J.-S. Bouillard, P. Segovia, W. Dickson, G. Wurtz, and A. Zayats, "Shaping plasmon beams via the controlled illumination of finite-size plasmonic crystals," *Scientific reports*, vol. 4, p. 7234, 2014
- [90] J.-S. Bouillard, S. Vilain, W. Dickson, and A. Zayats, "Hyperspectral imaging with scanning near-field optical microscopy: applications in plasmonics," *Optics express*, vol. 18, no. 16, pp. 16513-16519, 2010
- [91] J. S. G. Bouillard, W. Dickson, G. A. Wurtz, and A. V. Zayats, "Near-Field Hyperspectral Optical Imaging," *ChemPhysChem*, vol. 15, no. 4, pp. 619-629, 2014
- [92] S. I. Bozhevolnyi and V. Coello, "Elastic scattering of surface plasmon polaritons: Modeling and experiment," *Physical Review B*, vol. 58, no. 16, pp. 10899-10910, 1998
- [93] T. Sondergaard and S. I. Bozhevolnyi, "Vectorial model for multiple scattering by surface nanoparticles via surface polariton-to-polariton interactions," *Phys Rev B*, vol. 67, no. 16, 2003
- [94] P. Segovia and V. Coello, "Elastic surface plasmon polariton scattering: near- and far-field interactions," *Nano*, vol. 7, no. 01, p. 1150003, 2012
- [95] A. B. Evlyukhin and S. I. Bozhevolnyi, "Point-dipole approximation for surface plasmon polariton scattering: Implications and limitations," *Physical Review B*, vol. 71, no. 13, p. 134304, 2005

- [96] P. Gay-Balmaz and O. J. F. Martin, "Validity domain and limitation of non-retarded Green's tensor for electromagnetic scattering at surfaces," *Optics Communications*, vol. 184, no. 1, pp. 37-47, 2000
- [97] S. B. Cho, C. Liu, M. Gustafsson, and D. Y. Kim, "Vector wave analysis for nonnormal incident rays in epimicroscopic refractive index profile measurements," *Applied Optics*, vol. 47, no. 2, pp. 157-163, 2008
- [98] E. Wolf, "Electromagnetic diffraction in optical systems - I. An integral representation of the image field," *Proceedings of the Royal Society of London. Series A. Mathematical and Physical Sciences*, vol. 253, no. 1274, p. 349, 1959
- [99] B. Richards and E. Wolf, "Electromagnetic diffraction in optical systems, II. Structure of the image field in an aplanatic system," *Proceedings of the Royal Society of London. Series A. Mathematical and Physical Sciences*, vol. 253, no. 1274, p. 358, 1959
- [100] S.-Y. Hasegawa, N. Aoyama, A. Futamata, and T. Uchiyama, "Optical tunneling effect calculation of a solid immersion lens for use in optical disk memory," *Applied Optics*, vol. 38, no. 11, pp. 2297-2300, 1999
- [101] E. D. Palik, *Handbook of Optical Constants of Solids*. 1985
- [102] J.-S. G. Bouillard, W. Dickson, D. P. O'Connor, G. A. Wurtz, and A. V. Zayats, "Low-temperature plasmonics of metallic nanostructures," *Nano letters*, vol. 12, no. 3, pp. 1561-1565, 2012.
- [103] J.-S. Bouillard, S. Vilain, W. Dickson, G. Wurtz, and A. Zayats, "Broadband and broadangle SPP antennas based on plasmonic crystals with linear chirp," *Scientific reports*, vol. 2, 2012

- [104] A. Evlyukhin *et al.*, "Focusing and directing of surface plasmon polaritons by curved chains of nanoparticles," *Opt. Express*, vol. 15, no. 25, pp. 16667-16680, 2007
- [105] C. E. Garcia-Ortiz, V. Coello, Z. Han, and S. I. Bozhevolnyi, "Generation of diffraction-free plasmonic beams with one-dimensional Bessel profiles," *Optics letters*, vol. 38, no. 6, pp. 905-907, 2013
- [106] L. Li, T. Li, S. Wang, C. Zhang, and S. Zhu, "Plasmonic Airy beam generated by in-plane diffraction," *Physical review letters*, vol. 107, no. 12, p. 126804, 2011
- [107] L. Li, T. Li, S. Wang, and S. Zhu, "Collimated plasmon beam: nondiffracting versus linearly focused," *Physical review letters*, vol. 110, no. 4, p. 046807, 2013
- [108] J. Lin, J. Dellinger, P. Genevet, B. Cluzel, F. De Fornel, and F. Capasso, "Cosine-Gauss plasmon beam: a localized long-range nondiffracting surface wave," *Physical review letters*, vol. 109, no. 9, p. 093904, 2012
- [109] Z. Liu, J. M. Steele, W. Srituravanich, Y. Pikus, C. Sun, and X. Zhang, "Focusing surface plasmons with a plasmonic lens," *Nano letters*, vol. 5, no. 9, pp. 1726-1729, 2005
- [110] A. Minovich, A. E. Klein, N. Janunts, T. Pertsch, D. N. Neshev, and Y. S. Kivshar, "Generation and near-field imaging of Airy surface plasmons," *Physical review letters*, vol. 107, no. 11, p. 116802, 2011
- [111] B. Stein, J.-Y. Laluet, E. Devaux, C. Genet, and T. W. Ebbesen, "Surface plasmon mode steering and negative refraction," *Physical review letters*, vol. 105, no. 26, p. 266804, 2010
- [112] E. Altewischer, X. Ma, M. P. van Exter, and J. P. Woerdman, "Resonant Bragg scatter of surface plasmons on nanohole arrays," *New J Phys*, vol. 8, 2006

- [113] K. Lin and W. Lee, "Guided-wave 1.3/1.55 μm wavelength division multiplexer based on multimode interference," *Electronics Letters*, vol. 32, no. 14, pp. 1259-1261, 1996
- [114] L. Baojun, L. Guozheng, L. Enke, J. Zuimin, Q. Jie, and W. Xun, "Low-loss 1×2 multimode interference wavelength demultiplexer in silicon-germanium alloy," *IEEE Photonics Technology Letters*, vol. 11, no. 5, pp. 575-577, 1999
- [115] S.-L. Tsao, H.-C. Guo, and C.-W. Tsai, "A novel 1×2 single-mode 1300/1550 nm wavelength division multiplexer with output facet-tilted MMI waveguide," *Optics Communications*, vol. 232, no. 1, pp. 371-379, 2004
- [116] J. Xiao, X. Liu, and X. Sun, "Design of an ultracompact MMI wavelength demultiplexer in slot waveguide structures," *Optics Express*, vol. 15, no. 13, pp. 8300-8308, 2007
- [117] D. Malka, Y. Sintov, and Z. Zalevsky, "Design of a 1×4 silicon-alumina wavelength demultiplexer based on multimode interference in slot waveguide structures," *Journal of Optics*, vol. 17, no. 12, p. 125702, 2015
- [118] B. B. Ben Zaken, T. Zanzury, and D. Malka, "An 8-Channel Wavelength MMI Demultiplexer in Slot Waveguide Structures," *Materials*, vol. 9, no. 11, 2016
- [119] V. R. Almeida, C. A. Barrios, R. R. Panepucci, and M. Lipson, "All-optical control of light on a silicon chip," *Nature*, vol. 431, p. 1081, 2004
- [120] M. S. Dahlem, C. W. Holzwarth, A. Khilo, F. X. Kärtner, H. I. Smith, and E. P. Ippen, "Reconfigurable multi-channel second-order silicon microring-resonator filterbanks for on-chip WDM systems," *Optics Express*, vol. 19, no. 1, pp. 306-316, 2011

- [121] H. Alipour-Banaei, S. Serajmohammadi, and F. Mehdizadeh, "Optical wavelength demultiplexer based on photonic crystal ring resonators," *Photonic Network Communications*, vol. 29, no. 2, pp. 146-150, 2015
- [122] C.-T. Wu, C.-C. Huang, and Y.-C. Lee, "Plasmonic wavelength demultiplexer with a ring resonator using high-order resonant modes," *Applied Optics*, vol. 56, no. 14, pp. 4039-4044, 2017
- [123] C. Lu, Y.-C. Liu, X. Hu, H. Yang, and Q. Gong, "Integrated ultracompact and broadband wavelength demultiplexer based on multi-component nano-cavities," *Scientific Reports*, Article vol. 6, p. 27428, 2016
- [124] A. Tervonen, P. Poyhonen, S. Honkanen, and M. Tahkokorpi, "A guided-wave Mach-Zehnder interferometer structure for wavelength multiplexing," *IEEE Photonics Technology Letters*, vol. 3, no. 6, pp. 516-518, 1991
- [125] N. Goto and G. L. Yip, "Y-branch wavelength multi/demultiplexer for gamma = 1.30 and 1.55 μm ," *Electronics Letters*, vol. 26, no. 2, pp. 102-103, 1990
- [126] R. Dadabayev, N. Shabairou, Z. Zalevsky, and D. Malka, "A visible light RGB wavelength demultiplexer based on silicon-nitride multicore PCF," *Optics & Laser Technology*, vol. 111, pp. 411-416, 2019
- [127] O. Bryngdahl, "Image formation using self-imaging techniques," *Journal of the Optical Society of America*, vol. 63, no. 4, pp. 416-419, 1973
- [128] R. Ulrich, "Light-propagation and imaging in planar optical waveguides," *Nouvelle Revue d'Optique*, vol. 6, no. 5, pp. 253-262, 1975

[129] M. Bachmann, P. A. Besse, and H. Melchior, "General self-imaging properties in $N \times N$ multimode interference couplers including phase relations," *Applied Optics*, vol. 33, no. 18, pp. 3905-3911, 1994

[130] L. B. Soldano and E. C. M. Pennings, "Optical multi-mode interference devices based on self-imaging: principles and applications," *Journal of Lightwave Technology*, vol. 13, no. 4, pp. 615-627, 1995

[131] T. Fujisawa and M. Koshiya, "Theoretical investigation of ultrasmall polarization-insensitive $1/\sqrt{2}$ multimode interference waveguides based on sandwiched structures," *IEEE Photonics Technology Letters*, vol. 18, no. 11, pp. 1246-1248, 2006

[132] V. R. Almeida, Q. Xu, C. A. Barrios, and M. Lipson, "Guiding and confining light in void nanostructure," *Optics Letters*, vol. 29, no. 11, pp. 1209-1211, 2004

[133] S. Zhu, T. Y. Liow, G. Q. Lo, and D. L. Kwong, "Silicon-based horizontal nanoplasmonic slot waveguides for on-chip integration," *Optics Express*, vol. 19, no. 9, pp. 8888-8902, 2011

[134] J. Lu and J. Vučković, "Nanophotonic computational design," *Optics Express*, vol. 21, no. 11, pp. 13351-13367, 2013

[135] A. Y. Piggott, J. Lu, T. M. Babinec, K. G. Lagoudakis, J. Petykiewicz, and J. Vučković, "Inverse design and implementation of a wavelength demultiplexing grating coupler," *Scientific Reports*, Article vol. 4, p. 7210, 2014

[136] A. Y. Piggott, J. Lu, K. G. Lagoudakis, J. Petykiewicz, T. M. Babinec, and J. Vučković, "Inverse design and demonstration of a compact and broadband on-chip wavelength demultiplexer," *Nature Photonics*, vol. 9, p. 374, 2015

- [137] A. Y. Piggott, J. Petykiewicz, L. Su, and J. Vučković, "Fabrication-constrained nanophotonic inverse design," *Scientific Reports*, vol. 7, no. 1, p. 1786, 2017
- [138] L. Su, A. Y. Piggott, N. V. Sampa, J. Petykiewicz, and J. Vučković, "Inverse Design and Demonstration of a Compact on-Chip Narrowband Three-Channel Wavelength Demultiplexer," *ACS Photonics*, vol. 5, no. 2, pp. 301-305, 2018
- [139] S. Molesky, Z. Lin, A. Y. Piggott, W. Jin, J. Vucković, and A. W. Rodriguez, "Inverse design in nanophotonics," *Nature Photonics*, vol. 12, no. 11, pp. 659-670 2018
- [140] D. A. B. Miller, "All linear optical devices are mode converters," *Optics Express*, vol. 20, no. 21, pp. 23985-23993, 2012
- [141] R. L. Freeman, *Telecommunication system engineering*, 2nd ed. ed. New York: Wiley, 1989
- [142] A. H. Gnauck *et al.*, "25.6-Tb/s WDM transmission of polarization-multiplexed RZ-DQPSK signals," *J Lightwave Technol*, vol. 26, no. 1-4, pp. 79-84, 2008
- [143] N. Chi, L. Xu, S. Yu, and P. Jeppesen, "Generation and transmission performance of 40Gbit/s polarisation shift keying signal," , *Electron Lett*, vol. 41, no. 9, pp. 547-549, 2005
- [144] M. Nazarathy and E. Simony, "Stokes space optimal detection of multidifferential phase and polarization shift keying modulation," , *J Lightwave Technol*, vol. 24, no. 5, pp. 1978-1988, 2006
- [145] J. S. Tyo, D. L. Goldstein, D. B. Chenault, and J. A. Shaw, "Review of passive imaging polarimetry for remote sensing applications," *Applied Optics*, vol. 45, no. 22, pp. 5453-5469, 2006

- [146] A. Ling, K. P. Soh, A. Lamas-Linares, and C. Kurtsiefer, "An optimal photon counting polarimeter," *Journal of Modern Optics*, vol. 53, no. 10, pp. 1523-1528, 2006
- [147] H. J. Kimble, "The quantum internet," *Nature*, vol. 453, p. 1023, 2008
- [148] H. Hübel *et al.*, "High-fidelity transmission of polarization encoded qubits from an entangled source over 100 km of fiber," *Optics Express*, vol. 15, no. 12, pp. 7853-7862, 2007
- [149] W. A. Hiltner, "Polarization of Light From Distant Stars by Interstellar Medium," *Science*, vol. 109, no. 2825, p. 165, 1949
- [150] P. A. R. Ade *et al.*, "Antenna-coupled TES Bolometers Used in BICEP2, Keck Array, and Spider," *The Astrophysical Journal*, vol. 812, no. 2, p. 176, 2015
- [151] J. P. B. Mueller, K. Leosson, and F. Capasso, "Polarization-Selective Coupling to Long-Range Surface Plasmon Polariton Waveguides," *Nano Letters*, vol. 14, no. 10, pp. 5524-5527, 2014
- [152] J. Lin *et al.*, "Polarization-Controlled Tunable Directional Coupling of Surface Plasmon Polaritons," *Science*, vol. 340, no. 6130, p. 331, 2013
- [153] J. Petersen, J. Volz, and A. Rauschenbeutel, "Chiral nanophotonic waveguide interface based on spin-orbit interaction of light," *Science*, Vol. 346, Issue 6205, pp. 67-71, 2014
- [154] S.-Y. Lee *et al.*, "Role of Magnetic Induction Currents in Nanoslit Excitation of Surface Plasmon Polaritons," *Physical Review Letters*, vol. 108, no. 21, p. 213907, 2012
- [155] F. J. Rodríguez-Fortuño *et al.*, "Near-Field Interference for the Unidirectional Excitation of Electromagnetic Guided Modes," *Science*, vol. 340, no. 6130, p. 328, 2013

- [156] L. Huang *et al.*, "Helicity dependent directional surface plasmon polariton excitation using a metasurface with interfacial phase discontinuity," *Light: Science & Applications*, Original Article vol. 2, p. e70, 2013
- [157] M. Totzeck, W. Ulrich, A. Göhnermeier, and W. Kaiser, "Pushing deep ultraviolet lithography to its limits," *Nature Photonics*, vol. 1, p. 629, 2007
- [158] M. R. Shcherbakov *et al.*, "Plasmonic enhancement of linear birefringence and linear dichroism in anisotropic optical metamaterials," *JETP Letters*, vol. 90, no. 6, p. 433, 2009
- [159] M. Anastasiadou *et al.*, "Polarimetric imaging for the diagnosis of cervical cancer," *physica status solidi c*, vol. 5, no. 5, pp. 1423-1426, 2008
- [160] R. M. A. Azzam, I. M. Elminyaw, and A. M. El-Saba, "General analysis and optimization of the four-detector photopolarimeter," *Journal of the Optical Society of America A*, vol. 5, no. 5, pp. 681-689, 1988
- [161] A. Pors and S. I. Bozhevolnyi, "Waveguide Metacouplers for In-Plane Polarimetry," *Physical Review Applied*, vol. 5, no. 6, p. 064015, 2016
- [162] W. T. Chen, P. Török, M. R. Foreman, C. Y. Liao, W.-Y. Tsai, P. R. Wu, and D. P. Tsai, "Integrated plasmonic metasurfaces for spectropolarimetry," *Nanotechnology*, vol. 27, no. 22, p. 224002, 2016.
- [163] *Fibre Optic Test and Measurement* (Hewlett-Packard Professional Books)
- [164] J. A. Nelder and R. Mead, "A Simplex Method for Function Minimization," *The Computer Journal*, vol. 7, no. 4, pp. 308-313, 1965